Materials design and theory of nanoscale thermoelectric junctions

Majed Alshammari

PhD Thesis in nanoscience

Department of physics, Lancaster University, UK

This Thesis is submitted in partial fulfilment of the requirements for degree of Doctor of Philosophy

2021

Declaration

I hereby declare that the thesis is my own work and effort and has not been submitted in substantially the same form for the award of a higher degree elsewhere. Other sources of information have been used, they have been acknowledged. This thesis documents work carried out between October 2018 and November 2021 at Lancaster University, UK, under the supervision of Prof. Colin J. Lambert and funded by Ministry of Education Saudi Arabia and Aljouf University, KSA.

Majed Alshammari

November 2021

Acknowledgment

I would like to express deepest gratitude to Prof. Colin John Lambert for the excellent supervision and guidance I received. This thesis would never have been completed without his supervision and assistance. I would also like to express my grateful admiration to Dr Ali Ismael, none of this work would have been accomplished without his insightful comments and suggestions, dedicated time, and guidance. Also, many thanks to Theory of molecular-Scale groups especially Dr Iain Grace.

I would like also to thank my sponsor, the Ministry of Education-KSA and my University in Saudi Arabia Aljouf University, for given me this great opportunity to study a Ph.D. in the United Kingdom.

I would like to thank the collaborating experimental groups. I would like to thank all my friends and colleagues in Colin's group.

Last but not the least, I would like to thank my family: my father, mother, my brothers and sisters and not forget to thank my wife, son Ameer and my daughter Malak.

Above all, my great thanks to ALLAH for his mercy and blessing.

Majed

List of Publications

1- Ismael, A., Al-Jobory, A., Wang, X., Alshehab, A., Almutlg, A., **Alshammari, M.,** and Lambert, C. (2020). Molecular-scale thermoelectricity: as simple as 'ABC'. *Nanoscale Advances*, *2*(11), 5329-5334.

2- Wang, X., Ismael, A., Almutlg, A., **Alshammari, M.,** Al-Jobory, A., Alshehab, A., and Lambert, C. (2021). Optimised power harvesting by controlling the pressure applied to molecular junctions. *Chemical Science*.

3- Bennett,T. **Alshammari, M.,** Almutlg, A., Wang,X. Ismael, A., Luke A., Wilkinson, Andrew J. P. White[a], Albrecht,T. Jarvis,S., Lesley F., Cohen,. Lambert, C., Robinson, B., and Long, N. Multi-Component Self-Assembly on a Surface - Towards New Thermoelectric Systems. (submitted).

Content

Chapter 1

1.1 Molecular electronics and Thermopower

Molecular electronics studies molecular building blocks to design electronic components or electronic devices [1]. These electronic ingredients, such as self-assembled monolayer (SAM) [2] and single-molecule [3] junction, have the potential to deliver: logic gates [4], sensors [5-6], memories [7], and thermoelectric energy with ultralow power requirements and sub 10 nm device footprint. These are also interested in their ability to probe room-temperature quantum properties at a molecular scale, including quantum interference [8] and thermoelectricity [9, 10]. In 1974, the first molecular rectifier was proposed by Aviram and Ratner [11]. These Single molecular electronics has attracted great attention from various researchers. A vast number of molecules are investigated by modifying their chemical structure, some of which act as fundamental electronic elementary devices, including rectifiers, [12] conducting wires, [13-14] and negative differential resistance devices, [15]. Molecular electronics faces a critical challenge, such as utilizing specific intermolecular interactions to assemble molecular devices appropriately. As a result, having a comprehensive explanation of electron transport between adjacent molecules is necessary.

A simple electrode/molecule/electrode system, is studied mainly by theoretical and experimental techniques, which will be discussed in this thesis. These systems can be measured experimentally utilizing two types of equipment such as Scanning Tunneling Microscopy Break Junctions (STM-BJ) [16] and Mechanically Controllable Break Junctions MCBJ [17]. Such methods have been used and developed for contacting single molecules, graphene-based junctions [18], and silicene-based junctions [19]. On the other hand, structural defects in 2D

hexagonal materials, as expected several years earlier [20], indicate that their use as electrodes is still in its infancy. For the moment, gold break junctions remain the contacting method of choice. Because of these constraints, various ways of controlling electron transport have been developed, such as mechanical gating [21] and electrochemical gating [22].

Single-molecule electronic devices face many challenges, which summarises as follows:

1- The length of molecules use in the studied field is in order of 1-2 nm. Furthermore, electrodes separated by 1-2 nm, which are typically made from noble metals, are beyond the capabilities of classical top-down lithographic techniques.

2- The tiny dimensions of the molecule are considered, where direct manipulation of the molecule in the nanogap is typically impractical. To place the molecule in a gap between electrodes, the chemical interaction between the molecule and the electrode is essential.

3- The electrodes' sizes are much larger than molecules; thus, it is challenging to place a single molecule in each functional device.

Additionally, there are not only these three issues, but also there are other significant challenges including: device stability, uniformity, yield, and scalability.

Furthermore, there has been a lot of improvement in understanding the thermoelectrical properties of single-molecule junctions [23], stimulated in part by observations of high Seebeck coefficient S of order 161 μVK^{-1} for PEDOT: PSS organic films [24]. Recently, it was found that the sign of the S in fullerenes and nanotubes can be changed through pressure, strain, and intermolecular interactions [25]. Significantly, many of the quantum interaction effects found and predicted in single-molecule junctions are now being scaled up to self-assembled monolayers SAM [26-27], resulting in the development of novel thin-film materials with room-

temperature quantum effects controlling transport properties. Therefore, these developments indicate that the world of single-molecule electronics has a bright future in developing novel functional materials.

Recent studies of the Seebeck coefficient S on anthracene molecules have been demonstrated in the following references [58-59]. The Seebeck coefficient S for anthracene molecule (2SMe anchor groups) with two connectivities **9, 10** and **1, 5** were found to be negative -20 and -33.0 $\frac{\mu V}{K}$, respectively. This group also calculated the S for the same molecule, but with different linker (2SAc anchor groups), of the same connectivities and found a positive S +12.5 and +16.3 $\frac{\mu V}{K}$ respectively [26-27].

SAM is an important section of molecular-scale electronics. Presently, there are mainly three global designs for forming ensemble molecular junction for large-area electrical measurements: First: direct formation of metal leads utilizing either electron beam/thermal evaporation or electrochemical deposition, secondly: incorporation of electrically conducting polymers/nanomaterials as an electrode and thirdly: employment of liquid metals as electrodes. To fabricate ensemble molecular junctions using different state-of-art methods, there are many methods such as liquid metal contact, lift-and-float, nanopore and nanowell, on-wire lithography, nanoimprint lithography, crossbar or crosswire, self-aligned lithography, buffer interlayer-based junctions, and on-edge molecular junctions.

In this part, we aim to demonstrate a simple rule for defining the value of electrical conductance that appears from constructive quantum interference in molecules. In general, when a single molecule attaches to metallic leads, electrons entering through the molecule from one electrode to the other can stay phase-coherent, even at room temperature [28-29]. As a result, there has been a lot of discussion about quantum interference (QI). This QI can determine the electrical

conductance of single molecules [30-31]. Thus, both experiment and theory have concentrated on explaining the conditions for the appearance of QI for two cases constructive or destructive interference. The constructive quantum interference (CQI) occurs when it coincides with the molecule's delocalized energy level. In contrast, destructive quantum interference (DQI) occurs when it coincides with a bound state's energy located on a pendant moiety [32, 33]. Since it is typically situated in the HOMO and LUMO (H-L) gap, molecules inside a junction seldom show these QI conditions unless the energy levels are controlled by electrostatic, electrochemical, or mechanical gating. Consequently, the studies have considered the two conditions CQI and DQI when they are defined or located at the H-L gap centre [31,34-37].

Therefore, I demonstrate a Magic ratio rule (MRR) based on the table of quantum numbers. This MRR study contributes connectivity to the studied molecule's electrical conductance, such as the examples below. When one electrode is attached to a site i and the other to a site i′ of the same molecule, the molecule is assigned the "magic integer" Mii'.

Magic integers (MIs) can capture the complexity of interference patterns created by electrons at the center of the HOMO-LUMO gap. Thus, the conductance ratio can be predicted by magic ratio rules (MRR). MRR states that "*the ratio of conductances of two molecules is equal to the squares of the ratios of their magic integers.*" When studying the aromatic core's conductances but different contacts, the MI's signs are irrelevant.

The MRR can be considered an exact formula for conductance ratios of tight-binding representations of molecules; this happened in the weak coupling limit when Fermi energy is located between the H-L gap. In this case, there is no dependence on the size of the H-L gap and is independent of asymmetries in the contact between the leads and the molecule. The MRR can apply for a tight-binding, bipartite lattice of identical sites with identical couplings; when the E_F is defining at the centre of the H-L gap, the number of odd sites equals the number

of even sites. In this case we are describing a simple system of tight-binding Hamiltonian that possess -1 for nearest neighbour couplings and zeroes for on-site energies.

Generally, the mid-gap principle explains how the transmission coefficient at the gap centre is determined if the electrons with energy traveling through the core molecule are equated to the middle of the HOMO-LUMO gap. This depends on the connectivity that is connected to the external electrodes. This shows that it is essential and useful to consider the connectivity to begin with to fabricate single-molecule junctions with good electrical properties. In the case of binding molecules to the electrodes, high conductivity is preferable.

However, to prevent leakage currents when attaching to an electrostatic gate, a low conductance is required. This study provides connectivities with high and low MIs to be obtained utilizing the same molecule.

The examination of the entire Magic number for a molecule core allows us to understand the effect of connectivity on electrical conductance. Consequently, this electrical conductance is proportional to, where is the i, the entry in the magic number table. The following is the simplest example for applying the magic ratio theory based on this paper *Magic Ratios for Connectivities-Driven Electrical Conductance of Graphene-like Molecule by YAN Geng and others (9 authors) etc* [38].

Example 1: we aim to apply the magic ratio theory on a bipartite lattice (benzene ring) consisting of six atoms [38]. To apply this theory, two connectivities are required in the same molecule. Thus, (**1, 4**) and (**1, 2**) are chosen in this example, as shown in the **Figure 1.1**.

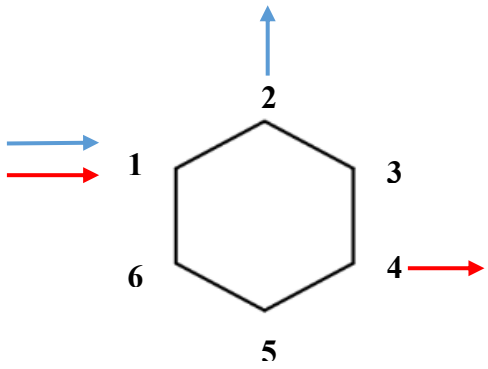

Figure 1.1: Simple example of bipartite lattice such as benzene with the magnitude of its magic number. **(1, 2):** first connectivity; **(1, 4)** the second connectivity.

Table 1.1: magic numbers for Benzene ring.

C=

	1	3	5	2	4	6
1	0	0	0	1	0	1
3	0	0	0	1	1	0
5	0	0	0	0	1	1
2	1	1	0	0	0	0
4	0	1	1	0	0	0
6	1	0	1	0	0	0

Table 1.2: connectivity table

M=

	1	3	5	2	4	6
1	0	0	0	1	-1	1
3	0	0	0	1	1	-1
5	0	0	0	-1	1	1
2	1	1	-1	0	0	0
4	-1	1	1	0	0	0
6	1	-1	1	0	0	0

To determine the ratio of these two connectivities shown in table 1.2, electrical conductance considered to be proportional to $(M_{i\,j})^2$, where i and j the entry and the out. In our case, i and j are (1, 2) for first connectivity and (1, 3) for the second connectivity choice. Therefore, the magic ratio rule (MMR) can be determined for the two connectivities (1, 2) and (1, 4) by:

MRR= $\frac{G_{1,2}}{G_{1,3}} = \frac{(1)^2}{(-1)^2} = \mathbf{1}$.

Example 2 aims to compare the theory and experiment with the magic ratio theory as reported in this paper [38]. Anthanthrene core has been chosen to study. Two connectivities are studied in the same molecule. Thus, (**1, 5'**) and (**7, 2'**) are selected in this example, as shown in the Figure 1.2**.**

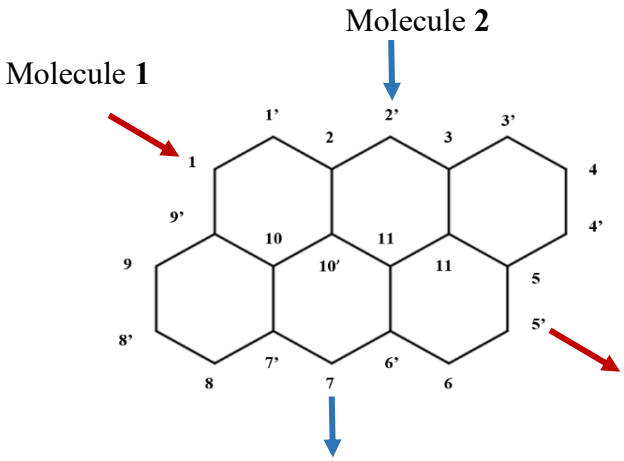

Figure 1.2: Representation of studied Anthanthrene core. Two connectivities for **1:** (**1, 5'-** Red) and **2**: (**2', 7** -blue).

Table 1.3: magic numbers for Anthanthrene core.

M=

	1'	2'	3'	4'	5'	6'	7'	8'	9'	10'	11'
1	-9	7	-4	4	-1	1	-1	1	-1	2	-3
2	-1	-7	4	-4	1	-1	1	-1	1	-2	3
3	1	-3	-4	4	-1	1	-1	1	-1	2	-3
4	-1	3	-6	-4	1	-1	1	-1	1	-2	3
5	1	-3	6	-6	-1	1	-1	1	-1	2	-3
6	-1	3	-6	6	-9	-1	1	-1	1	-2	3
7	3	-9	8	-8	7	-7	-3	3	-3	6	1
8	-6	8	-6	6	-4	4	-4	-6	6	-2	-2
9	6	-8	6	-6	4	-4	4	-4	-6	2	2
10	3	1	-2	2	-3	3	-3	3	-3	-4	1
11	-2	6	-2	2	2	-2	2	-2	2	-4	4

$$\text{MRR}= \frac{G_{7,2'}}{G_{1,5'}} = \frac{(-9)^2}{(-1)^2} = \mathbf{81}\text{ , (Theoretical value).}$$

Next, does this value, 81, agree with the experiment or not?

The experiment below shows the ratio number of the Anthanthrene core. Anthanthrene's measurement is studied for the same molecule with different connectivities represented by **1** and **2,** as shown in Figure 1.2.

The experiment measurement shows that the electrical conductances for 1 and 2 are $10^{-6.7\pm0.7}G_0$ and $10^{-4.8\pm0.6}G_0$, respectively.

As results, the conductance ratio between **1** and **2** can be determined as follow:

$$\frac{G1}{G2} = \frac{10^{-4.8}}{10^{-6.7}} = \mathbf{79}.$$

In summary, the theoretical conductance value (**81**) for **1** and **2** has a good agreement with the experiment value (**79**).

Magic ratio rules for symmetric Anthracene Molecule.

Example 3 aims to show the magic ratio theory for our studied molecule, core anthracene. Anthracene core has been chosen to study [26-27]. Two connectivities are studied in the same molecule. Thus, (**2', 6**) and (**3', 7**) are selected in this example, as shown in the **Figure 1.3**.

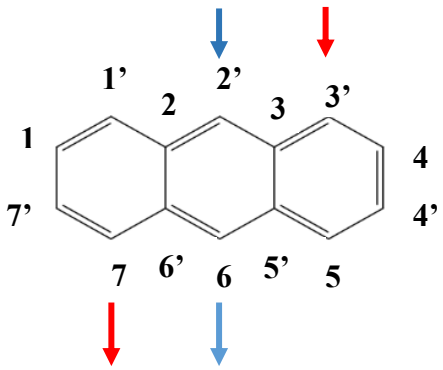

Figure 1.3: Representation of studied anthracene core. Two connectivities (**2', 6)**, (blue) and (**3, 7'**) **(**Red).

Table 1.4: Magic Number Table Mij for anthracene core ($C_{10}H_8$).

$\boldsymbol{C} =$

	1	**2**	**3**	**4**	**5**	**6**	**7**
1'	1	1	0	0	0	0	0
2'	0	1	1	0	0	0	0
3'	0	0	1	1	0	0	0
4'	0	0	0	1	1	0	0
5'	0	0	1	0	1	1	0
6'	0	1	0	0	0	1	1
7'	0	0	0	0	0	0	1

Table 1.5: connectivity table

M=

	1	**2**	**3**	**4**	**5**	**6**	**7**
1'	-3	2	-1	1	-1	1	-1
2'	-1	-2	1	-1	1	-1	1
3'	1	-2	-1	1	-1	1	-1
4'	-1	2	-3	-1	1	-1	1
5'	1	-2	3	-3	-1	1	-1
6'	-2	4	-2	2	-2	-2	2
7'	3	-2	1	-1	1	-1	-3

$$M = det(C) \times C^{-1}$$

$$Det\ (C) = 4$$

$$\text{MRR}= \frac{G_{2',6}}{G_{3',7}} = \frac{(4)^2}{(1)^2} = 16.$$

Table 1.6: the magic ratio for the previous study of Anthracene.

Anthracene 's anchor	Theory $\frac{G}{G_0}$	Theory ratios	Experiment $\frac{G}{G_0}$	Experiment ratios	Ref
2 SMe (1, 9)	1.66 e-4	**15.8**	7.01 e-5	**10.19**	**[26,27]**
2 SMe (1, 5)	1.05 e-5		6.88 e-6		
2 SAc (1, 9)	1.59 e-4	**15.9**	1.28 e-4	**14.22**	
2 SAc (1, 5)	1 e-5		9 e-6		
2 Py (1, 9)	0.9 e-4	**15.7**			
2 Py (1, 5)	0.57 e-5				

In the current study, I will discuss the experiment and theory ratios for the anthracene molecule with the Porphyrin and the graphene sheet in the following parts.

1.2 Thesis Outline

In this thesis, the theoretical studies introduce two-terminal molecular junctions' electrical properties; this can be described as gold electrodes that form gold |molecule| gold structures. Theoretical methods employ density functional theory (DFT). Thus, Chapter 2 provides theoretical concept of DFT and the implementation utilized in this study, mainly the SIESTA code. The second tool is the quantum transport code GOLLUM. To introduce this technique, I present in chapter 3 solutions of Green's functions for infinite and semi-infinite1D chains and the transmission coefficient equations, which forms this code's theoretical basis. The charge transport at the single-molecule scale is investigated. Recently, quantum interference effects have attracted great interest in facilitating the charge transport. Within this framework, I theoretically study two primary results, electrical and thermoelectrical properties of studied structures represented in chapters 4 and 5**.**

In chapter 4**,** I began this chapter by exploring 4 bare anthracene-based molecules, those molecules classified into two connectivities **9, 10** and **1, 5** and two anchor groups including thioether and pyridyl. Then this research was narrowed down to two molecules as two of them do not bind to a graphene sheet. I divide this research into 4 steps. In step-1, I looked only at the bare molecule with the pyridyl anchor groups as the binding energy calculations suggested that the thioether linker does not bind to a graphene sheet. Step-2 explored the case of combining the bare molecules with either **9, 10** or **1, 5** geometries to a finite graphene sheet

(Gr), where the binding energy calculations demonstrated that the pyridyl anchor strongly bind to a Gr. In step-3, I repeated the step-2 procedure however with a porphyrin layer ZnTTP. Eventually, both the graphene sheet and porphyrin complexed to the bare anthracene-based molecules and that was step-4. My theoretical simulations of this research were tested against the measured parameters including the binding energies, conductances and Seebeck coefficients and excellent agreements were found.

Chapter 5, represented a theoretical based on the same molecules that explored in chapter 4, however, in different directions. This research introduced a variety of anchor groups to include alkynyl, thiol and pyridyl. Furthermore, the anthracene-based molecules were chosen to be asymmetric, meaning with different different anchors at the ends of the molecule. This chapter is also constructed in three sections. First-section dealt with the bare molecules, where three asymmetric anthracene-based molecules were nominated such as alkynyl -Py, alkynyl -thiol and Py-thiol. The electronic properties of this sites of molecules were envisaged and assorted as either HOMO- or LUMO-dominated molecules.

The second section i dedicated to combine the bare molecules to a finite graphene sheet (Gr) to form multicomponent and placed it between metallic electrodes. The Gr. pulled out in the junction in several binding locations, however, in each position the anchor and the tip were aligned and passed through a C atom in the sheet. The outcome of this pulling technique is an oscillation in the conductance.

Third section concentrated on the “flipping characteristic” as the molecules are asymmetric when they form multicomponent with the Gr, there will be two multicomponent. For example, an asymmetric molecule with Py and thiol anchors produced Py-graphene multicomponent and thiol-graphene multicomponent (flipping the anchor in regard to the sheet). The flipping

technique yields a positive and negative Seebeck coefficient for the different multicomponent. Switching the sign of the Seebeck coefficient of the same molecule is such an important feature.

1.3 Bibliography

1- Scheer, E. (2013). Visions for a molecular future. *Nature Nanotechnology*, *8*(6), 386.

2- Love, J. C., Estroff, L. A., Kriebel, J. K., Nuzzo, R. G., and Whitesides, G. M. (2005). Self-assembled monolayers of thiolates on metals as a form of nanotechnology. *Chemical reviews*, *105*(4), 1103-1170.

3- Aradhya, S. V., and Venkataraman, L. (2013). Single-molecule junctions beyond electronic transport. *Nature nanotechnology*, *8*(6), 399.

4- Sangtarash, S., Huang, C., Sadeghi, H., Sorohhov, G., Hauser, J., Wandlowski, T., and Lambert, C. J. (2015). Searching the hearts of graphene-like molecules for simplicity, sensitivity, and logic. *Journal of the American Chemical Society*, *137*(35), 11425-11431.

5- Sadeghi, H., Algaragholy, L., Pope, T., Bailey, S., Visontai, D., Manrique, D., and Lambert, C. J. (2014). Graphene sculpturene nanopores for DNA nucleobase sensing. *The Journal of Physical Chemistry B*, *118*(24), 6908-6914.

6- Sadeghi, H., Bailey, S., and Lambert, C. J. (2014). Silicene-based DNA nucleobase sensing. *Applied Physics Letters*, *104*(10), 103104.

7- T. Prodromakis, C. Toumazou, and L. Chua, (2012). Two centuries of memristors, Nature Materials, vol. 11, no. 6, pp. 478–481.

8- Lambert, C. J. (2015). Basic concepts of quantum interference and electron transport in single-molecule electronics. *Chemical Society Reviews*, *44*(4), 875-888.

9- Sadeghi, H., Sangtarash, S., and Lambert, C. J. (2015). Oligoyne molecular junctions for efficient room temperature thermoelectric power generation. *Nano letters*, *15*(11), 7467-7472.

10- Sadeghi, H., Sangtarash, S., and Lambert, C. J. (2015). Enhanced thermoelectric efficiency of porous silicene nanoribbons. *Scientific reports*, *5*(1), 1-7.

11- Aviram, A., and Ratner, M. A. (1974). Molecular rectifiers. *Chemical physics letters*, *29*(2), 277-283.

12- Batra, A., Darancet, P., Chen, Q., Meisner, J. S., Widawsky, J. R., Neaton, J. B., and Venkataraman, L. (2013). Tuning rectification in single-molecular diodes. *Nano letters*, *13*(12), 6233-6237.

13- Lafferentz, L., Ample, F., Yu, H., Hecht, S., Joachim, C., and Grill, L. (2009). Conductance of a single conjugated polymer as a continuous function of its length. *Science*, *323*(5918), 1193-1197.

14- Davis, W. B., Svec, W. A., Ratner, M. A., and Wasielewski, M. R. (1998). Molecular-wire behaviour in p-phenylenevinylene oligomers. *Nature*, *396*(6706), 60-63.

15- Chen, J., Wang, W., Reed, M. A., Rawlett, A. M., Price, D. W., and Tour, J. M. (2000). Room-temperature negative differential resistance in nanoscale molecular junctions. *Applied physics letters*, *77*(8), 1224-1226.

16- Li, C., Pobelov, I., Wandlowski, T., Bagrets, A., Arnold, A., and Evers, F. (2008). Charge transport in single Au vertical bar alkanedithiol vertical bar Au junctions: Coordination geometries and conformational degrees of freedom. *Journal of the American Chemical Society*, *130*(1), 318-326.

17- Hong, W., Manrique, D. Z., Moreno-García, P., Gulcur, M., Mishchenko, A., Lambert, C. J., and Wandlowski, T. (2012). Single molecular conductance of tolanes:

experimental and theoretical study on the junction evolution dependent on the anchoring group. *Journal of the American Chemical Society*, *134*(4), 2292-2304.

18- Sadeghi, H., Sangtarash, S., and Lambert, C. J. (2015). Enhancing the thermoelectric figure of merit in engineered graphene nanoribbons. *Beilstein journal of nanotechnology*, *6*(1), 1176-1182.

19- Sadeghi, H., Bailey, S., and Lambert, C. J. (2014). Silicene-based DNA nucleobase sensing. *Applied Physics Letters*, *104*(10), 103104.

20- Warner, J. H. (2015). Detailed Atomic Structure of Defects in 2D Materials: From Graphene to Transition Metal Dichalcogenides. *Microscopy and Microanalysis*, *21*(S3), 573-574.

21- Rincón-García, L., Ismael, A. K., Evangeli, C., Grace, I., Rubio-Bollinger, G., Porfyrakis, K., and Lambert, C. J. (2016). Molecular design and control of fullerene-based bi-thermoelectric materials. *Nature materials*, *15*(3), 289-293.

22- Li, Y., Baghernejad, M., Qusiy, A. G., Zsolt Manrique, D., Zhang, G., Hamill, J., and Lambert, C. (2015). Three-state single-molecule naphthalenediimide switch: integration of a pendant redox unit for conductance tuning. *Angewandte Chemie*, *127*(46), 13790-13793.

23- Yzambart, G., Rincón-García, L., Al-Jobory, A. A., Ismael, A. K., Rubio-Bollinger, G., Lambert, C. J., and Bryce, M. R. (2018). Thermoelectric Properties of 2, 7-Dipyridylfluorene Derivatives in Single-Molecule Junctions. *The Journal of Physical Chemistry C*, *122*(48), 27198-27204.

24- Massonnet, N., Carella, A., Jaudouin, O., Rannou, P., Laval, G., Celle, C., and Simonato, J. P. (2014). Improvement of the Seebeck coefficient of PEDOT: PSS by chemical reduction combined with a novel method for its transfer using free-standing thin films. *Journal of Materials Chemistry C*, *2*(7), 1278-1283.

25- Rincón-García, L., Ismael, A. K., Evangeli, C., Grace, I., Rubio-Bollinger, G., Porfyrakis, K., and Lambert, C. J. (2016). Molecular design and control of fullerene-based bi-thermoelectric materials. *Nature materials*, *15*(3), 289-293.

26- Wang, X., Bennett, T. L., Ismael, A., Wilkinson, L. A., Hamill, J., White, A. J., and Lambert, C. J. (2020). Scale-up of room-temperature constructive quantum interference from single molecules to self-assembled molecular-electronic films. *Journal of the American Chemical Society*, *142*(19), 8555-8560.

27- Ismael, A., Wang, X., Bennett, T. L., Wilkinson, L. A., Robinson, B. J., Long, N. J., and Lambert, C. J. (2020). Tuning the thermoelectrical properties of anthracene-based self-assembled monolayers. *Chemical science*, *11*(26), 6836-6841.

28- Sedghi, G., García-Suárez, V. M., Esdaile, L. J., Anderson, H. L., Lambert, C. J., Martín, S., and Nichols, R. J. (2011). Long-range electron tunnelling in oligo-porphyrin molecular wires. *Nature nanotechnology*, *6*(8), 517-523.

29- Zhao, X., Huang, C., Gulcur, M., Batsanov, A. S., Baghernejad, M., Hong, W., and Wandlowski, T. (2013). Oligo (aryleneethynylene) s with terminal pyridyl groups: synthesis and length dependence of the tunneling-to-hopping transition of single-molecule conductances. *Chemistry of materials*, *25*(21), 4340-4347.

30- Sadeghi, H., Mol, J. A., Lau, C. S., Briggs, G. A. D., Warner, J., and Lambert, C. J. (2015). Conductance enlargement in picoscale electroburnt graphene nanojunctions. *Proceedings of the National Academy of Sciences*, *112*(9), 2658-2663.

31- Solomon, G. C., Bergfield, J. P., Stafford, C. A., and Ratner, M. A. (2011). When "small" terms matter: Coupled interference features in the transport properties of cross-conjugated molecules. *Beilstein journal of nanotechnology*, *2*(1), 862-871.

32- Bergfield, J. P., Solis, M. A., and Stafford, C. A. (2010). Giant thermoelectric effect from transmission supernodes. *ACS nano*, *4*(9), 5314-5320.

33- Ricks, A. B., Solomon, G. C., Colvin, M. T., Scott, A. M., Chen, K., Ratner, M. A., and Wasielewski, M. R. (2010). Controlling electron transfer in donor− bridge− acceptor molecules using cross-conjugated bridges. *Journal of the American Chemical Society*, *132*(43), 15427-15434.

34- Manrique, D. Z., Huang, C., Baghernejad, M., Zhao, X., Al-Owaedi, O. A., Sadeghi, H., and Lambert, C. J. (2015). A quantum circuit rule for interference effects in single-molecule electrical junctions. *Nature communications*, *6*(1), 1-8.

35- Markussen, T., Schiötz, J., and Thygesen, K. S. (2010). Electrochemical control of quantum interference in anthraquinone-based molecular switches. *The Journal of chemical physics*, *132*(22), 224104.

36- Vazquez, H., Skouta, R., Schneebeli, S., Kamenetska, M., Breslow, R., Venkataraman, L., and Hybertsen, M. S. (2012). Probing the conductance superposition law in single-molecule circuits with parallel paths. *Nature Nanotechnology*, *7*(10), 663-667.

37- Aradhya, S. V., Meisner, J. S., Krikorian, M., Ahn, S., Parameswaran, R., Steigerwald, M. L., and Venkataraman, L. (2012). Dissecting contact mechanics from quantum interference in single-molecule junctions of stilbene derivatives. *Nano letters*, *12*(3), 1643-1647.

38- Geng, Y., Sangtarash, S., Huang, C., Sadeghi, H., Fu, Y., Hong, W., and Liu, S. X. (2015). Magic ratios for connectivity-driven electrical conductance of graphene-like molecules. *Journal of the American Chemical Society*, *137*(13), 4469-4476.

Chapter 2

2. Density Functional Theory

This chapter has shown the mathematical principle of Density Functional Theory (DFT). I will also illustrate general concepts of DFT code SIESTA, which is applied to all studied electronic structure calculations in this thesis. The first step in learning electronic transport to extract the Hamiltonian of an isolated molecule and relax it. We then attach this isolated molecule to metallic electrodes to calculate the transport properties. I will briefly introduce the calculation of the transport properties carried out during an ab initio transport calculation. The details will discuss in chapter 3.

2.1 introduction

DFT is a discipline used mainly by experts in chemistry and physics to research the ground state of interacting many-particle systems such as molecules, atoms, and crystals. It is a computational quantum mechanics method that utilizes many-body systems into one of the non-interacting fermions in an effective field. Similarly, the electrical properties of many interacting particle systems can be described as a function of ground-state density [1, 2]. In 1998, the importance of DFT was affirmed by a Nobel Prize in Chemistry being awarded to Walter Kohn. This was awarded due to his achievements in developing concepts of DFT. DFT is a reliable methodology that has been used for many molecular systems.

Additionally, many books regarding relevant literature elaborating comprehensive descriptions of the principles of density functional theory and its application have been documented [1-6].

The DFT was started by the Thomas-Fermi model back in the 1920s, in which they provided the basic steps to obtain density functionality for total energy based on wave functions [1, 6-8]**.** In addition to the work of Thomas Fermi model, further improvement was made by Dirac, Hartree, Slater, and Fock, nearly four decades after their work was put forward work. The DFT foundation was then given an effective start by the Hohenberg-Kohn theorems and Kohn-Sham methods [1, 3, 4, 7-11]. The primary objective of this chapter is to give a brief introduction to density functional theory and give an outline of the leading mathematical equations as a method of obtaining a solution of the non-relativistic many-particles time-independent Schrödinger equation TISE. This is because the properties of a many-electron system can be determined by using the function of electron density. This chapter will summarize the DFT code 'SIESTA', which has been largely used throughout this Ph.D. research as a theoretical tool to find a way for structure optimization.

2.2 The Schrödinger Equation and Variational Principle.

Non-relativistic many particles system is systematically described by the time-independent, non-relativistic Schrödinger equation in the equation 2.1:

$$\mathrm{H}\Psi_i(\vec{r}_1, \vec{r}_2, \dots, \vec{r}_N, \vec{R}_1, \vec{R}_2, \dots, \vec{R}_M) = E_i\Psi_i(\vec{r}_1, \vec{r}_2, \dots, \vec{r}_N, \vec{R}_1, \vec{R}_2, \dots, \vec{R}_M) \quad (2.1)$$

H is the Hamiltonian operator of a system consisting of *N*-electrons, *M*-nuclei is the interaction of particles, Ψ_i is the wave-function of the state of the system, E_i which describes the numerical value energy of the state. The Hamiltonian operator (H) is:

$$\mathrm{H} = \overbrace{-\frac{\hbar^2}{2m_e}\sum_{i=1}^{N}\nabla_i^2}^{T_e} \tag{2.2}$$

$$\overbrace{-\frac{\hbar^2}{2m_n}\sum_{n=1}^{M}\nabla_n^2}^{T_n} - \overbrace{\frac{1}{4\pi\varepsilon_o}\sum_{i=1}^{N}\sum_{n=1}^{M}\frac{1}{\left|\vec{r}_i - \vec{R}_n\right|}Z_n e^2}^{U_{en}}$$

$$+\overbrace{\frac{1}{4\pi\varepsilon_o}\frac{1}{2}\sum_{i=1}^{N}\sum_{i\neq j}^{N}\frac{e^2}{\left|\vec{r}_i - \vec{r}_j\right|}}^{U_{ee}}$$

$$+\overbrace{\frac{1}{4\pi\varepsilon_o}\frac{1}{2}\sum_{n=1}^{M}\sum_{n\neq n'}^{M}\frac{1}{\left|\vec{R}_n - \vec{R}_{n'}\right|}Z_n Z_{n'} e^2}^{U_{nn}}$$

The equation 2.2: i and j represent the N-electrons while n and n' represent a run over the M-nuclei in the system, m_e and m_n represent the mass of electron and nucleus respectively. Additionally, e and Z_n represent the electron and nuclear charge in the system respectively, while $\vec{r}_i$ and $\vec{R}_n$ is the position of the electrons and nuclei in the system respectively. The equation below ∇_i^2 is the Laplacian operator, mathematically, it is outlined in a Cartesian coordinate ∇_i^2 which is given by the equation below.

$$\nabla_i^2 = \frac{\partial^2}{\partial x_i^2} + \frac{\partial^2}{\partial y_i^2} + \frac{\partial^2}{\partial z_i^2}$$

According to the illustration given by the Eq. (2.2), the terms, T_e is the kinetic energy of electrons, while T_n is denoted as kinetic energy of nuclei in the system. Additionally, the last three terms describe the potential part of the Hamiltonian; the term U_{en} represents the attractive electrostatic interaction between nuclei and electrons in the system. The electron-electron (U_{ee}) and nuclear-nuclear (U_{nn}) are the repulsive part of the potential respectively [1, 3, 6, 9, 13].

The Born-Oppenheimer approximation, which is also referred to as the clamped nuclei approximation can be applied in the analysis because about 99.9% of atom's mass is contained in the nucleus, additionally, the nuclei in the system can be considered fixed as compared to the electrons. This means, for example, concentration of mass of the hydrogen atom is illustrated by the fact that the nucleus weigh about 1800 times more than the electron. In the given case, if the nuclei of the treated atoms are held fixed it indicates that the resulting kinetic energy sums to zero, this directly means that they do not contribute to the full wave-function anymore.

The results of the above assumption is that the Hamiltonian expression of the electron system reduces the Hamiltonian to a different figure, similarly, the electronic Hamiltonian H_{ele} which in a fixed nuclear representation can be given by [1, 3, 6, 13-15]:

$$\mathrm{H}_{ele} = \overbrace{-\frac{\hbar^2}{2m_e}\sum_{i=1}^{N}\nabla_i^2}^{T_e} \overbrace{-\frac{1}{4\pi\varepsilon_o}\sum_{i=1}^{N}\sum_{n=1}^{M}\frac{1}{\left|\vec{r}_i-\vec{R}_n\right|}Z_n e^2}^{U_{en}} + \overbrace{\frac{1}{4\pi\varepsilon_o}\frac{1}{2}\sum_{i=1}^{N}\sum_{i\neq j}^{N}\frac{e^2}{\left|\vec{r}_i-\vec{r}_j\right|}}^{U_{ee}} + \overbrace{\frac{1}{4\pi\varepsilon_o}\frac{1}{2}\sum_{i=1}^{M}\sum_{n\neq n'}^{M}\frac{Z_n Z_{n'} e^2}{\left|\vec{R}_n-\vec{R}_{n'}\right|}}^{U_{nn}} \tag{2.3}$$

Where; the U_{nn} is an obtained constant for the system.

In the above a system, the Schrödinger equation for 'clamped-nuclei' is represented as:

$$\mathrm{H}_{ele}\Psi_{ele} = E_{ele}\Psi_{ele} \tag{2.4}$$

Where; Ψ_{ele} is dependent on the electron coordinates for the system, while the nuclear part enters only dimensionally and does not clearly appear in Ψ_{ele}.

Total energy E_{total} is given as the sum of E_{ele} and the constant nuclear repulsion term for the system which is given as:

$$E_{total} = E_{ele} + U_{nn} \tag{2.5}$$

Wave-function for a system is not an observable quantity, its modulus squared can be written in the form as:

$$|\Psi(\vec{r}_1, \vec{r}_2, \dots, \vec{r}_N)|^2 d\vec{r}_1\, d\vec{r}_2 \dots d\vec{r}_N \tag{2.6}$$

The above expression represents the fact that the probability that electrons 1, 2… *N* are found in the volume elements$d\vec{r}_1\, d\vec{r}_2 \dots\dots d\vec{r}_N$, this is because the electrons are indistinguishable, and this probability is unchangeable if the coordinates of any two of electrons (i and j) are swapped [12]:

$$\left|\Psi(\vec{r}_1, \vec{r}_2, \dots \vec{r}_i, \vec{r}_j, \dots, \vec{r}_N)\right|^2 = \left|\Psi(\vec{r}_1, \vec{r}_2, \dots \vec{r}_j, \vec{r}_i, \dots, \vec{r}_N)\right|^2 \tag{2.7}$$

Because of the reason that electrons are fermions with spins of a half then the value of Ψ must therefore be anti-symmetric with respect to the interchange of the spatial and the spin coordinates as well in any pair of electrons:

$$\Psi(\vec{r}_1, \vec{r}_2, \dots \vec{r}_i, \vec{r}_j, \dots, \vec{r}_N) = -\Psi(\vec{r}_1, \vec{r}_2, \dots \vec{r}_i, \vec{r}_j, \dots, \vec{r}_N) \tag{2.8}$$

A logical result of probability interpretation format of the wave-function is that the integral of equation 2.6 over the full range of all variables gives an output of one**.** This mean, the probability of finding the *N*-electron at any position in a space must be exactly unity,

$$\int \dots \int |\Psi(\vec{r}_1, \vec{r}_2, \dots, \vec{r}_N)|^2 \, d\vec{r}_1 \, d\vec{r}_2 \dots d\vec{r}_N = 1 \qquad (2.9)$$

A wave-function that meets the requirements for equation (2.9) is a normalized one.

Since the Schrödinger wave-equation does not have an exact solution, several theories have been developed to fulfil this objective; this effort start with Hartree, Hartree-Fock and many others. A large number of these theories were based on a significant theoretical principle referred to as variational principle of the wave-function where this principle leads an analysts on how to look for solutions by using suitable trial wave-functions Ψ_{Tri} [1, 2, 5, 6, 12]. The above principle is meaningful in the study of the ground state, but is not very fruitful in the study of excited states. When a system is in the state Ψ_{Tri}, the expectation value of the energy is given by the expression:

$$\langle E_{Tri} \rangle = \frac{\int \Psi_{Tri} \, \mathrm{H} \, \Psi^*_{Tri} \, d\vec{r}}{\int \Psi_{Tri} \; \Psi^*_{Tri} \, d\vec{r}} \qquad (2.10)$$

Variational principle that is given in the equation 2.10 implies that the energy computes as the expectation value of the Hamiltonian operator from any Ψ_{Tri} that is an upper bound of the true ground-state energy Ψ_{GS}. Suppose Ψ_{Tri} is normalized as per the equation 2.9 while Ψ_{Tri} then it equals to the ground state ($\Psi_{Tri} = \Psi_{GS}$). This indicates that entity E_{Tri} is equal to the exact

ground state energy E_{GS}, additionally, we can reconfigure the equation 2.10 for the ground state as:

$$\langle E_{GS} \rangle = \int \Psi_{GS} \, \mathrm{H} \, \Psi_{GS}^{*} \, d\vec{r} \qquad (2.11)$$

From the normalized Ψ_{Tri} we can clarify that $E_{Tri} > E_{GS}$ or $E_{Tri} = E_{GS}$. The best choice for E_{Tri} is therefore the one in which E_{Tri} is reduced [3, 4, 6].

2.3 The Hohenberg-Kohn Theorems.

Essentially, DFT is based on Hohenberg-Kohn theorems; whereby in 1964, Hohenberg and Kohn validated the use of the electron density $n(\vec{r})$ to calculate the ground state energy. These theorems can be clarified by two powerful statements.

The first theory: For any interacting many particle systems in external potential $V_{ext}(\vec{r})$, density of the system is uniquely defined. Additionally, this can be computed because it illustrates that the density $n(\vec{r})$ is used instead of the potential as a basic function uniquely giving a description of the system, and be stated as the ground state density $n_{GS}(\vec{r})$ that is expressly relied upon to establish the potential up to an arbitrary constant [6, 10, 17, 19].

This theorem is approved by considering two different external potentials:

$V_{ext}(\vec{r})_{(1)}$And $V_{ext}(\vec{r})_{(2)}$.The two differ by more than a constant but results in the same ground state density $n_{GS}(\vec{r})$. It is clear that these the above two potentials correspond to

different Hamiltonians which are $H_{ext}[(\vec{r})]_{(1)}$ and $H_{ext}[(\vec{r})]_{(2)}$, and they give rise to distinct wave-functions $\Psi_{ext}[(\vec{r})]_{(1)}$ and $\Psi_{ext}[(\vec{r})]_{(2)}$.

Since ground state of the systems is the same and going according to the variational principle which informs us that there is no wave-function that gives energy that is less than the energy of $\Psi_{ext}[(\vec{r})]_{(1)}$ for $H_{ext}[(\vec{r})]_{(1)}$.

This is expressed as:

$$\langle E_{(1)} \rangle = \int \Psi_{(1)}\, H_{(1)}\, \Psi^{*}_{(1)}\; d\vec{r} < \int \Psi_{(2)}\, H_{(2)}\, \Psi^{*}_{(2)}\; d\vec{r} \qquad (2.12)$$

Therefore, for non-degenerate ground state with regard to identical ground state densities for the two Hamiltonians, the equation 2.12 is given as:

$$\int \Psi_{(2)}\, H_{(1)}\, \Psi^{*}_{(2)}\; d\vec{r}$$

$$= \overbrace{\int \Psi_{(2)}\, H_{(2)}\, \Psi^{*}_{(2)}\; d\vec{r}}^{\langle E_{(2)} \rangle} \qquad (2.13)$$

$$+ \int \left\{ [V_{ext}(\vec{r}\,)]_{(1)} - [V_{ext}(\vec{r}\,)]_{(2)} \right\} n_{GS}(\vec{r})\, d\vec{r}$$

Exchanging of the labels in the equation 2.13, we obtain:

$$\int \Psi_{(1)}\, H_{(2)}\, \Psi^{*}_{(1)}\, d\vec{r} \qquad (2.14)$$

$$= \overbrace{\int \Psi_{(1)}\, H_{(1)}\, \Psi^{*}_{(1)}\; d\vec{r}}^{\langle E_{(1)} \rangle}$$

$$+ \int \{[V_{ext}(\vec{r}\,)]_{(2)} - [V_{ext}(\vec{r}\,)]_{(1)}\}\, n_{GS}(\vec{r})\, d\vec{r}$$

By addition of the equations 2.13 and 2.14, the results obtained are given by:

$$\langle E_{(1)} \rangle + \langle E_{(2)} \rangle < \langle E_{(2)} \rangle + \langle E_{(1)} \rangle \qquad (2.15)$$

The equation (2.15) shows a logical contradiction. Hence, the theorem has been confirmed by reductio ad absurdum.

The second theorem avails a variational ansatz for obtaining the value for $n(\vec{r})$, this is applied in searching for $n(\vec{r})$ which minimizes the energy. This is also meant to say that expressing in terms of the density $n(\vec{r})$, we can describe a universal functional expression for the given energy $E[n(\vec{r})]$. The ground state energy of the system ($V_{ext}(\vec{r}\,)$) is the global minimum value of this functional and the density $n(\vec{r})$ which minimizes the function, it also signifies the actual ground state density $n_{GS}(\vec{r})$.

Regarding the second proof, the first theorem informs us that the total energy of the system is expressed as a function of the density $n(\vec{r})$ and is provided by:

$$E_{total}[n(\vec{r})] =$$

$$\overbrace{T_{int}[n(\vec{r}\,)] + \underbrace{U_{ee}[n(\vec{r}\,)]}_{\substack{=zero,\ for \\ non-interacting \\ system}}}^{F_{H-K}[n(\vec{r}\,)]} + \int V_{ext}(\vec{r}\,)\; n(\vec{r}\,)\, d\vec{r} \qquad (2.16)$$

The first two terms of equation (2.16) ($F_{H-K}[n(\vec{r})]$) are kinetic energy (T_{int}) and electron-electron interaction energy (U_{ee}), they are evaluated as the same for the whole system. Hence $F_{H-K}[n(\vec{r})]$ is a universal function which has been uniquely illustrated as the Holy Grail of density functional theory[12]. Taking the assumption that the system is in the ground state, the energy can be particularly illustrated by the ground state density $n_{GS}(\vec{r})$ as:

$$\langle E_{GS}\rangle = \langle E[n_{GS}(\vec{r})]\rangle = \int \Psi_{GS}\, H_{GS}\, \Psi_{GS}^{*}\; d\vec{r} \qquad (2.17)$$

According to variational principle, the ground state energy which has a direct correspondence to the ground state density is the minimum energy and any different density will essentially provide a higher energy:

$$\langle E_{GS}\rangle = \langle E[n_{GS}(\vec{r})]\rangle$$

$$= \int \Psi_{GS}\, H_{GS}\, \Psi_{GS}^{*}\; d\vec{r} < \int \Psi\, H\, \Psi^{*}\; d\vec{r}$$

$$= \langle E[n(\vec{r})]\rangle \quad = \langle E\rangle$$

Once we have evaluated the functional$F_{H-K}[n(\vec{r})]$, we can compute the total energy to be minimized with respect to variations in the density function as shown in the equation 2.16. It results in finding the exact ground state properties of the system that we are pursuing, for most practical calculations, the direct minimization does not give a vivid guide to the ground state energy as provided by Kohn-Sham method.

2.4 Kohn-Sham Method and Self-Consistent Field SFC.

Efforts of Kohn and Sham observed that Hohenberg-Kohn theory is usable at both interacting and non-interacting systems. Density function theory (DFT) is skeptical at giving an

elaboration on interacting many particles problem. The non-interacting system has one great advantage over the interacting system because it is easily used in finding the ground-state energy for a non-interacting system. Kohn and Sham developed the idea in 1965, they found out that it is possible to replace the original Hamiltonian of the system by an effective Hamiltonian (H_{eff}) of the non-interacting system in an effective external potential$V_{eff}(\vec{r})$, they also added that the system gives rise to the same ground state density as the initial system. There is no clear procedure for performing the calculations, the outcome of the efforts of Kohn-Sham method is considered as an ansatz, significantly, it is considerably easier to solve it than the non-interacting problem. Kohn-Sham method is founded on the Hohenberg-Kohn universal density [6, 9, 10, 20]:

$$F_{H-K}[n(\vec{r})] = T_{int}[n(\vec{r})] + U_{ee}[n(\vec{r})] \qquad (2.18)$$

The Hohenberg-Kohn functional for non-interacting electrons in a system can be scaled down to compute only the kinetic energy. Additionally, the energy function of the Kohn-Sham ansatz $F_{K-S}[n(\vec{r})]$ in contrast with the computation evaluated in the equation 2.16 is thereby given the mathematical computation below:

$$F_{K-S}[n(\vec{r})] = T_{non}[n(\vec{r})] + E_{Hart}[n(\vec{r})] + \int V_{ext}(\vec{r})\ n(\vec{r})\ d\vec{r} + E_{xc}[n(\vec{r})]. \qquad (2.19)$$

Where T_{non} denotes the kinetic energy of the non-interacting system that differs from T_{int} for interaction system given by the equation 2.16, while E_{Hart} denotes the classical electrostatic energy also referred to as classical self-interaction energy of the electron gas which is linked

to the density $n(\vec{r})$ in the system. The term E_{xc} in the system is the exchange-correlation energy functional and given by:

$$E_{xc}[n(\vec{r})]=F_{H-K}[n(\vec{r})-\overbrace{\frac{1}{2}\int\frac{n(\vec{r}_1)n(\vec{r}_2)}{|\vec{r}_1-\vec{r}_2|}d\vec{r}_1 d\vec{r}_2}^{E_{Hart}[n(\vec{r})]}- \quad (2.20)$$

$T_{non}[n(\vec{r})]$

In the equation 2.19, the first three consecutive terms can be trivially cast into a functional form. Conversely, this is given generally with no exact functional form for the E_{xc}. In the last couple of years in the recent past, multiple efforts have been intensively explored into finding a better computation of E_{xc}. At this time, the physical properties of a large variety of solid-state systems and molecules can investigate and predict by the functional. Additionally, for the last three terms in the equation 2.19, the functional derivatives are taken to construct an effective single particle potential $V_{eff}(\vec{r})$:

$$V_{eff}(\vec{r}) = V_{ext}(\vec{r}) + \frac{\partial E_{Hart}[n(\vec{r})]}{\partial n(\vec{r})} + \frac{\partial E_{xc}[n(\vec{r})]}{\partial n(\vec{r})} \quad (2.21)$$

Significantly, we can logically use this potential to give the Hamiltonian of the single particle:

$$H_{K-S} = T_{non} + V_{eff} \quad (2.22)$$

The Schrödinger equation, for this Hamiltonian, can obtained by:

$$[T_{non} + V_{eff}]\Psi_{K-S} = E\Psi_{K-S} \quad (2.23)$$

Expression represented by the equation 2.23 is referred to as Kohn-Sham equation. Additionally, the ground state density $n_{GS}^{K-S}(\vec{r})$ corresponds to the ground state wave-function Ψ_{GS}^{K-S} by which its evaluation minimizes the Kohn-Sham functional subject to the ortho-normalization constraints $\langle \Psi_i | \Psi_j \rangle = \delta_{ij}$; it is established by a self-consistent calculation.

Density functional theory (DFT) makes significant use of a self-consistent field procedure, an example is that which supposed that E_{Hart} and E_{xc} can be precisely calculated. The major challenge now is that V_{eff} cannot be calculated until the correct ground state density is determined, the actual density can't be determined from the Kohn-Sham wave-functions until the equation 2.23 is solved to obtain the actual value of V_{eff} for a particular system. Therefore, the circular problem can be effectively determined by carrying out a self-consistent cycle as shown in the Figure 2.1.

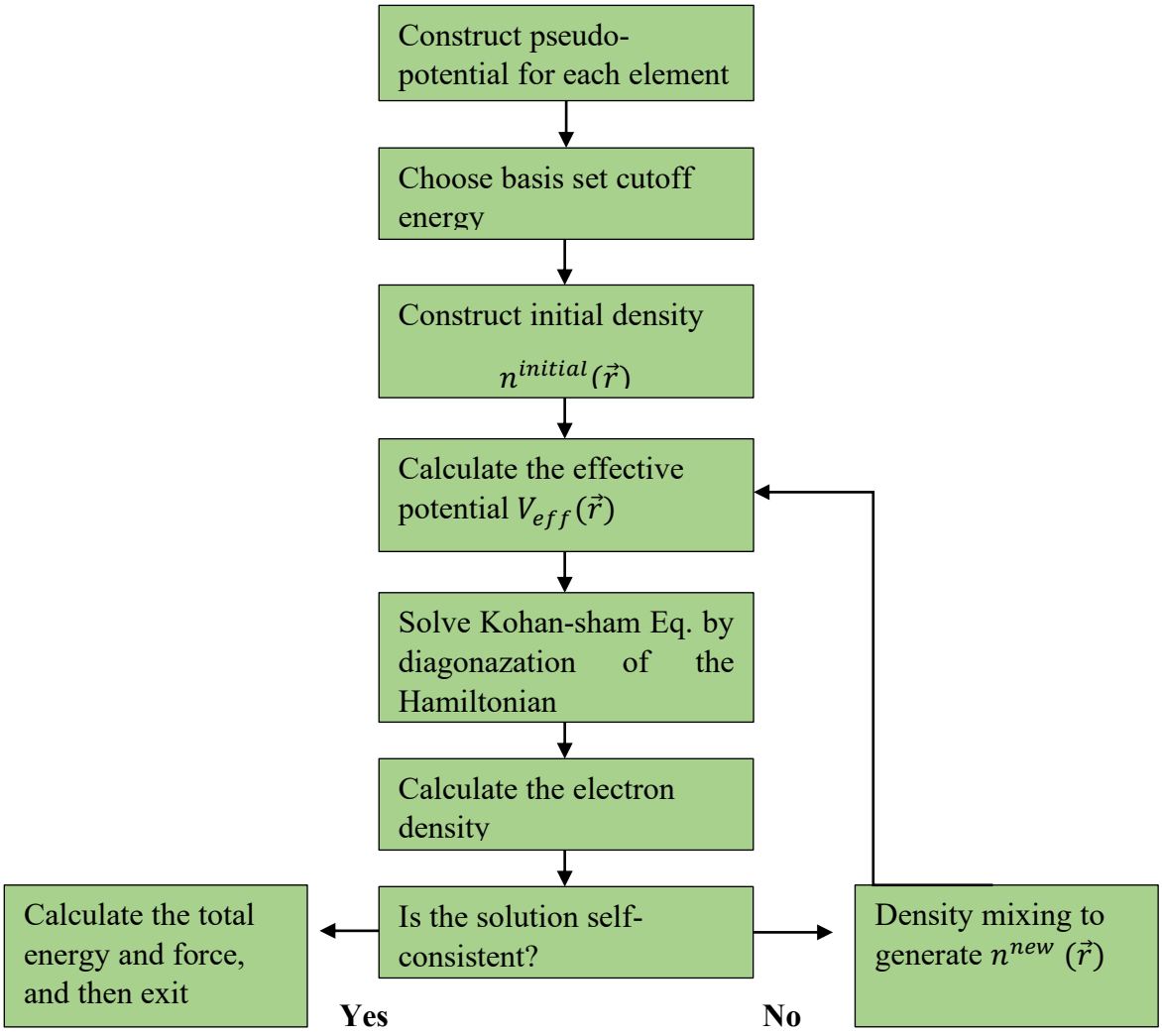

Figure 2.1: A Schematic illustration of the self-consistent DFT cycle.

According to the figure 2.1, the primary step in the study is to generate the pseudo-potential which represents electrostatic interaction between the valence electrons, the nuclei and core electrons in a system. The following step is to make the required basis set with a selected kinetic energy cutoff to be plugged in; this is a step that is designed deliberately to broaden density functional quantities.

Obviously, the energy functional can be fully calculated if the system's density is known. A trial electronic density $n^{initial}(\vec{r})$ is considered as an initial guess. Thus, the following quantity can be calculated by using the initial guess:

$$G = E_{Hart}[n^{initial}\,(\vec{r})] + E_{xc}[n^{initial}\,(\vec{r})] \qquad (2.24)$$

The parameters $\frac{\partial G}{\partial n^{initial}\,(\vec{r})}$ and the effective potential V_{eff} is determined. The effectiveV_{eff} potential is used to obtain a solution for Kohn-Sham equation 2.23 which provides an outline to a solution of the electron Hamiltonian. Upon obtaining the Hamiltonian, it is subsequently diagonalised to obtain the Eigen functions and the new electron density$n^{new}(\vec{r})$. The term $n^{new}(\vec{r})$ is closer to true ground state and it is verified.

For self-consistency, if it is found out that new updated electron density $n^{new}(\vec{r})$ agrees numerically with the density $n^{initial}\,(\vec{r})$ used to build the Hamiltonian at the beginning of the SCF cycle where one terminates at the end of the loop. It follows then that we exit the operations, and calculate all the desired converged quantities, that includes the total energy, the electronic band structure, and density of states. Conversely, the new density $n^{new}(\vec{r})$ does not match with the initial density$n^{initial}\,(\vec{r})$, one has to generate a new input density and begins another SCF cycle: it then follows again that one has to build a new density-dependent Hamiltonian that is used to calculate the density and verify its self-consistency [3, 17, 23].

The illustration of the Kohn-Sham approach clearly shows that a complicated multiple body system can be mapped onto a set of simple non-interacting equations precisely as it can be if the exchange correlation functional is known. It is notable that, the exchange-correlation functional is undetermined precisely, thus approximations need to be considered.

2.5 The Exchange-Correlation Potential.

The DFT is a very reliable and proven method used in the analysis although it still uses an approximation for the kinetic energy functional and the exchange-correlation functional in terms of the density for studied the system. Significantly huge amount of efforts have been oriented at finding reliable expressions for those functionals. The most commonly utilized exchange-correlation functional approximations are the Local Density Approximation (LDA) that depends primarily on the density, and more complicated Generalized Gradient Approximation (GGA) that includes the derivative of the density. This GGA contains information about the environment hence making it is semi-local.

2.6 Local Density Approximation (LDA).

According to Kohn-Sham theory, the functional E_{xc} parameter could be calculated in a homogenous electron gas to approximate the multiple body particle problem as a less complicated system [11]. Kohn-Sham showed in the studies that by slowly but systematically varying the density of a system, the functional E_{xc} at point $\vec{r}$ can be represented as acting in a uniform density. Additionally, the E_{xc} functional is given by a uniform electron gas $E_{xc}^{homo}[n(\vec{r})]$ with a density $n(\vec{r})$.

It is generally that the local density approximation (LDA) does not work for systems with which they are largely dominated by electron-electron interactions. Nonetheless, LDA assumes that the density is a constant a local region around any considered position.

The local density approximation (LDA) is shown by the expression for $E_{xc}^{LDA}[n(\vec{r})]$ in the illustration below.

$$E_{xc}^{LDA}[n(\vec{r})] = \int E_{xc}^{homo}[n(\vec{r})]n(\vec{r})d\vec{r} \qquad (2.25)$$

The exchange-correlation energy $E_{xc}^{homo}[n(\vec{r})]$ can be separated into two different parts; that is as the sum of the exchange$E_{x}^{homo}[n(\vec{r})]$ and the correlation energies$E_{c}^{homo}[n(\vec{r})]$; this can be found separately. Thus, the exchange-correlation energy $E_{xc}^{homo}[n(\vec{r})]$ can be evaluated as:

$$E_{xc}^{homo}[n(\vec{r})] = E_{x}^{homo}[n(\vec{r})] + E_{c}^{homo}[n(\vec{r})] \qquad (2.26)$$

Analytically, the exchange term can be found; it is well determined and can be found in many academic books: [6, 12]

$$E_{x}^{homo}[n(\vec{r})] = -\frac{3}{4}\left(\frac{3n(\vec{r})}{\pi}\right)^{1/3} \qquad (2.27)$$

Correlation energy for the system ($E_{c}^{homo}[n(\vec{r})]$) term cannot be evaluated for analytically, but it can be obtained precisely utilizing numerical steps. The most prevalent and accurate method was done by Ceperly and Alder (CA) utilizing quantum Monte-Carlo simulations. There are multiple interpretations of the Monte Carlo data, an example is that the most used model was calculated by Perdew and Punger (PZ), who fitted the numerical data into an analytical expression and obtained [25, 26].

$$E_{c}^{homo}[n(\vec{r})]=$$

$$\begin{cases} -0.048 + 0.031\,ln(r_o) - 0.0116\,r_o + 0.002\;ln(r_o) & if\ r_o < 1 \\ -\frac{0.1423}{(1+1.9529\sqrt{r_o}+0.3334\,r_o} & if\ r_o > 1 \end{cases} \qquad (1.28)$$

The above equation is done for values of $r_0 > 1$ and that of $r_0 < 1$. Where r_o denotes the average radius of the electrons in the homogenous electron gas. r_0 defined as$(\frac{3}{4\pi n})^{1/3}$.

The local density approximation (LDA) is simple although it is a well-known powerful functional which is accurate for graphite and carbon nanotubes where the electron density does not rapidly change. For atoms with *d* and *f* orbitals, a large error is predicted. The above functional to some reasonable extent has many problems, an example is that the band gap in semiconductors and insulators is typically not accurate with a large error within the range of 0.5 to 2eV or 10-30%. For the above reason it is highly appropriate to utilize better functional [25, 27, 28].

2.7 Generalized Gradient Approximation (GGA).

Local density function (LDA) considers all systems as units of homogenous systems, but the reality is that the systems are non-homogeneous. For one to constructively take this into account, a step may be taken beyond the LDA to expand it by including derivative of the density into the exchange-correlation functional. The workable way to do this is to include the gradient and the higher spatial derivatives of the total charge density.

$$\text{I.e. } (|\nabla n(\vec{r})|, |\nabla^2 n(\vec{r})|, \ldots)$$

The total charge density is evaluated with the help of higher spatial derivatives into the approximation layout. The above functional is referred to as the generalized gradient approximation (GGA). For this scenario, there is conclusive expression for the exchange part of the functional and hence it has to be calculated along with the correlation contributions using

numerical analysis methods. Exactly as in the case of the local density function (LDA) many parameterizations are available for the exchange-correlation energies in the generalized gradient approximation (GGA) [29-32].

In this particular part, we will address the proposed functional from which is put forward by (PBE) **P**erdew, **B**urke and **E**rnzerhof [29]. There are two separated expressions in the given parameterization, the first expression is the exchange $E_x^{GGA}[n(\vec{r})]$ and demonstrated by:

$$E_x^{GGA}[n(\vec{r})]E_x^{GGA}[n(\vec{r})] = \int n(\vec{r})\, E_x^{homo}[n(\vec{r})]\; F_x(s)d\vec{r} \qquad (2.29)$$

Additionally,

$$F_x(s) = 1 + \kappa - \frac{\kappa}{(1+\mu s^2)/\kappa}$$

Where $F_x(s)$ is referred to as the enhancement factor, $\kappa = 0.804$, $\mu = 0.21951$, $s = |\nabla n(\vec{r})/2k_s n(\vec{r})|$ denotes the dimensionless density gradient, $k_s = \sqrt{\frac{4\,k_{T-F}}{\pi a_o}}$, and $k_{T-F} = \frac{(12/\pi)^{1/3}}{\sqrt{r_s}}$ is the Thomas-Fermi screening wavenumber, r_s is the local Seitz radius.

The next expression is the correlation energy $E_x^{GGA}[n(\vec{r})]$.

The correlation energy $E_x^{GGA}[n(\vec{r})]$ is expressed by:

$$E_c^{GGA}[n(\vec{r})] = \int (E_c^{homo}[n(\vec{r})] + \chi\,[n(\vec{r})])d\vec{r} \qquad (2.30)$$

$$\chi\,[n(\vec{r})] = \frac{e^2}{a_o}\,\gamma\, ln\left(1 + \frac{\beta}{\gamma}\,t^2\,\frac{1+At^2}{1+At^2+A^2t^4}\right),$$

$$A = \frac{\beta}{\gamma}\,[\,e^{\left(\frac{E_c^{homo}[n(\vec{r})]}{\gamma}\right)^{-1}}\,]^{-1}$$

Where: $\gamma = (1 - ln(2)/\pi^2,\ \ t = |\nabla n(\vec{r})/2k_{T-F}n(\vec{r})|$ is another dimensionless density gradient,

$\beta = 0.066725$, and $a_0 = \frac{\hbar}{me^2}$.

LDA and GGA are the two most preferred and used approximations for the estimation of exchange-correlation energies in the DFT. Similarly, there are several other functionals that dominate both LDA and GGA. In the illustration, it is mathematically true that there is no robust theory for the validity of these functionals. It is calculated through testing the functional for various materials over a large range of systems then compared with results of provable empirical information for similar cases.

2.8 SIESTA.

In this thesis all calculations were done by the implementation of DFT in the SIESTA code. The calculations are used to obtain a relaxed geometry of the studied structures and to carry out the calculations to investigate their electronic properties. SIESTA is a common acronym that was obtained from the ***S***panish ***I***nitiative for ***E***lectronic ***S***imulations with ***T***housands of ***A***toms. The concept of SIESTA is a self-consistent density functional theory (DFT) method that utilize norm-conserving pseudo-potentials and a **L**inear **C**ombination of **A**tomic **O**rbital **B**asis set (LCAOB) to obtain dependable outcomes for the calculations [33-40] . There are significantly two different modes to perform density function theory (DFT) simulations using SIESTA. The first one is that in which a conventional self-consistent field diagonalisation method to solve the Kohn-Sham equations while the second one is that whereby direct minimization of a modified energy functional [36]. This section is meant to give a description of some of the SIESTA's components and how they are implemented within the given code.

2.11 Bibliography

1. Argaman, N. and G. Makov, (1998). *Density Functional Theory--an introduction.* arXiv preprint physics/9806013.
2. Dronskowski, R. (2005). *Computational chemistry of solid-state materials* (Vol. 300). Weinheim, Germany: Wiley-VCH.
3. Eschrig, H. (2003). *The fundamentals of density functional theory* (Vol. 2). Leipzig: Edition am Gutenbergplatz.
4. Kohn, W., Becke, A. D., and Parr, R. G. (1996). Density functional theory of electronic structure. *The Journal of Physical Chemistry*, *100*(31), 12974-12980.
5. Martin, R. M. (2020). *Electronic structure: basic theory and practical methods*. Cambridge university press.
6. Parr, R.G. and Y. Weitao. (1994) *Density-functional theory of atoms and molecules*. Vol. 16., Oxford University Press, USA.
7. Kumar, A. (2012). A Brief Introduction to Thomas-Fermi Model in Partial Differential Equations.
8. Lieb, E. H. (1982). Erratum: Thomas-Fermi and related theories of atoms and molecules. *Reviews of Modern Physics*, *54*(1), 311.
9. Gross, E.K. and R.M. Dreizler. (1995). *Density functional theory*. Vol. 337: Springer.
10. Hohenberg, P., and Kohn, W. (1964). Inhomogeneous electron gas. *Physical review*, *136*(3B), B864.
11. Kohn, W., and Sham, L. J. (1965). Self-consistent equations including exchange and correlation effects. *Physical review*, *140*(4A), A1133.

12. Koch, W. and M.C. Holthausen.(2001). *A chemist's guide to density functional theory*. Vol. 2. : Wiley-Vch Weinheim.
13. Geerlings, P., De Proft, F., and Langenaeker, W. (2003). Conceptual density functional theory. *Chemical reviews*, *103*(5), 1793-1874.
14. Eschrig, H., Koepernik, K., and Chaplygin, I. (2003). Density functional application to strongly correlated electron systems. *Journal of Solid-State Chemistry*, *176*(2), 482-495.
15. Ziesche, P., and Tasnádi, F. (2004). Methods for electronic-structure calculations: Overview from a reduced-density-matrix point of view. *International journal of quantum chemistry*, *100*(4), 495-508.
16. Thomas, L. H. (1927, January). The calculation of atomic fields. In *Mathematical proceedings of the Cambridge philosophical society* (Vol. 23, No. 5, pp. 542-548). Cambridge University Press.
17. Burke, K. (2007). *the ABC of DFT.* Department of Chemistry, University of California.
18. Walker, B. G., Molteni, C., and Marzari, N. (2004). Ab initio molecular dynamics of metal surfaces. *Journal of Physics: Condensed Matter*, *16*(26), S2575.
19. Kohn, W.(1999) .*Nobel Lecture: Electronic structure of matter—wave functions and density functionals*.* Reviews of Modern Physics,Vol. 71, No. 5: p. 1253-1266.
20. Levy, M. (1982). Electron densities in search of Hamiltonians. *Physical Review A*, *26*(3), 1200.
21. Lima, N. A., Oliveira, L. N., and Capelle, K. (2002). Density-functional study of the Mott gap in the Hubbard model. *EPL (Europhysics Letters)*, *60*(4), 601.
22. March, N.H. (1975).*Self-consistent fields in atoms*.

23. Kohn, W., and Sham, L. J. (1965). Self-consistent equations including exchange and correlation effects. *Physical review*, *140*(4A), A1133.
24. Ceperley, D. M., and Alder, B. J. (1980). Ground state of the electron gas by a stochastic method. *Physical review letters*, *45*(7), 566.
25. Perdew, J. P., and Zunger, A. (1981). Self-interaction correction to density-functional approximations for many-electron systems. *Physical Review B*, *23*(10), 5048.
26. Naghavi, S. S. (2010). *Theoretical study of correlated systems using hybrid functionals* (Doctoral dissertation, Ph. D. Thesis, Johannes Gutenberg-Universität, Mainz).
27. Hedin, L., and Lundqvist, S. (1970). Effects of electron-electron and electron-phonon interactions on the one-electron states of solids. In *Solid state physics* (Vol. 23, pp. 1-181). Academic Press.
28. Vosko, S. H., Wilk, L., and Nusair, M. (1980). Accurate spin-dependent electron liquid correlation energies for local spin density calculations: a critical analysis. *Canadian Journal of physics*, *58*(8), 1200-1211.
29. Perdew, J. P., Burke, K., and Ernzerhof, M. (1996). Generalized gradient approximation made simple. *Physical review letters*, *77*(18), 3865.
30. Becke, A. D. (1988). Density-functional exchange-energy approximation with correct asymptotic behavior. *Physical review A*, *38*(6), 3098.
31. Hammer, B. H. L. B., Hansen, L. B., and Nørskov, J. K. (1999). Improved adsorption energetics within density-functional theory using revised Perdew-Burke-Ernzerhof functionals. *Physical review B*, *59*(11), 7413.
32. Perdew, J. P., and Wang, Y. (1992). Accurate and simple analytic representation of the electron-gas correlation energy. *Physical review B*, *45*(23), 13244.

33. Soler, J. M., Artacho, E., Gale, J. D., García, A., Junquera, J., Ordejón, P., and Sánchez-Portal, D. (2002). The SIESTA method for ab initio order-N materials simulation. *Journal of Physics: Condensed Matter*, *14*(11), 2745.
34. Sánchez-Portal, D., Ordejon, P., Artacho, E., and Soler, J. M. (1997). Density-functional method for very large systems with LCAO basis sets. *International journal of quantum chemistry*, *65*(5), 453-461.
35. E. Artacho, J.D.G., A. Junquera, R. M. Martin, P. Ordejon, D. Sanchez-Portal, and J. M. Soler. 2(011). *SIESTA 3.1 User's Guide*.
36. Ordejón, P., Drabold, D. A., Grumbach, M. P., and Martin, R. M. (1993). Unconstrained minimization approach for electronic computations that scales linearly with system size. *Physical Review B*, *48*(19), 14646.
37. Kleinman, L., and Bylander, D. M. (1982). Efficacious form for model pseudopotentials. *Physical Review Letters*, *48*(20), 1425.
38. Hamann, D. R., Schlüter, M., and Chiang, C. (1979). Norm-conserving pseudopotentials. *Physical Review Letters*, *43*(20), 1494.
39. Troullier, N., and Martins, J. L. (1991). Efficient pseudopotentials for plane-wave calculations. *Physical review B*, *43*(3), 1993.
40. Troullier, N., and Martins, J. (1990). A straightforward method for generating soft transferable pseudopotentials. *Solid State Communications*, *74*(7), 613-616.

Chapter 3

3. Theory of single particle transport

After representing the density Functional Theory concept for an isolated molecule's electronic structure, the next step is to link the isolated molecule to semi-infinite leads and then compute the probability of transmission through the system. This can be explained by using Green's function scattering equation.

Here, I will discuss the methods based on scattering theory and Green's function methods. These methods describe the electric and thermoelectric properties of nanosized systems placed between two metallic electrodes.

3.1 Introduction

As the primary numerical tool for studying a range of molecular geometrics, single-particle transport theory is introduced and includes a detailed investigation of electronic properties, [1]. The focus of molecular electronics is to understand molecular junctions' electronic structure. This molecule is connected between electrodes, and ballistic transport occurs through the molecules' energy levels. The lead and molecule are coupled weakly compared to an intra-electrode and inter-molecular binding strengths. One of the main problems in molecular electronics is how to bind the molecule to metallic or some other electrodes to probe its electronic properties. A scattering mechanism is involved because of the movement from the electrode to molecule and from molecule to electrode. The scattering mechanism from the electrode and the molecular bridge can be described by using a general Green's function formalism which successfully achieves this process. In this chapter, the derivation of the Landauer formula will be discussed, then a basic procedure of a retarded Green's function will be added, which is valid for a one-dimensional tight-binding chain. It is seen that the Green’s function is directly linked to the transmission coefficient via the scattering area by breaking the periodicity of this lattice at a single link.

3.2 The Landauer Formula

To describe the transport to describe transport phenomena, The Landauer formula**,** [1-4], is used, and that happened in ballistic mesoscopic systems and is applicable for phase coherent systems, in which a single wave function sufficiently explains electronic flow resulting in an equation or formula that relates the conductance of system to the S-matrix of a scattering region connected to two semi-infinite leads. This method will be discussed in this chapter to calculate the transmission properties.

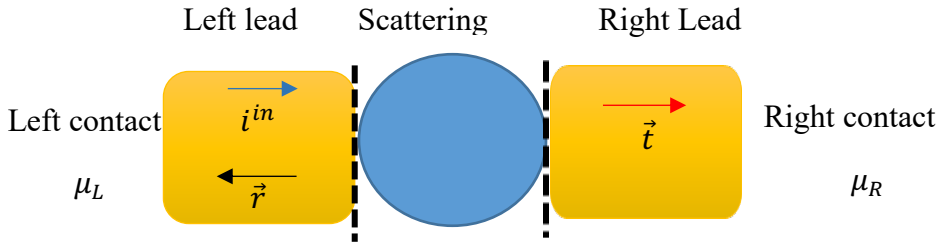

Figure 3.1: A mesoscopic scatterer linked to contacts. Where μ_L and μ_R are the chemical potential in the left and right lead respectively. When an incident wave i^{in} collides with the scatterer from the left, the wave will be transmitted to the right with probability $T = |\vec{t}|^2$ and reflected with probability $R = |\vec{r}|^2$. The fact that the incident electrons must be either reflected or transmitted, thus the probability conservation is $T + R = 1$.

To understand the formula's main principles, I begin by considering a mesoscopic scatterer connected to two contacts, which work as electron reservoirs, resulting from two ideal ballistic leads as shown on the Figure 3.1. The reservoirs 3 are limited to all inelastic relaxation methods. These reservoirs contain slightly chemically different potentials that move electrons

from the left reservoir to the right. In the case of one open channel, the zero-temperature incident electric current produced by the potential chemical difference:

$$\delta \mathrm{I} = \mathrm{e} v_g \left(\frac{\partial \mathrm{n}}{\partial \mathrm{E}} \right) (\mu \mathrm{L} - \mu \mathrm{R}) \tag{3.1}$$

Where, e denotes the electronic charge, v_g is the group velocity, and $\partial n/\partial E$ is the density of states (DOS). The system is defined as one dimensional, then we can write:

$$\frac{\partial \mathrm{n}}{\partial \mathrm{E}} = \frac{\partial \mathrm{n}}{\partial \mathrm{k}} \frac{\partial \mathrm{k}}{\partial \mathrm{E}} = \frac{\partial \mathrm{n}}{\partial \mathrm{k}} \frac{1}{v\hbar} \tag{3.2}$$

$$\frac{\partial \mathrm{n}}{\partial \mathrm{k}} = \frac{1}{\pi}, \ \frac{\partial \mathrm{n}}{\partial \mathrm{k}} = \frac{1}{v\hbar} \tag{3.3}$$

The equation 3.3 is one-dimension, since the group velocity is defined as $\upsilon = \frac{1}{\hbar} \frac{\partial \mathrm{k}}{\partial \mathrm{E}}$, where a factor of two for spin is added, the equation cab be written as:

$$\delta I = \frac{2e}{h} (\mu_L - \mu_R) = \frac{2e^2}{h} \delta V \tag{3.4}$$

Here, δV denotes voltage which corresponds to the potential chemical difference. It is noticeable from the equation 3.4, in the absence of a scattering region, the conductance of one open channel is $\frac{2e^2}{h}$, and this around $77\ \mu S$, where the resistance is $\frac{h}{e^2}$, this approximately

12.9 $k\Omega$. When the scattering region is assumed in the system, the current is partially reflected with a probability $R = |\vec{r}|^2$ and partially transmitted with a probability $T = \left|\vec{t}\right|^2$. The current that will travel to the scatterer to the right side of the lead is:

$$\delta \mathrm{I} = \frac{2e^2}{h}\, T\delta V \rightarrow \frac{\delta I}{\delta V} = \frac{2e^2}{h}\, T \qquad (3.5)$$

The equation 3.5 is the Landauer formula where conductance is $G = \left(\frac{2e^2}{h}\right) T$. And the transmission coefficient is predicted at the Fermi energy [5]. Then, Buttiker, in 1985, has generalized the Landauer formula to more than one open channel [3]. Here the transmission coefficient can be replaced by the sum of all the transmission amplitudes representing the electrons going from the left contact and reaching to the right contact.

The equation 3.5 of Landauer formula for many open channels becomes:

$$\frac{\delta \mathrm{I}}{\delta V} = G = \frac{2e^2}{h} \sum\nolimits_{i,j} |t_{i,j}|^2 = \frac{2e^2}{h} Trace(tt^{\dagger}) \qquad (3.6)$$

Where $t_{i,j}$ denotes the amplitude of transmission representing scattering from the j^{th} channel of the left lead to i^{th} channel of the right lead, G is the electrical conductance and $r_{i,j}$ is the reflection amplitudes which describe how the electron travels through scattering region in the opposite direction. The scattering S matrix involving the electron coming from the left lead and the right lead can be described by combining the transmission and reflection amplitudes as follows:

$$S = \begin{pmatrix} r & \mathrm{t}' \\ t & \mathrm{r}' \end{pmatrix} \qquad (3.7)$$

Where, r and t describe the electrons coming from the left, while r' and t' represent electrons coming from the right. In the equation 3.8 r,t, $\mathrm{r}'$and t' are consider as complex matrices that for more than one open channel and because of the conservation satisfy $SS^{+}=I$.

3.3 Thermoelectric Coefficients

The Seebeck, Peltier, and Thompson effects at the turn of the nineteenth century formed the links between heat, current, temperature, and voltage [1]. The Seebeck effect describes the generation of electrical current due to a temperature difference, while the Thompson and Peltier effects explain the cooling or heating of a current-carrying conductor [6]. A more general mechanism can be considered in which the temperature differential is $\Delta\mathcal{T}$, and there is a theoretical drop ΔV in the system, causing the flow of both heat currents and charge. The generalized Landauer-Büttiker formulae will be shown for heat (Q) and charge (I) and currents within the linear basis and temperature regime to establish expressions for the thermoelectric coefficients of a device having two terminals. The system is comprised of a scattering region that has connections to two leads, which are themselves connected to a pair of electron reservoirs. These reservoirs are constructed using the chemical potential μ_L and μ_R, temperature $\mathcal{T}_L$ and$\mathcal{T}_R$, and the Fermi distribution function [6]:

$$f_i\,(E) = \left(1 + e^{\frac{E-\mu_i}{k_B\mathcal{T}_i}}\right)^{-1} \tag{3.8}$$

Assuming that the reservoirs and leads are connected so that scattering does not occur at their interface, this can be claimed that the central scattering area is the cause of all scattering effects. The right moving charge current of an individual k-state emerging from the left reservoir can be expressed in terms of the number of electrons per unit length$n$, the Fermi distribution f_L, the group velocity v_g, and the transmission coefficient $T(E)$ of the scattering zone (E).

$$I_k^+ = nev_g(E(k))\, T\big(E(k)\big)\; f_L(E(k)) \tag{3.9}$$

Thus, the total charge current can be determined from the right moving states by summing all positive k states, then converting the result into the integral form, where $n = 1/L$ for the electron density and $v_g = \frac{1}{\hbar}\frac{\partial E(k)}{\partial k}$.

$$I_k^+ = \sum_k e\,\frac{1}{L}\frac{1}{\hbar}\frac{\partial E(k)}{\partial k}\,T(E(k))\,f_L(E(k)) = \int_{-\infty}^{+\infty}\frac{2e}{h}\,T(E)\,f_L(E)\,dE \tag{3.10}$$

Similarly, we obtain the following for the left moving states:

$$I_k^- = \int_{-\infty}^{+\infty}\frac{2e}{h}\,T(E)\,f_R(E)\,dE \tag{3.11}$$

Thus, the total right-moving current can be represented as:

$$I = I^+ - I^- = \frac{2e}{h}\int_{-\infty}^{+\infty} T(E)\,(f_L(E) - f_R(E))\,dE \tag{3.12}$$

The equation 3.12 is denoted by the Landauer-Bttiker formula.

An equivalent derivation can be provided for the identical system's heat current (alternatively, energy current) by starting with the relation $\mathcal{Q} = Env_g$ rather than $= nev_g$. The final result is close to the previous results, but it involves two additional energy terms:

$$\mathcal{Q} = \mathcal{Q}^+ - \mathcal{Q}^- = \frac{2}{h}\int_{-\infty}^{+\infty} T(E)\left((E-\mu_L)f_L(E) - (E-\mu_R)f_R(E)\right)dE$$

Where,

$$f_L(E) = \left[1 + e^{\frac{E-\mu-\frac{\Delta\mu}{2}}{k_B\left(\mathcal{T}+\frac{\Delta\mathcal{T}}{2}\right)}}\right]^{-1},\ f_L(E) = \left[1 + e^{\frac{E-\mu-\frac{\Delta\mu}{2}}{k_B\left(\mathcal{T}+\frac{\Delta\mathcal{T}}{2}\right)}}\right]^{-1},$$

$$\mu_L = \mu + \frac{\Delta\mu}{2}, \qquad \mu_R = \mu - \frac{\Delta\mu}{2}$$

Buttiker, Imry, Landauer, et al. [7-10], relate the electric current I and heat current (Q) flowing through a system to the voltage difference ΔV and temperature difference $\Delta\mathcal{T}$ in the linear-response regime. As a result, the thermoelectric coefficients G, L, M, and K are related to both currents and temperature and potential differences [1 and 11-12]:

$$\begin{pmatrix} I \\ \dot{Q} \end{pmatrix} = \begin{pmatrix} G & L \\ M & K \end{pmatrix}\begin{pmatrix} \Delta V \\ \Delta\mathcal{T} \end{pmatrix} \qquad (3.13)$$

In the absence of a magnetic field, the thermoelectric coefficients L and M are related by the Onsager relation:

$$M = -L\mathcal{T} \qquad (3.14)$$

In the equation 3.14, $\mathcal{T}$ denotes temperature. In the rearranging of these equations, the measurable thermoelectric coefficients, electrical resistance$R = 1/G$, thermopower $S = -\Delta V/\Delta\mathcal{T}$, Peltier coefficient, and the thermal constant k can be used to express the current relations:

$$\begin{pmatrix}\Delta V\\ \dot{Q}\end{pmatrix} = \begin{pmatrix}\frac{1}{G} & -\frac{L}{G}\\ \frac{M}{G} & K - \frac{LM}{G}\end{pmatrix}\begin{pmatrix}1\\ \Delta\mathcal{T}\end{pmatrix} = \begin{pmatrix}R & S\\ \Pi & -K\end{pmatrix}\begin{pmatrix}1\\ \Delta\mathcal{T}\end{pmatrix} \tag{3.15}$$

In the absence of an electrical current, the thermopower S is described as the potential decrease due to a temperature difference:

$$S = -\begin{pmatrix}\Delta V\\ \Delta\mathcal{T}\end{pmatrix}_{I=0} = \frac{L}{G'} \tag{3.16}$$

In the absence of a temperature differential, the Peltier coefficient Π is described as the heat transferred solely due to the charge current:

$$\Pi = \left(\frac{\dot{Q}}{I}\right)_{\Delta\mathcal{T}=0} = \frac{M}{G} = -S\mathcal{T} \tag{3.17}$$

Eventually, in the absence of an electric current, thermal conductance k is described as the heat current due to temperature drop:

$$k = -\begin{pmatrix}\dot{Q}\\ \Delta\mathcal{T}\end{pmatrix}_{I=0} = -\left(1 + \frac{S^2 G\mathcal{T}}{k}\right) \tag{3.18}$$

Consequently, evaluating S or Π provides insight into the system's ability to perform as a heat-driven current generator or a current-driven cooling device.

Furthermore, the thermoelectric figure of merit, $Z\mathcal{T}$ [13, 14], can be described in terms of these measurable thermoelectric coefficients:

$$Z\mathcal{T} = \frac{S^2 G\mathcal{T}}{k} \tag{3.19}$$

The $Z\mathcal{T}$ is determined in classical electronics by calculating the maximum induced temperature difference caused by an applied electrical current in the presence of Joule heating. By considering a current-carrying conductor is placed between two heat baths $\mathcal{T}_L$ and $\mathcal{T}_R$, and electrical potentials V_L and V_R, respectively.

The thermoelectric figure of merit can be calculated by determining the conductor's maximum induced temperature difference caused by an electrical current. By defining ($\dot{Q}$) as the gain in heat from bath L to R, then from equation (3.13) we obtain:

$$\dot{Q} = \Pi\, I - k\Delta\mathcal{T} \tag{3.20}$$

This heat transfer results in the left bath cooling and the right bath heating, causing $\Delta\mathcal{T}$ increases. The sum of Joule heating can be calculated using the formula $\dot{Q}_J = RI^2$, which is proportional to both the electrical resistance and the current square. This Joule heating also affects the temperature difference generated by heat transfer, and therefore in the steady state case:

$$\Pi\, I - k\Delta T = \frac{R\, I^2}{2} \tag{3.21}$$

Where $R/2$ denotes the sum of two parallel resistances (internal and external resistance).

The temperature difference becomes:

$$\Delta\mathcal{T} = \frac{1}{k}\left(\Pi\, I - \frac{R\, I^2}{2}\right) \tag{3.22}$$

The equation 3.15 represents the relationship between temperature difference and current. The derivative of the equation 3.16 can determine the maximum $\Delta\mathcal{T}$:

$$\frac{\partial\Delta\mathcal{T}}{\partial I} = \frac{\Pi - IR}{k} = 0 \tag{3.23}$$

To obtain the maximum $\Delta\mathcal{T}$, we insert $I = \Pi\,/R$ and substituting the equation 3.17 into the equation 3.23.

$$(\Delta\mathcal{T})_{max} = \frac{\Pi^2}{2kR} = \frac{S^2\mathcal{T}^2G}{2k} \tag{3.24}$$

$$\frac{(\Delta\mathcal{T})_{max}}{\mathcal{T}} = \frac{S^2\mathcal{T}^2G\mathcal{T}}{2k} = \frac{1}{2}Z \tag{3.25}$$

Giving a dimensionless number that can be used to describe a molecular device's 'efficiency'.

3.3 Theory of electron transport

To investigate electron transport, it is important to understand the transmission probability, which is related to the conductance G at the Fermi energy E by the Landauer formula [15, 16].

$$G = G_0 T(E) \qquad (3.26)$$

The equation 3.26 shows the electric conductance G as a function of energy and the quantum conductance is described by $G_0 = \frac{2e^2}{h}$ where e represents the electron charge and h is the Planck's constant. Also, $T(E)$ is the transmission coefficient as a function of energy, and it can be defined as the probability that an electron with energy E can transfer from one electrode to the other. This refers to the scattering formalism seen in the schematic below

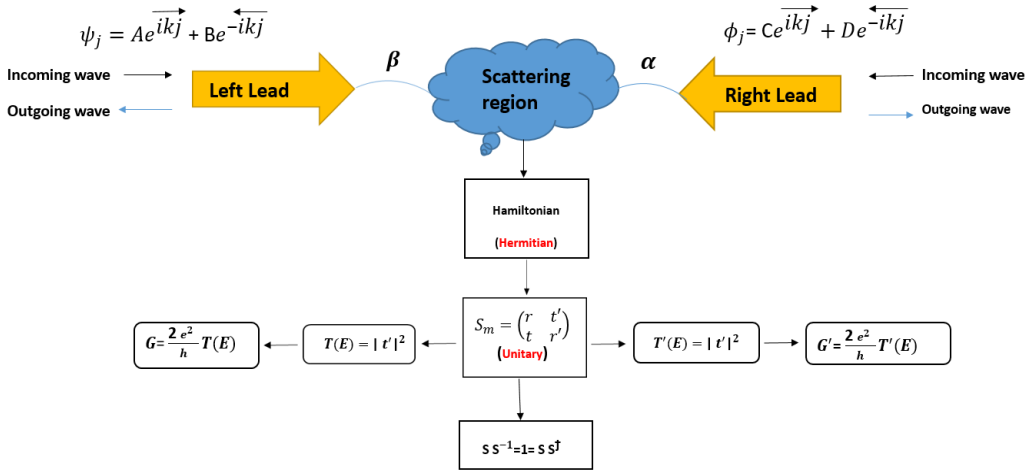

Figure 3.2: Representation of the transport mechanism. It shows combination of mathematical and physical structure. This mechanism contains two types of probabilities as of R and T.

$$\left|\vec{t}\right|^2 + |\vec{r}|^2 = 1 \qquad T + R = 1$$

3.4 Scattering Theory

3.4.1 One dimensional (1-D) linear crystalline lattice

It helps calculate the scattering matrix for a simple one-dimensional structure to provide a simple and straightforward outline of the methodology used before representing a generalized methodology, [1]. In this calculation, Green's function is utilized for derivation. Moreover, a simple tight-binding model in periodic systems is considered to provide a qualitative view of electronic systems' calculations. Each atom contains a single atomic orbital of energy and is the first nearest neighbour coupling or hopping element, as shown in the Figure 3.3**.**

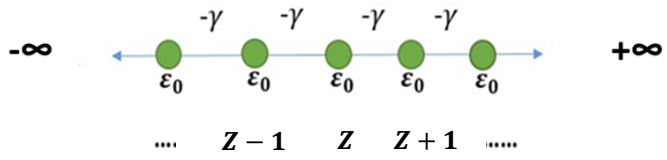

Figure 3.3: Representation of a tight-binding model of a (1-D) periodic lattice with energy site and hopping elements is the label of our atoms.

The system is described by the Hamiltonian H, which is

$$H = \begin{pmatrix} -\infty & . & . & . & . & . & . & . & . \\ . & . & . & . & . & . & . & . & . \\ . & . & \varepsilon_0 & -\gamma & 0 & 0 & 0 & . & . \\ . & . & -\gamma & \varepsilon_0 & -\gamma & 0 & 0 & . & . \\ . & . & 0 & -\gamma & \varepsilon_0 & -\gamma & 0 & . & . \\ . & . & 0 & 0 & -\gamma & \varepsilon_0 & -\gamma & . & . \\ . & . & 0 & 0 & 0 & -\gamma & \varepsilon_0 & . & . \\ . & . & . & . & . & 0 & -\gamma & . & . \\ . & . & . & . & . & . & . & . & +\infty \end{pmatrix}$$

Then, the Schrodinger equation is used to obtain Z row of the Hamiltonian:

$$\varepsilon_0\,\psi_Z - \gamma\psi_{Z+1} - \gamma\,\psi_{Z-1} = E\,\psi_Z \qquad (3.27)$$

$$\psi_Z = e^{ikZ} \qquad (3.28)$$

Where, ψ_Z is a wave function of this system, this only needs to satisfy criteria of the Schrodinger equation 3.28.

By substituting a plane wave the equation 3.28 into the equation 3.27 leads to the dispersion relation in the equation 3.30**.** Where we assume γ= γ*.

$$E = \varepsilon_0 - 2\gamma\cos(\mathrm{k}) \qquad (3.29)$$

Here, the wave number is described by the quantum number (k), while the wave function is related to the retarded Greens function defined as $\mathrm{g}(\mathrm{z},\mathrm{z}')$. The method solves the same equation, as the Schrödinger equation.

$$\left.\begin{array}{c}(E-H)\,g(z,z') = \delta_{(z,z')} \\ -\gamma g(z-1,z') + (E-\varepsilon_0)\,g(z,z') - \gamma\,g(z+1,z') = \delta_{(z,z')}\end{array}\right\} \qquad (3.30)$$

Where $\delta_{(z,z')} = 1$, if $z = z'$, And $\delta_{(z,z')} = 0$, if $z \neq z'$.

The amplitude at the point z is consider to be the Green's function g (z,z') of a system , caused by an excitation at point z'. Two waves would be produced due to this excitation, and travel through the points of the excitation. The Figure 3.3 shows the amplitudes B and D.

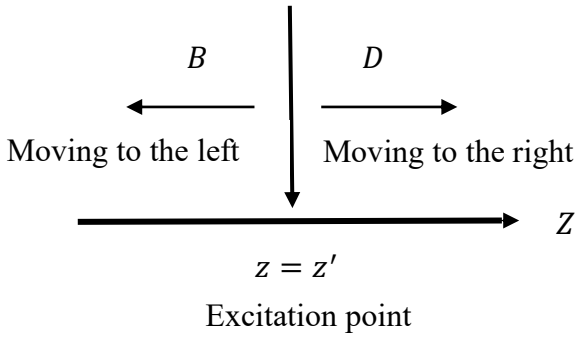

Figure 3.3: Representation of retarded Green's function. This contains an infinite one-dimensional lattice. Through excitation point at z=z', the wave is propagated towards the left and right sides. These waves have amplitude B and D respectively.

Figure 3.3 shows the two waves moves outward from the excitation point with their amplitudes B and D . Consequently, the two waves can be written as:

$$g(z, z') = \begin{cases} D\, e^{ikz}, & z \geq z' \\ B\, e^{-ikz}, & z \leq z' \end{cases} \qquad (3.31)$$

The fact that the equation 3.31 satisfy the equation 3.30 at every point. However, the conditions at point $z = z'$ is not satisfied where the Green's function must be continuous at this point ($z = z'$).

$$[g(z,z')\,]_{Left} = [g(z,z')]_{Right} \tag{3.32}$$

$$B\,e^{-ikz'} = D\,e^{ikz'} \tag{3.33}$$

$$B = e^{2ikz'} \tag{3.34}$$

Now, we obtain the following:

$$g(z,z') \tag{3.35}$$
$$= \begin{cases} D\,e^{ikz} = D\,e^{ikz'}e^{ik(z-z')} & z \geq z' \\ D\,e^{2ikz'}D\,e^{2ikz'} = D\,e^{ikz'}e^{ik(z'-z)} = D\,e^{ikz'}e^{ik(z'-z)} & z \geq z' \end{cases}$$

We can see that the power of the complex exponent is always positive, thus the simplified form can be described as:

$$g(z,z') = D\,e^{ikz'}e^{ik\,|z'-z|} \tag{3.36}$$

In addition, this equation must fulfil the Green's function, $(E-H)g(z-z') = \delta_{(z,z')}$:

$$\delta_{z,z'} = Eg(z,z') - \varepsilon_0 g(z-z') + \gamma g(z+1,z') + \gamma g(z-1,z') \tag{3.37}$$

Thus, we obtain the solution at $z = z'$ to be:

$$1 = (E - \varepsilon_0)g(z,z) + \gamma g(z+1,z') + \gamma g(z-1,z') \qquad (3.38)$$

$$= D\, e^{ikz'}[(E - \varepsilon_0)]e^{ik\,|z-z|} + \gamma e^{ik\,|z+1\,z|} + \gamma e^{ik\,|z-1\,z|}$$

When we solve it for $D\, e^{ikz'}$. we get:

$$\frac{1}{D\, e^{ikz'}} = (E - \varepsilon_0) + \gamma e^{ik} + \gamma e^{ik}$$

$$= (E - \varepsilon_0) + \gamma e^{ik} + \gamma e^{ik} + \gamma e^{-ik} + \gamma e^{-ik}$$

$$= \gamma e^{ik} - \gamma e^{-ik}$$

$$De^{ikz'} = \frac{1}{2i\gamma \sin(k)} \qquad (3.39)$$

Starting from the group velocity $hv_g = 2\gamma \sin(k)$, we can express the Green's function for a one-dimensional chain as:

$$g^R(z,z') = \frac{1}{ihv_g} e^{ik\,|z-z'|} \qquad (3.40)$$

Here, several solutions of this problem are reported in the literature [4, 17- 19]. In the equation above, we solved this problem using the retarded Green's function $g^R(z,z')$. Nevertheless, the advanced Green's function $g^A(z,z')$ is an equally true solution;

$$g^A(z,z') = \frac{-1}{i\hbar v_g} e^{ik\,|z-z'|} = \frac{-i}{\hbar v_g} e^{ik\,|z-z'|} \qquad (3.41)$$

We can say that, Outgoing waves from an excitation point (z=z ') are represented by the retarded Green function, however two incoming waves that vanish at the excitation point is represented by the advanced Greens' function. Thus, the retarded Green's function will be used for the simplicity. We Then delete the R from the expression to be as $(z - z') = g^R(z, z')$,[1].

3.4.2 Semi-infinite one-dimensional lattice

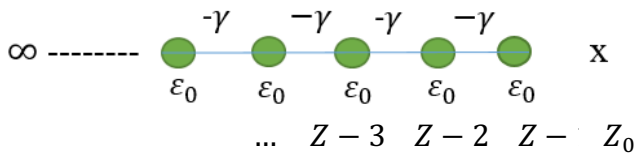

Figure 3.4: Representation of tight-binding model of a semi-infinite one-dimensional lattice. This system contains of energy site ε_0 and hopping elements (γ).

First, we aim to satisfy the boundary condition (B.C). This will be done by introducing another plane wave component with a new amplitude [1]:

$$g(z, z') = \frac{1}{ihv_g} e^{ik\,|z-z'|} + Ae^{-ik\,|z-z'|} \qquad (3.42)$$

By using the condition $(z, z_0) = 0$, $z \leq z'$, we obtain:

$$g(z, z_0) = \frac{1}{ihv_g} e^{ik\,(z_0-z)} + Ae^{-ik(z_0-z)}$$

$$A = \frac{1}{ihv_g} e^{2ik\,(z_0 - z)} \tag{3.43}$$

Now, we substituting this back into the Green's function to find:

$$g(z, z') = \frac{1}{ihv_g} e^{ik\,(z' - z)} - \frac{1}{ihv_g} e^{2ik\,(z - z_0)} e^{-ik\,(z' - z)}$$

$$g(z, z') = \frac{1}{ihv_g} [e^{ik\,(z' - z)} - e^{ik\,(2z_0 - z - z')}] \tag{3.44}$$

Then, we apply the second condition which is any any point beyond $(z_0 - 1)$ does not have effect from a source in the chain. Thus, it is expected that $g(z_0, z) = 0$ if if $z \geq z'$ and $z = z_0$. According to this condition, we find:

$$g(z_0, z) = \frac{1}{ihv_g} e^{ik\,(z_0 - z')} - Ae^{-ik\,(z_0 - z')}$$

$$A = -\frac{1}{ihv_g} e^{2ik\,(z_0 - z')} \tag{3.45}$$

When we substituting this back into the Green's function, we obtain:

$$g(z, z') = \frac{1}{ihv_g} e^{ik\,(z - z')} - \frac{1}{ihv_g} e^{2ik\,(z_0 - z')}\, e^{-ik\,(z - z')}$$

$$g(z, z') = \frac{1}{ihv_g} \left[e^{ik\,(z - z')} - e^{ik\,(2z_0 - z - z')}\right] \tag{3.46}$$

In order to summarize these two equations, we write the following:

$$\begin{cases} \frac{1}{ihv_g}\left[e^{ik\,(z-z')} - e^{ik\,(2z_0-z-z')}\right], z \geq z' \\ \frac{1}{ihv_g}\left[e^{ik\,(z'-z)} - e^{ik\,(2z_0-z-z')}\right], z \leq z' \end{cases} \tag{3.47}$$

Moreover, the above equation can be expressed as

$$g(z,z') = \frac{1}{ihv_g}\left[e^{ik\,|z-z'|} - e^{ik\,(2z_0-z-z')}\right] = g^{\infty}_{z,z'} + \Psi^{z_0}_{z,z'} \tag{3.48}$$

3.4.3 One dimensional (1-D) scattering

In this section, we will give a simple example, the surface Green's function is calculated with the site$z = z_0 - 1$. So, the surface Green's function can be expressed as the following [1]:

$$g(z_0 - 1, z_0 - 1\,) = \frac{1}{ihv_g}\left[e^{ik\,|z_0-1,z_0-1|} - e^{ik\,(2z_0-z_0+1-z_{0+1})}\right] \tag{3.49}$$

Now, we simplified this form to get:

$$g(z_0 - 1, z_0 - 1\,) = \frac{1}{ihv_g} - 2i\sin(k)\,e^{ik} \tag{3.50}$$

$$g(z_0 - 1, z_0 - 1\,) = \frac{2i\,\sin\,(k)}{2i\,\gamma\,\sin\,(k)}e^{ik} = -\frac{e^{ik}}{\gamma} \tag{3.51}$$

3.4.4 One-dimensional (1-D) Scattering Using Green's functions

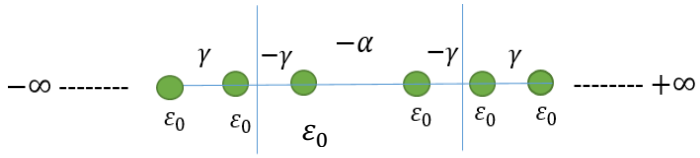

Figure 3.5: Representation of tight binding model of two semi-infinite leads with one site energies ε_0 and couplings –γ, coupled by hopping element –α.

Here in this example, we two semi-infinite one-dimensional leads both leads are equal with ε_0 on-site potential and –γ hopping elements. In the case of decoupled leads ($\alpha = 0$) , the total Green function is obtained and it is described by [1];

$$g = \begin{pmatrix} \frac{e^{ik}}{\gamma} & 0 \\ 0 & -\frac{e^{ik}}{\gamma} \end{pmatrix} \tag{3.52}$$

Since we have the two decoupled semi-infinite leads, the Green's function is written as $g = (E - h_1)^{-1}$ where h_1 is the Hamiltonian of two decoupled semi-infinite leads. Thus, we have created an infinite matrix for determining this Hamiltonian h_1 as:

$$h_1 = \begin{pmatrix} . & . & 0 & 0 & 0 \\ . & \varepsilon_0 & -\gamma & 0 & 0 \\ 0 & -\gamma & \varepsilon_0 & -\gamma & 0 \\ 0 & 0 & -\gamma & \varepsilon_0 & -\gamma \\ 0 & 0 & 0 & 0 & . \end{pmatrix} \tag{3.53}$$

By connecting the two leads by a hopping element, the Hamiltonian for whole system is $H = h_1 + h_0$ where h_0 represents the coupling parameters

$$h_0 = \begin{pmatrix} 0 & \alpha \\ \alpha & 0 \end{pmatrix} \tag{3.54}$$

Now we use Dyson's equation to obtain The Green's function for coupled system:

$$G = (E - H)^{-1} = (E - h_1 - h_0)^{-1} \tag{3.55}$$

$$G = (g^{-1} - h_0)^{-1} \tag{3.56}$$

The solution would be as follows:

$$G = \left(\begin{pmatrix} -\frac{e^{ik}}{\gamma} & 0 \\ 0 & -\frac{e^{ik}}{\gamma} \end{pmatrix}^{-1} - \begin{pmatrix} 0 & \alpha \\ \alpha & 0 \end{pmatrix} \right)^{-1} \tag{3.57}$$

$$G = \frac{1}{\gamma^2 e^{-2ik} - \alpha} \begin{pmatrix} -\gamma e^{-ik} & \alpha \\ \alpha^* & -\gamma e^{-ik} \end{pmatrix} \tag{3.58}$$

Now, we calculate the Greens' function described in the equation (3.58) and apply them to the Fisher Lee relation to calculate transmission $\vec{t}$ and reflection $\overleftarrow{r}$ amplitudes. Fisher Lee relation

determines the scattering amplitudes of the scattering problem by relating it to the Green's function of the same problem.

By determining the Green's function components from equation (3.58), transmission and reflection coefficients can be defined. When we send two waves moving outwards starting from source (the excitation point), one away from the scatter and one towards the scatter with amplitude B and D respectively. Consequently, the Green's function represents two waves: a left wave or a reflected wave ($De^{-\mathrm{ik}|\mathrm{z}-\mathrm{z}'|} + Bre^{\mathrm{ik}|\mathrm{z}-\mathrm{z}'|}$) and a right wave or a transmitted wave ($Bre^{\mathrm{ik}|\mathrm{z}-\mathrm{z}'|}$). Here we use $\overleftarrow{t}$ to describe transmitted right wave and $\overleftarrow{r}$ to represent reflected left wave where arrows are pointing directions of amplitudes.

$$1 + r = -ihv_g \frac{\gamma\, e^{-ik}}{\gamma^2 e^{-2ik} - \alpha^2} \tag{3.59}$$

$$t = ihv_g \frac{\alpha\, e^{ik}}{\gamma^2 e^{-2ik} - \alpha^2} \tag{3.60}$$

Now, we calculate the transmission and reflection probabilities as the following:

$T = |\mathrm{t}|^2$ and $T = |\mathrm{r}|^2$

Finally, the conductance of the system can be calculated by using the Landauer formula

$G = G_0 T(E)$.

3.5 Bibliography

1. Lambert, C. J. (2021). Quantum Transport in Nanostructures and Molecules.

2. Landauer, R. (1957). Spatial variation of currents and fields due to localized scatterers in metallic conduction. *IBM Journal of research and development*, *1*(3), 223-231.
3. Büttiker, M., Imry, Y., Landauer, R., and Pinhas, S. (1985). Generalized many-channel conductance formula with application to small rings. *Physical Review B*, *31*(10), 6207.
4. Datta, S. (1997). *Electronic transport in mesoscopic systems*. Cambridge university press.
5. Cuevas, J. C., Scheer, E., Cao, G., Wang, Y., Tsukerman, I., Tenne, R., and Ghaemmaghami, A. (2010). World Scientific series in nanoscience and nanotechnology. *Molecular electronics: an introduction to theory and experiment*, *1*.
6. Finch, C. M. (2008). *An understanding of the the electrical characteristics of organic molecular devices* (Doctoral dissertation, Lancaster University).
7. Büttiker, M., Imry, Y., Landauer, R., and Pinhas, S. (1985). Generalized many-channel conductance formula with application to small rings. *Physical Review B*, *31*(10), 6207.
8. Maslyuk, V. V., Achilles, S., and Mertig, I. (2010). Spin-polarized transport and thermopower of organometallic nanocontacts. *Solid State Communications*, *150*(11-12), 505-509.
9. García-Suárez, V. M., Ferradás, R., and Ferrer, J. (2013). Impact of Fano and Breit-Wigner resonances in the thermoelectric properties of nanoscale junctions. *Physical review b*, *88*(23), 235417.
10. Claughton, N. R., and Lambert, C. J. (1996). Thermoelectric properties of mesoscopic superconductors. *Physical review b*, *53*(10), 6605.
11. Sivan, U., and Imry, Y. (1986). Multichannel Landauer formula for thermoelectric transport with application to thermopower near the mobility edge. *Physical review b*, *33*(1), 551.

12. Hicks, L. D., and Dresselhaus, M. S. (1993). Effect of quantum-well structures on the thermoelectric figure of merit. *Physical Review B*, *47*(19), 12727.
13. Goldsmid, H. J. (1964). Thermoelectric Refrigeration Plenum. *New York*.
14. Athanasopoulos, S. (2005). *Electronic properties of hybrid carbon nanotubes* (Doctoral dissertation, Lancaster University).
15. Feng, D., and Jin, G. (2005). *Introduction to Condensed Matter Physics, Volume 1*. World Scientific Publishing Company.
16. Lesovik, G. Electronic Transport in Meso-and Nano-Scale Conductors.
17. Economou, E. N. (1983). Two or More Impurities; Disordered Systems. In *Green's Functions in Quantum Physics* (pp. 128-195). Springer, Berlin, Heidelberg.
18. Mello, P. A., Mello, P. A., Kumar, N., and Narendra Kumar, D. (2004). *Quantum transport in mesoscopic systems: complexity and statistical fluctuations: a maximum-entropy viewpoint* (Vol. 4). Oxford University Press on Demand.
19. Sanvito, S., Lambert, C. J., Jefferson, J. H., and Bratkovsky, A. M. (1999). General Green's-function formalism for transport calculations with spd Hamiltonians and giant magnetoresistance in Co-and Ni-based magnetic multilayers. *Physical review B*, *59*(18), 11936.

Chapter 4

Multi-Component Self-Assembled Molecular-Electronic Films - Towards New High-Performance Thermoelectric Systems.

This work was a collaboration between the group of Prof. Nicholas Long (Department of Chemistry, Imperial College London), who synthesised the anthracene molecules and Dr. Benjamin Robinson (Physics Department, Lancaster University), who conducted the experiments. Theoretical work was carried out at Lancaster as well. This work will be published soon in the name of Multi-Component Self-Assembly on a Surface - Towards New Thermoelectric Systems.

Troy L. R. Bennett, ***Majed Alshammari***, Ahmad Almutlg, Xintai Wang, Ali Ismael, Luke A. Wilkinson, Andrew J. P. White, Tim Albrecht, Samuel Jarvis, Lesley F. Cohen, Colin J. Lambert, Benjamin J. Robinson and Nicholas J. Long (**2021**). *Multi-Component Self-Assembly on a Surface - Towards New Thermoelectric Systems.*

4.1 Motivation

The thermoelectric properties of parallel arrays of organic molecules on a surface offer the potential for large-area, flexible, solution processed, energy harvesting thin-films, whose room-temperature transport properties are controlled by quantum interference (QI). Recently, it has been demonstrated that constructive QI (CQI) can be translated from single molecules to self-assembled monolayers (SAMs), boosting both electrical conductivities and Seebeck coefficients S. However, these CQI-enhanced systems are limited by rigid coupling of the component molecules to metallic electrodes, preventing the introduction of additional layers which would be advantageous for their further development. These rigid couplings also limit our ability to suppress the transport of phonons through these systems, which could act to boost their thermoelectric output, without comprising on their impressive electronic features. Here, through a combined experimental and theoretical study, we show that cross-plane thermoelectricity in SAMs can be enhanced by incorporating extra molecular layers. We utilize a bottom-up approach to assemble multi-component thin-films that combine a rigid, highly conductive 'sticky'-linker, formed from alkynyl-functionalised anthracenes, and a 'slippery'-linker consisting of a functionalized metalloporphyrin. Starting from an anthracene-based SAM, we demonstrate that subsequent addition of either a porphyrin layer or a graphene layer increases the Seebeck coefficient S, and addition of both porphyrin and graphene leads to a further boost in their Seebeck coefficients. This demonstration of Seebeck-enhanced multi-component SAMs is the first of its kind and presents a new strategy towards the design of thin-film thermoelectric materials.

4.2 Studied Molecules

Starting with the DFT code SIESTA [1], the isolated molecules' optimum geometries are achieved by relaxing the molecules. These relaxed molecules are obtained until all atoms' forces were less than 0.01 eV / Å [2-5]. A double-zeta plus polarization orbital basis set, norm-conserving pseudopotentials, and energy cut-off of 250 Rydbergs defining the real space grid were used and the Generalized Gradient Approximation (GGA) was chosen as the exchange-correlation functional [6-7]. Figure 4.1 illustrates the studied structures, where **1, 2** and **3** are **9,10** anthracene-based molecules with Py-SMe, pristine 2SMe and 2Py anchor groups respectively, while **4** is **1, 5** anthracene-based molecule with 2Py anchor group.

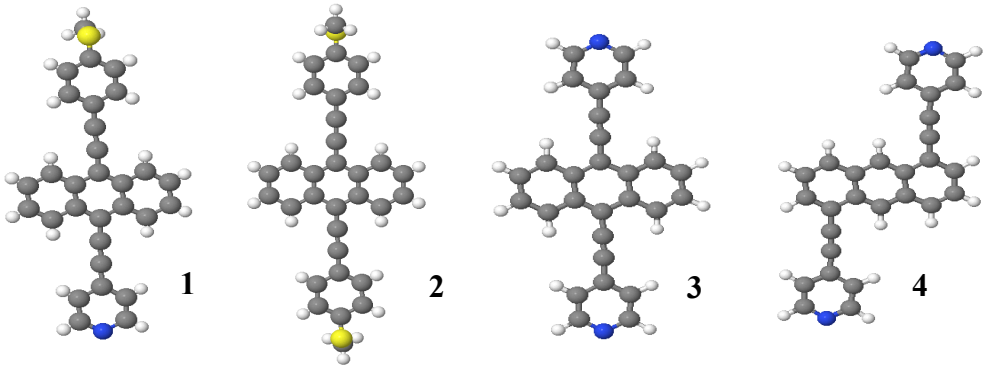

Figure 4.1. 1: 9, 10 Anthracene-based molecule with pyridyl and thioether anchor groups (Py-SMe), **2. 1, 9** Anthracene-based molecule with pristine thioether anchor group (2SMe), **3**: **9, 10** Anthracene-based molecule with pristine pyridyl anchor group (2Py), **4. 1, 5** Anthracene-based molecule with pristine pyridyl anchor group (2Py).

4.3 Frontier orbitals

To have a better understanding of the electronic properties of these structures (see Figure 4.1), the methods introduced in chapter 2 have been employed. Thus, I will investigate the wave functions of the four anthracene-based molecules

Figures 4.2-4.5, illustrate the frontier orbital for the studied molecules **1-4 (**see Figure 4.1)**.** Highest occupied molecular orbitals (HOMO), lowest unoccupied orbitals (LUMO), HOMO-1 and LUM+1 along with their energies are calculated. The red and blue colour correspond to the regions in space of positive and negative orbital amplitude. Quantum interference (QI) is expected to occur in this type of molecules (multipath). According to the product rule (PR), [8]. Figures 4.2-4.5 predict there is a constructive quantum interference (CQI), for the four molecules. Later on, I will check this prediction against the DFT results.

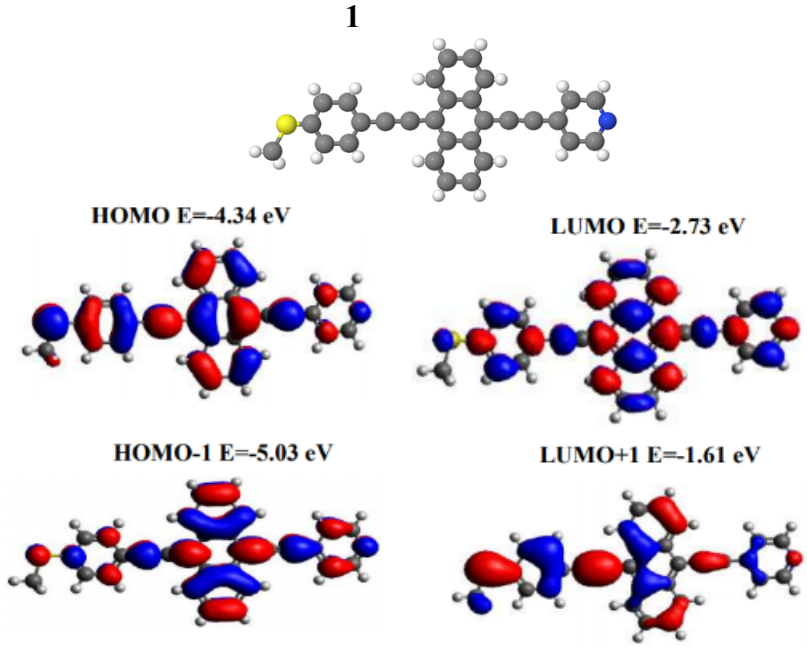

Figure 4.2: Wave function of **1**. **Top panel**: fully optimised geometry of **1. Lower panel**: HOMO, LUMO, HOMO-1, LUMO+1 of molecule **1** along with their energies.

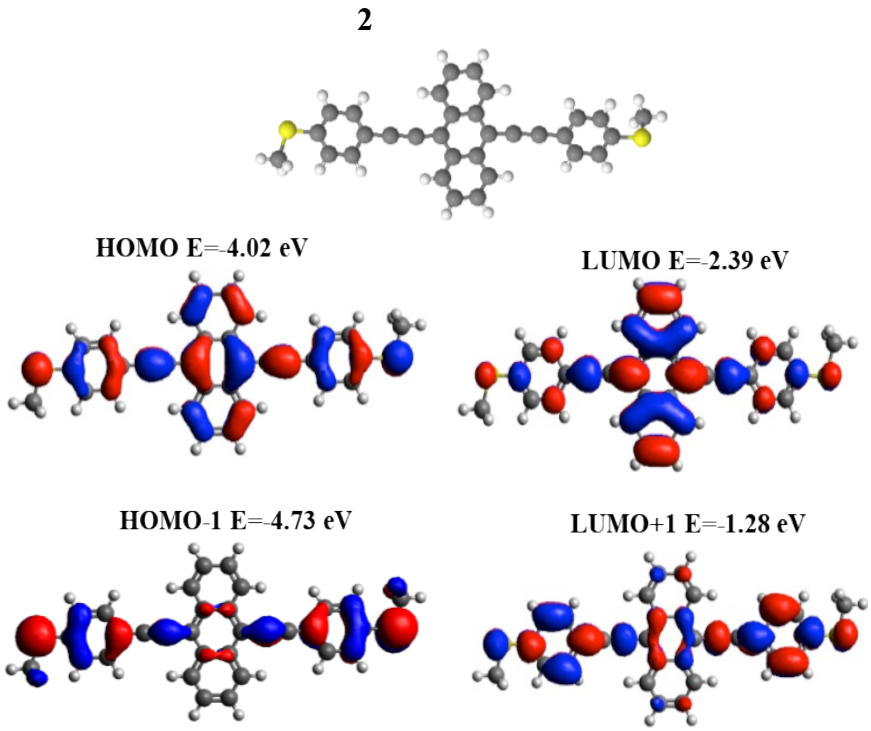

Figure 4.3: Wave function of **2**. **Top panel**: fully optimised geometry of **2**. **Lower panel**: HOMO, LUMO, HOMO-1, LUMO+1 of molecule **2** along with their energies.

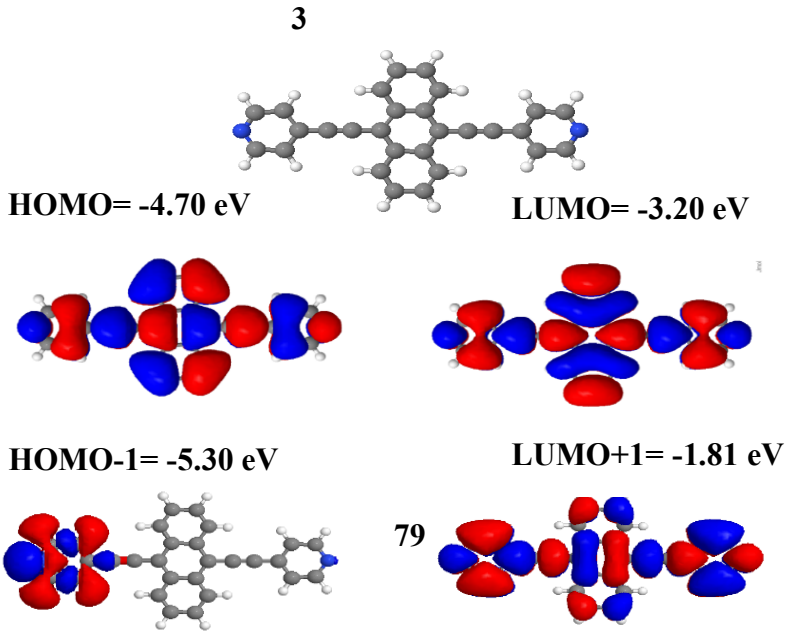

Figure 4.4: Wave function of **3**. **Top panel**: fully optimised geometry of **3**. **Lower panel**: HOMO, LUMO, HOMO-1, LUMO+1 of molecule **3** along with their energies.

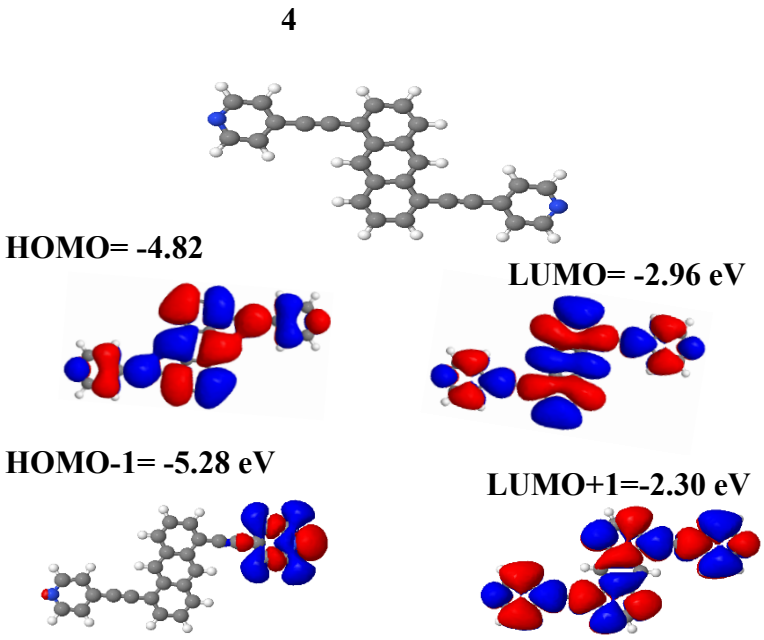

Figure 4.5: Wave function of **4**. **Top panel**: fully optimised geometry of **4**. **Lower panel**: HOMO, LUMO, HOMO-1, LUMO+1 of molecule **4** along with their energies.

I aim to combine these four anthracene-based molecules (see Figure 4.1) with porphyrin (Zn-TPP), graphene sheet (G), and both (Zn-TPP+ G), as shown in Figure 4.6. Thus, I consider three cases, case-1 bare anthracene-based molecules, case-2 anthracene-based molecules with Zn-TPP, and case-3 combine both Zn-TPP and G with the anthracene-based molecules. To do this, I start first by calculating the binding energy to know whether in real life the multicomponent prefers to combine or not? I will discuss that thoroughly, in the next section.

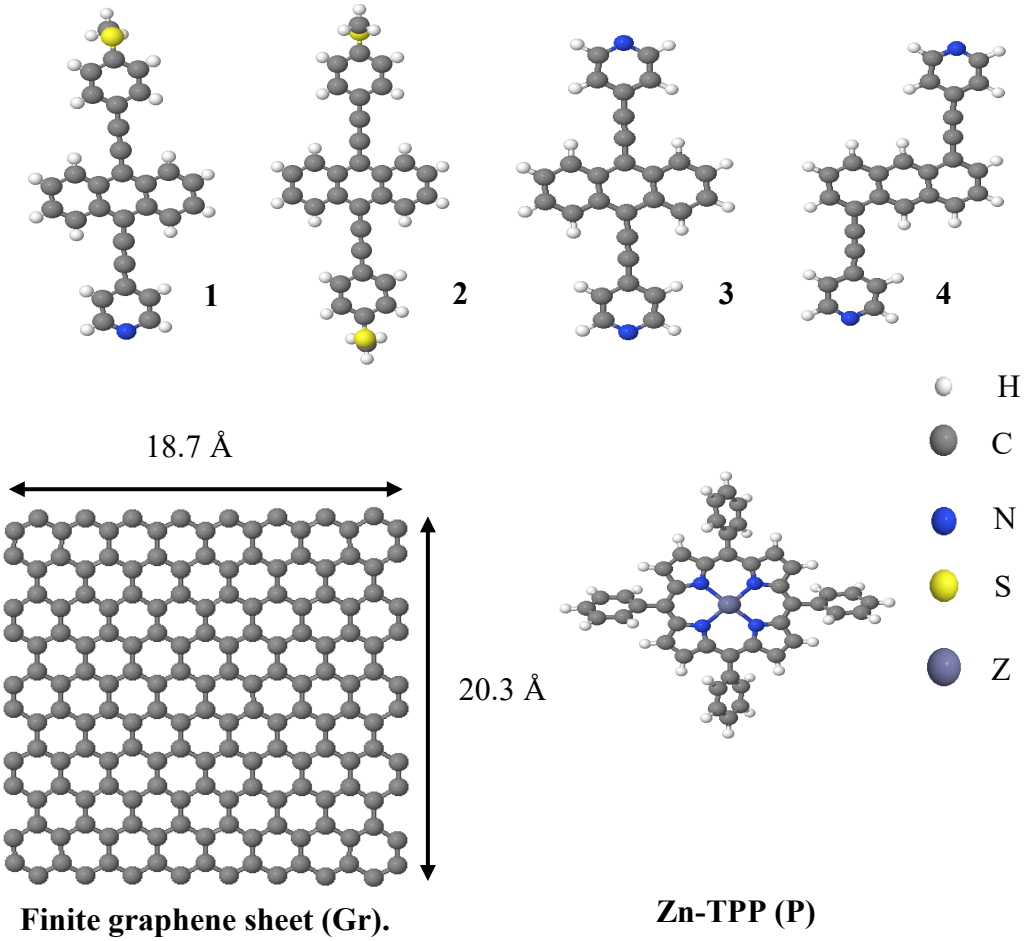

Figure 4.6: Top panel: 1: **9, 10** Anthracene-based molecule (Py-SMe), **2**: **9, 10** Anthracene-based molecule (2SMe), **3**: **9, 10** Anthracene-based molecule(2Py), **4: 1, 5** Anthracene-based molecule (2Py). **Lower panel:** Finite graphene sheet (Gr), porphyrin Zn-TPP (P), left to right.

4.4 Counterpoise method

The DFT method can be used to calculate the binding energy between different parts of a configuration. This is achieved by calculating the ground state energy of the whole and then the energy of the individual components. However, these calculations are subject to errors using a DFT code such as SIESTA, [1]. which uses localised basis sets that are focused on the nuclei. When atoms are close to each other, their basis functions will overlap, which leads to the strengthening of atomic interactions, and this could affect the total energy of the system. Generally, the Basis Set Superposition Error correction (BSSE) [9] or the counterpoise correction [10] helps to solve this type of error.

Let us consider two component systems which are labelled as A and B; the binding energy of the interaction can be defined as:

$$\Delta E(AB) = E_{AB}^{AB} - E_{A}^{A} - E_{B}^{B} \qquad 4.1$$

Where E_{AB}^{AB} is the total energy for the dimer system A and B, and the E_{A}^{A}, E_{B}^{B} is the total energy of the total isolated components. Here the superscript denotes the basis set used in each calculation i.e. A is just the basis set of system A, B is the basis set of B and AB is the combined basis set of both A and B.

To remove the numerical errors, the energy calculations are performed in the same total basis set AB. This is achieved in SIESTA by using 'ghost' states; (basis set functions which have no electrons or protons); to evaluate the total energy of the systems A and B in the dimer basis. This is formulated by the following equation,

$$\Delta E(AB) = E_{AB}^{AB} - E_{A}^{AB} - E_{B}^{AB} \qquad 4.2$$

Here the E_{A}^{AB}, E_{B}^{AB}, is both the energy of the system A and B evaluated based on the dimer. This method provides accurate and reliable results for different systems.

4.4.1 Binding energy of multicomponent

In this section, four binding energies are calculated to find the optimum distance between the components, **B1:** anthracene molecule and graphene sheet (Gr), **B2:** anthracene molecule and porphyrin molecule (Zn-TPP), **B3**: **B2** (anthracene+ Zn-TPP), and Gr. **B4:** anthracene (2SMe) and (Zn-TPP), as shown in Figures 4.7- 4.10.

In Figure 4.7, a graphene sheet (Gr) is attached to the anthracene, as shown in the right panel. The binding energy as a function of the optimum distances has been obtained. **B1** (Py-Gr) shows that a value of d = 3.0 Å gives the optimum distance between the anthracene and Gr, at approximately 0.15 eV. In Figure 4.8, **B2** (Py- ZnTPP) the anthracene molecule and (ZnTPP), the optimum distance is found to be d = 2.3 Å, at approximately 0.5 eV. After binding the optimum distance of **B2**, this new component is attached again to Gr sheet to be **B3**. The optimum distance of **B3** (Zn-Gr) is found to be 4.0 Å, and at approximately 0.15 eV, as shown in Figure 4.9.

B4; I repeat the same calculation however with different anchor group (more precisely thioether), to find whether this anchor binds to a porphyrin molecule through SMe-ZnTPP.

Figure 4.10 proves the SMe- ZnTPP to be the weakest bond among the four bonds (see **B1, B2, B3** and **B4**). No wonder, as the CH_3 group hinders the S atom from binding to Zn and the actual binding energy is 0.05 eV. This result suggests that SMe does not like to bind to ZnTPP.

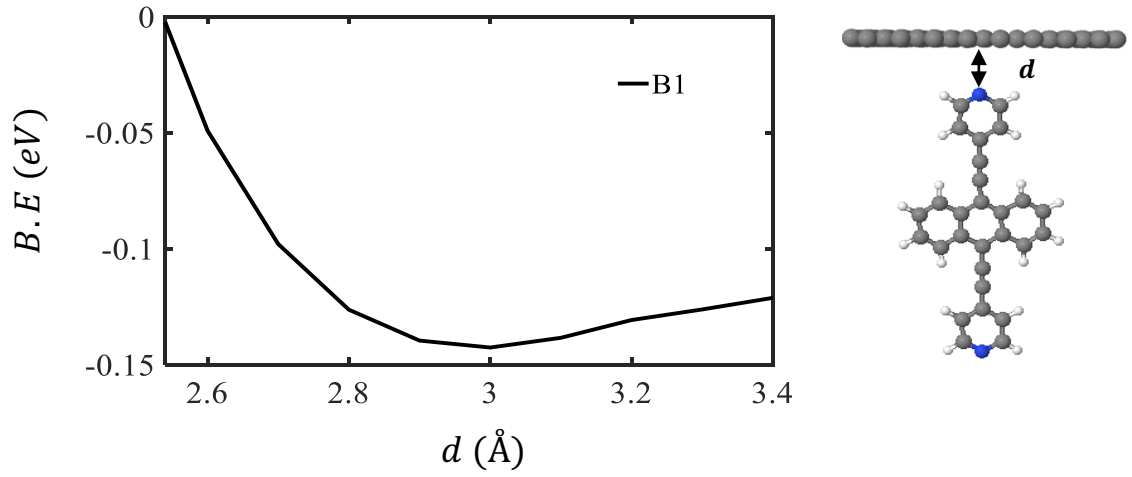

Figure 4.7: Right panel: Anthracene-based molecule with 2Py anchors and graphene sheet (Gr). **Left panel:** Binding energy versus distance plot of **B1** (Py-Gr), where the optimum distance d is found to be 3 Å, at approximately 0.15 eV.

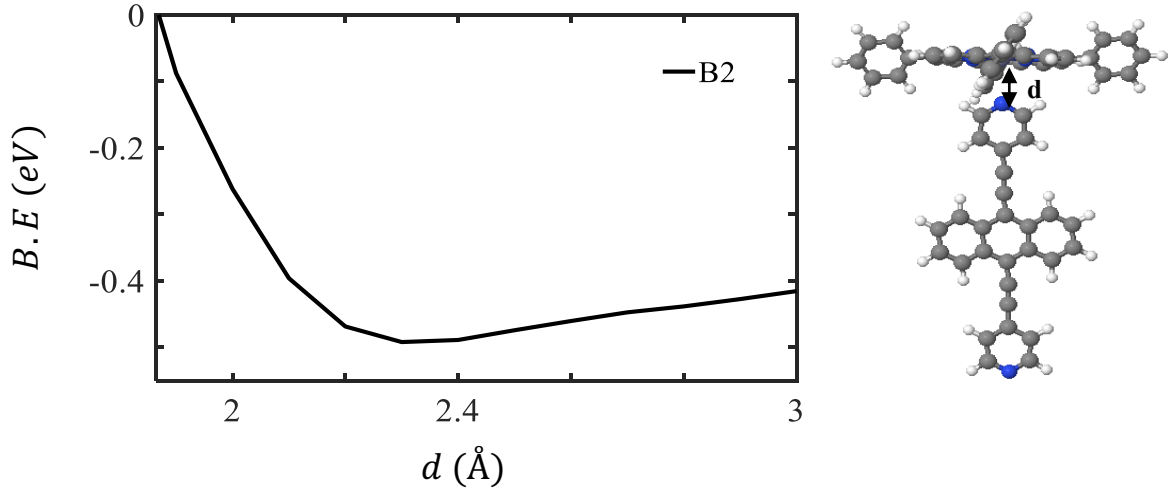

Figure 4.8: Right panel: Anthracene-based molecule with 2Py anchors and (Zn-TPP). **Left panel:** Binding energy versus distance plot of **B2** (Py-Zn-TTP), where the optimum distance d is found to be 2.3 Å, at approximately 0.50 eV.

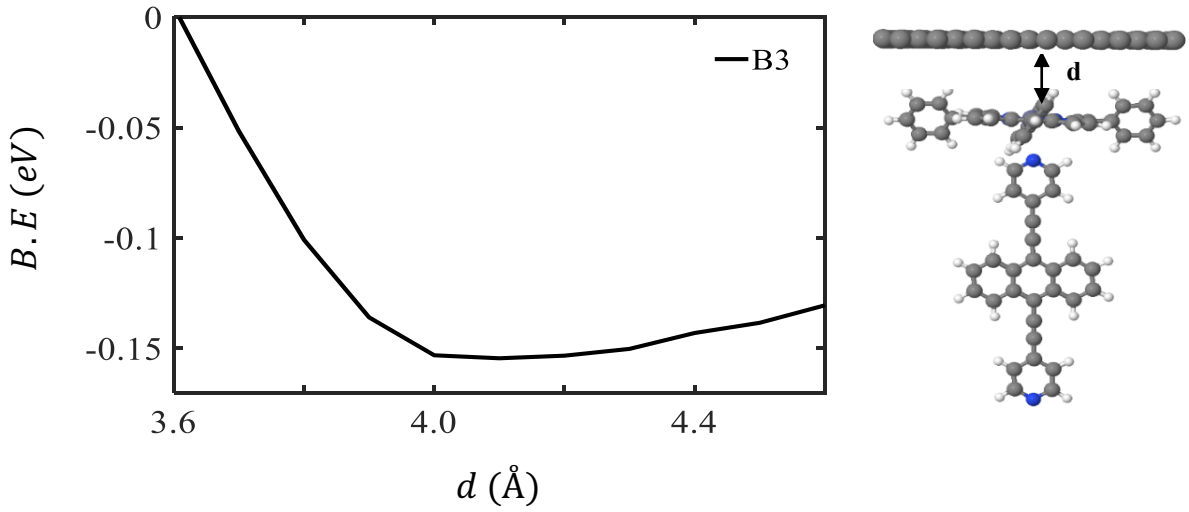

Figure 4.9: Right panel: Anthracene-based molecule combined with porphyrin (Zn-TPP), linked to Gr. **Left panel:** Binding energy versus distance plot of **B3** (Zn-TTP-Gr), where the optimum distance d is found to be 4 Å, at approximately 0.15 eV.

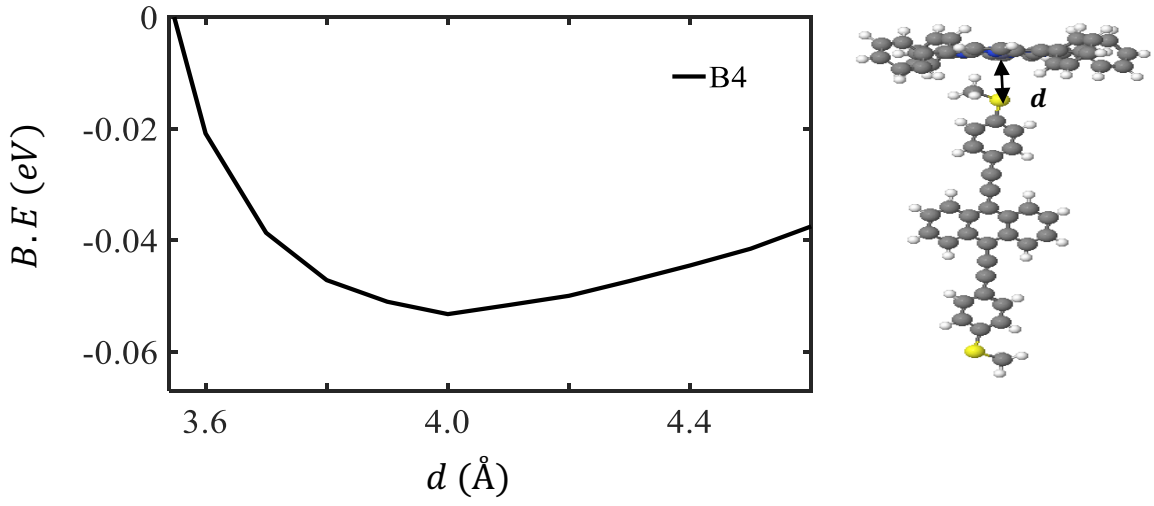

Figure 4.10: Right panel: Anthracene-based molecule with 2SMe anchors and (Zn-TPP). **Left panel:** Binding energy versus distance plot of **B4** (SMe-Zn-TTP), where the optimum distance d is found to be 4 Å, at approximately 0.05 eV.

Figures 4.7- 4.10 above determine the optimum distance between the two components of the four systems **B1**, **B2, B3,** and **B4** and as follows, d = (3, 2.3, 4.0 and 4.0 Å) and their corresponding binding energies (0.15, 0.50, 0.15 and 0.05 eV) of **B1**, **B2, B3,** and **B4** respectively. By comparing **B2** and **B4** one could tell that the pyridyl anchor binds 10 times stronger that the thioether (0.5 and 0.05 eV). This result is in excellent agreement with the XPS experimental measurements (see Figures 4.8 and 4.10). Based on these calculations, molecules **1** and **2** (SMe), are eliminated from this study and focus on molecules **3** and **4,** a pyridyl-terminated anthracene with two different connectivities.

4.4.2 Binding energy on gold substrate

After obtaining the optimum structures of the multicomponent shown in Figures 4.7-4.9 above, the next step is to find the optimum distance between the Au electrode and the anthracene or multicomponent.

In this section, another four binding energies **B5-B8** are calculated. **B5** is to find the optimum distance between the bare anthracene molecule and gold lead, **B6** is the optimum distance between (anthracene molecule + Gr, **B6**) and the gold lead, **B7** between (anthracene molecule + Zn-TTP, **B7**) and Au, **B8** between (**B7**+Gr) and Au.

The right panels of Figures 4.11-4.14 illustrate the four structures, while the left panels show the binding energy plots of **B5**, **B6, B7** and **B8.** The optimum distances are found to be 2.3, 2.4, 2.7, 2.4 Å and the corresponding binding energies are 0.4, 1, 0.50, 1.0 eV, of **B5**, **B6, B7** and **B8** respectively.

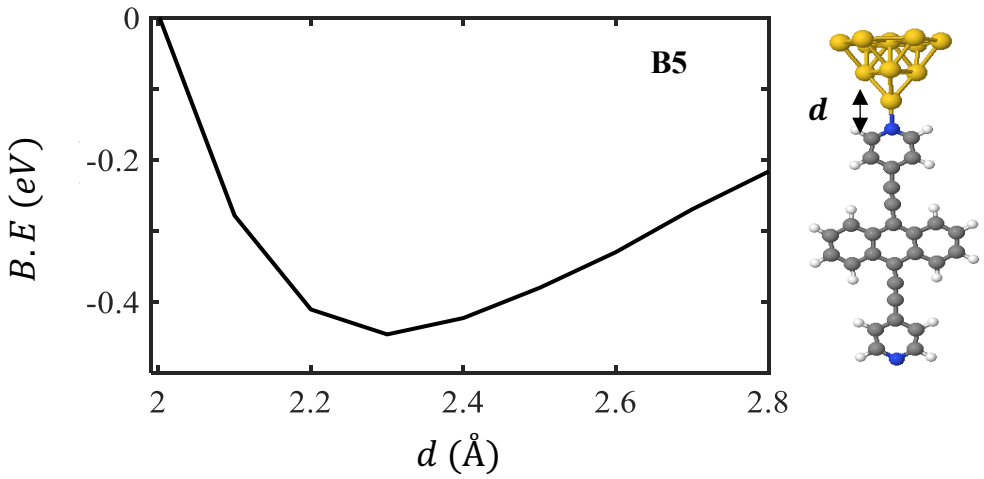

Figure 4.11: Right panel: Molecule configuration at the Au lead interface, anthracene-based molecule (2Py) linked to Au electrode. **Left panel: B5;** Binding energy plots as a function of distance d. This distance is found to be 2.3 Å, at approximately 0.4 eV.

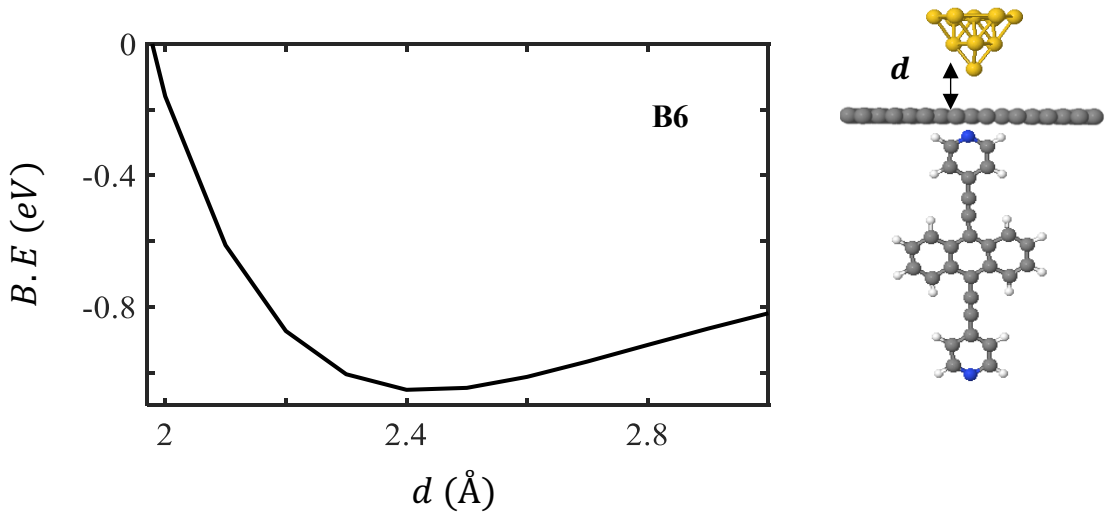

Figure 4.12: Right panel: Multicomponent configuration at the Au lead interface, anthracene-based molecule (2Py) with Gr sheet linked to Au electrode. **Left panel: B5;** Binding energy plots as a function of distance d. This distance is found to be 2.4 Å, at approximately 1 eV.

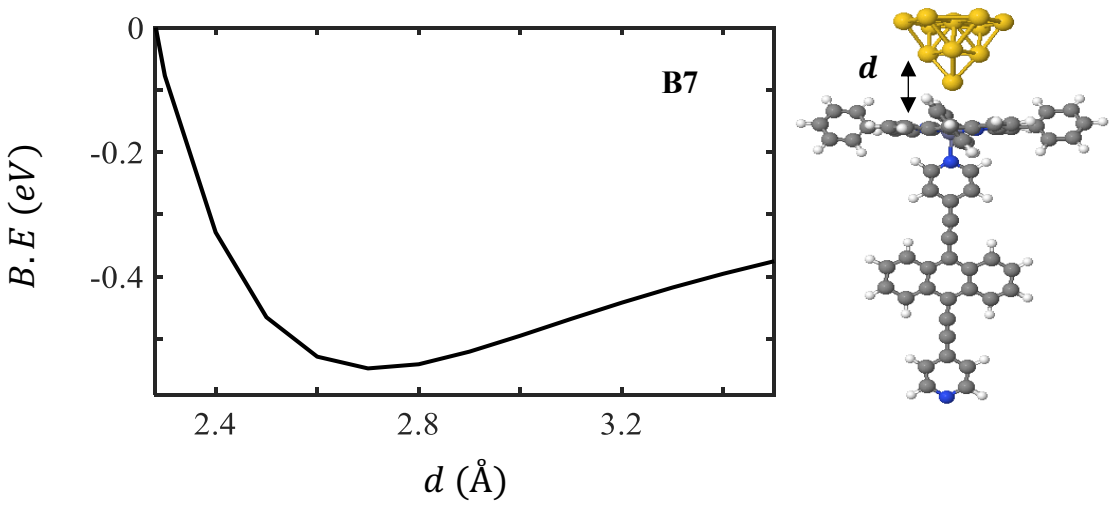

Figure 4.13: Right panel: Multicomponent configuration at the Au lead interface, anthracene-based molecule (2Py) with Zn-TTP molecule linked to Au electrode. **Left panel: B5;** Binding energy plots as a function of distance d. This distance is found to be 2.7 Å, at approximately 0.50 eV.

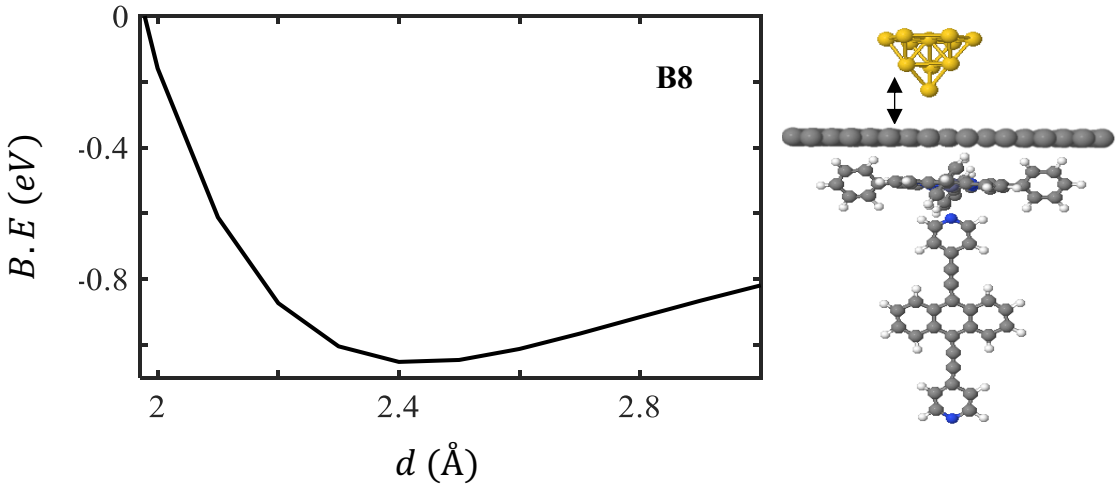

Figure 4.14: Right panel: Multicomponent configuration at the Au lead interface, anthracene-based molecule (2Py) with Zn-TTP+Gr linked to Au electrode. **Left panel: B5;** Binding energy plots as a function of distance d. This distance is found to be 2.4 Å, at approximately 1.00 eV.

Table 4.1 represents the optimum separation distance and binding energy of the eight studied structures **B1-B8**. **B1-B4** show the optimum separation distances and their corresponding binding energies of the multicomponent, means without Au substrate, while **B5-B8** show the optimum separation distances and their corresponding binding energies of the multicomponent bind to Au substrate. Based on the multicomponent calculations, I eliminate the thioether-terminated molecules **1** and **2** from this study as their binging energies to Zn-TTP are 10 times lower than the pyridyl-terminated. This theoretical result supports experimentally by the XPS measurements (see Figures 4.8 and 4.10). Comparing the multicomponent results against the Au results one can tell that Au binds stronger to these components than they bind to each other as shown in the second column of Table 4.1.

Table 4.1: Summarises the optimum separation distance and the binding energy calculations for the eight cases.

Compound	**B.E (eV)**	**d (Å)**
B1	0.15	3.0
B2	0.50	2.3
B3	0.15	4.0
B4	0.05	4.0
B5	0.40	2.3
B6	1.00	2.4
B7	0.50	2.7
B8	1.00	2.4

4.5 Tilt angle model

This section determines the tilt angle θ of each compound on a gold substrate, which corresponds to the experimentally measured most probable break-off distance (see table 4.2). Figure 4.15 illustrates a theoretical model of how the tilt angle θ varies between the tip and Au substrate.

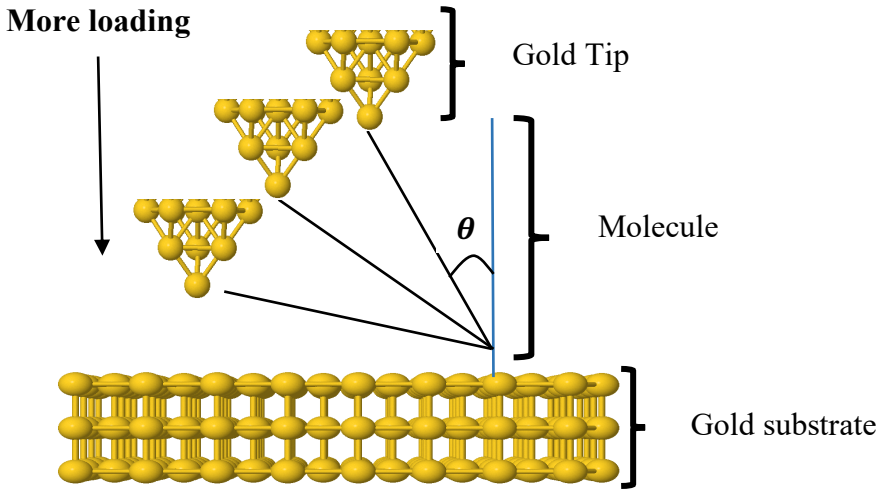

Figure 4.15: Representation of a tilt angle model, the more loading the larger tilt angle.

After eliminating molecules **1** and **2,** and for simplicity's sake, I am going to refer to the eight junctions as follows: **Au/3/Au** and **Au/4/Au** (***3*** *and* ***4*** *are bare molecules with* ***9-10*** *and* ***1-5*** *connectivities, respectively*), **Au/3/P/Au** and **Au/4/P/Au** (***3*** *and* ***4*** *plus porphyrin*), **Au/3/Gr/Au** and **Au/4/Gr/Au** (***3*** *and* ***4*** *plus graphene*), **Au/3/P/Gr/Au** and **Au/4/P/Gr/Au** (***3*** *and* ***4*** *plus porphyrin and graphene*). Table 4.3 shows the tilt angle of the eight compounds on Au substrate. Figure 4.16 represents the optimised structures of the eight compounds.

Table 4.2: Experimental break-off distance and equivalent tilt angle (θ), of the eight junctions.

Junction	Experimental film thickness (nm)	Experimental film roughness (nm)	Equivalent experimental tilt angle (θ)
Au/3/Au	1.23	0.2	38 °-55°
Au/4/Au	1.14	0.2	42 °-58°
Au/3/P/Au	1.81	0.4	38 °-55°
Au/4/P/Au	1.73	0.3	42 °-58°
Au/3/Gr/Au	1.23	0.2	38 °-55°
Au/4/Gr/Au	1.14	0.2	42 °-58°
Au/3/P/Gr/Au	1.81	0.4	38 °-55°
Au/4/P/Gr/Au	1.73	0.3	42 °-58°

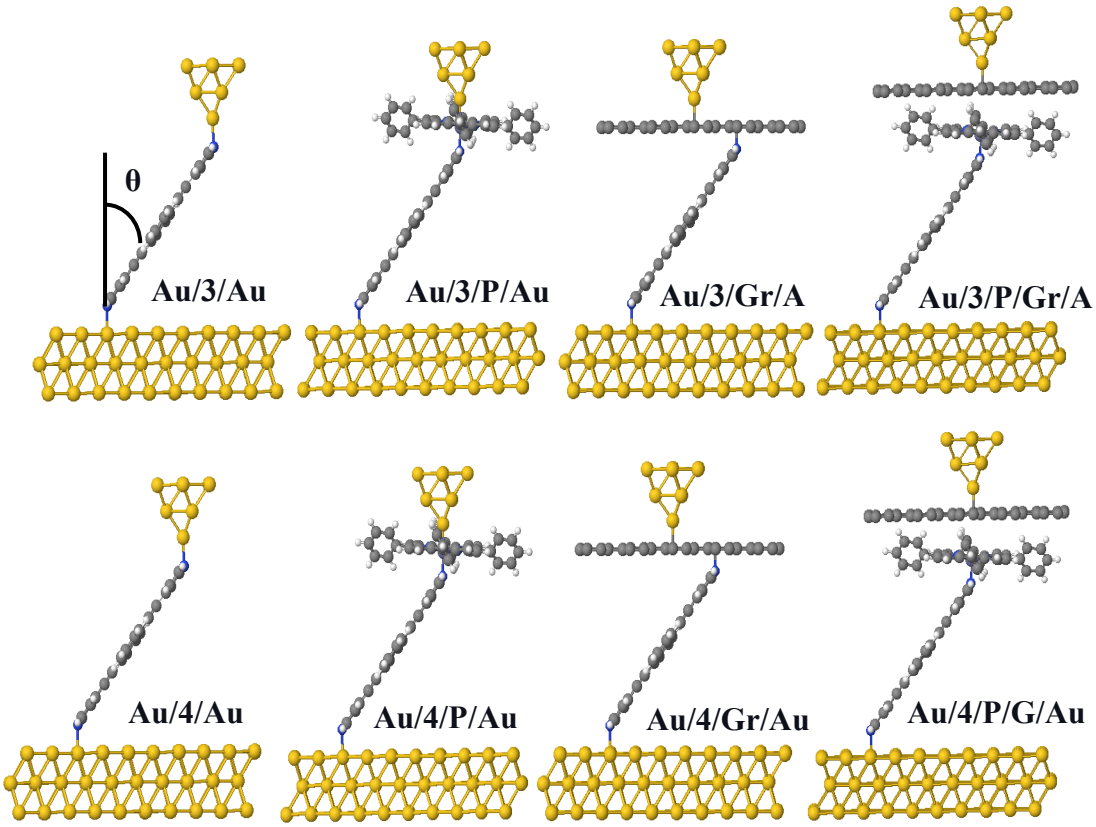

Figure 4.16: Optimised structures of the eight junctions, demonstrating the tilt-angle of the anthracene (side-view). **Au/3/Au**: Anthracene of **9, 10** connectivity, **Au/4/Au**: Anthracene of **1, 5** connectivity, **Au/3/Gr/Au**: anthracene **9, 10** connectivity with graphene sheet (G), **Au/4/Gr/Au**: anthracene **1, 5** connectivity with graphene sheet (G), **Au/3/P/Au**: anthracene **9, 10**) connectivity with ZnTPP (P), **Au/4/P/Au**: anthracene **1, 5** connectivity with ZnTPP (P), **Au/3/P/Gr/Au**: anthracene **9, 10** connectivity with P and G respectively, **Au/4/P/Gr/Au** : anthracene **1, 5** connectivitywith P and G respectively as well.

4.6 Tilt angle versus the conductance

This section aims to study the relation between the conductance G and the tilt angle θ, [15]. I am going to use two simple examples for this purpose: anthracene with two different connectivities **9, 10** and **1, 5**. In this model, I choose a range of tilt angle from 0^o to 90^o (step of 2 degrees).

Figures 4.17 and 4.19 prove that the relation between the transmission coefficient curve $T(E)$ and the tilt angle θ is to be a linear, means, the conductance increases with increasing the tilt angle as indicted by the green arrows. It is well-known that the Seebeck coefficient S is related to the slope of transmission coefficient curve. On the other hand, Figs. 4.18 and 4.20 determine the relation between the S and the tilt angle to be inverse, means large tilt angle possesses a small S.

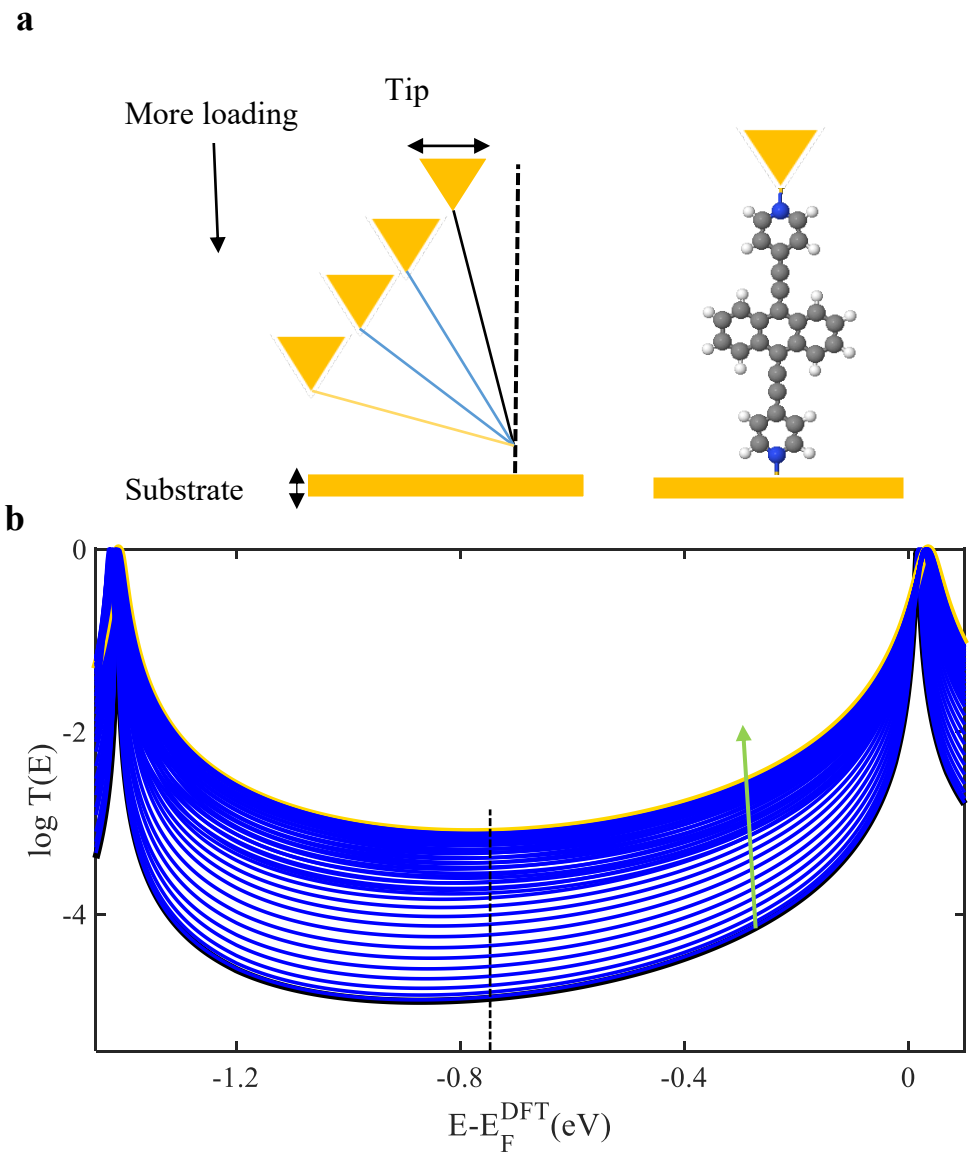

Figure 4.17: a: Representation of molecular junction with **9, 10** connectivity. **b:** Zero bias transmission coefficient $T\ (E)$ as a function of the tilt angle θ. The tilt angle varies from approximately 0^o (black curve) to 90^o (orange curve), here Fermi energy is chosen to be at mid-gap $E_F - E_F^{DFT}$= -0.77 eV, (black-line light pressure and green arrow points to towards heavy pressure, for).

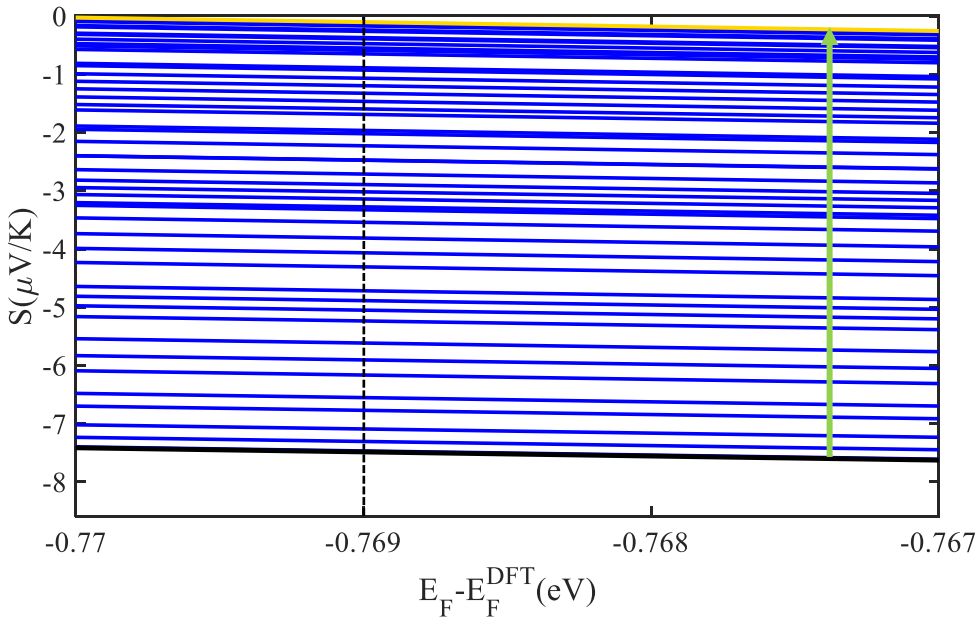

4.18: Seebeck coefficient S as a function pressure. The tilt angle varies from approximately 0^o (black curve) to 90^o (orange curve), at mid-gap $E_F - E_F^{DFT}$= -0.769 eV, (black-line light pressure and green arrow points to toward heavy pressure.

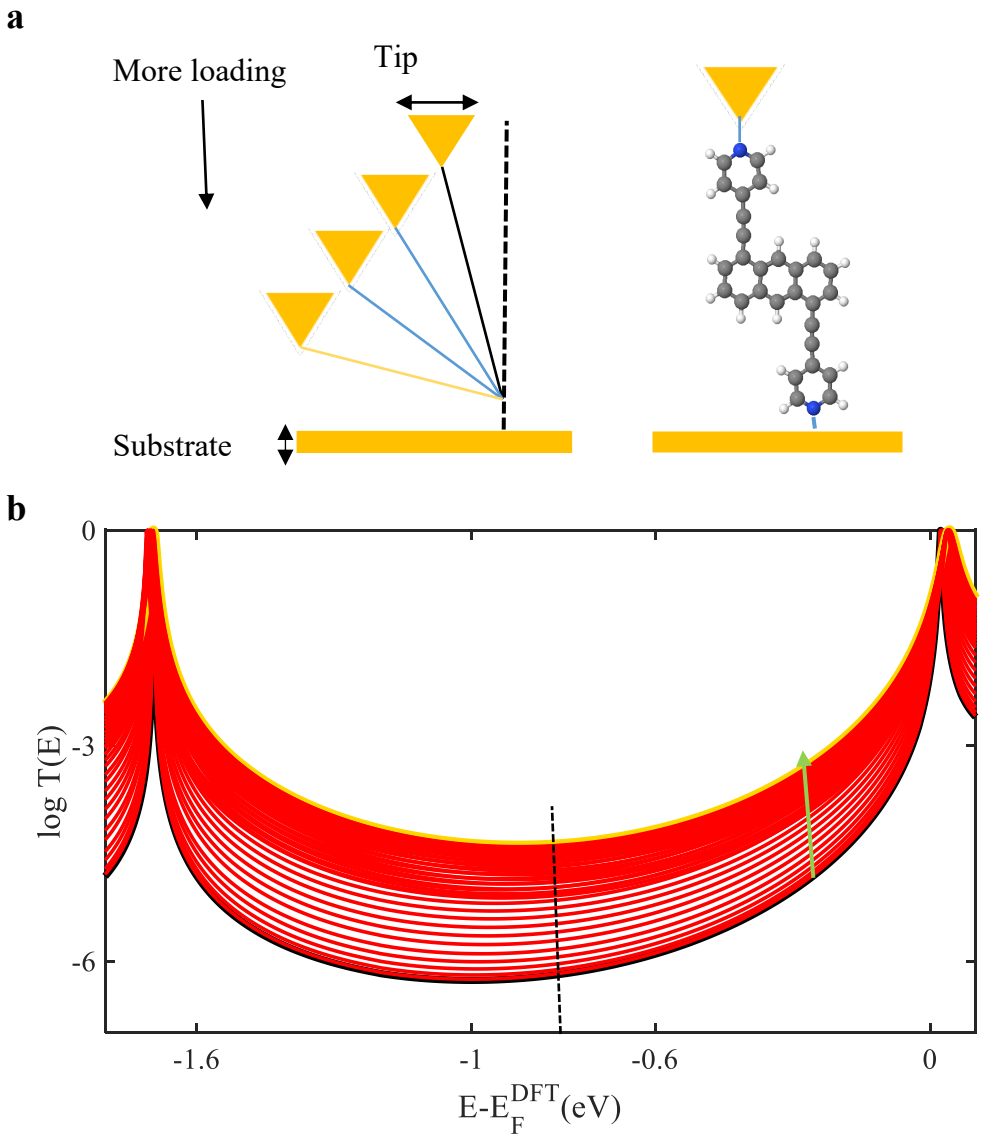

Figure 4.19: a: Representation of molecular junction with **1,5** connectivity. **b:** Zero bias transmission coefficient $T\,(E)$ as a function of the tilt angle θ. The tilt angle varies from approximately 0^o (black curve) to 90^o (orange curve), here Fermi energy is chosen to be at mid-gap $E_F - E_F^{DFT}$= -0.80 eV, (black-line light pressure and green arrow points to towards heavy pressure).

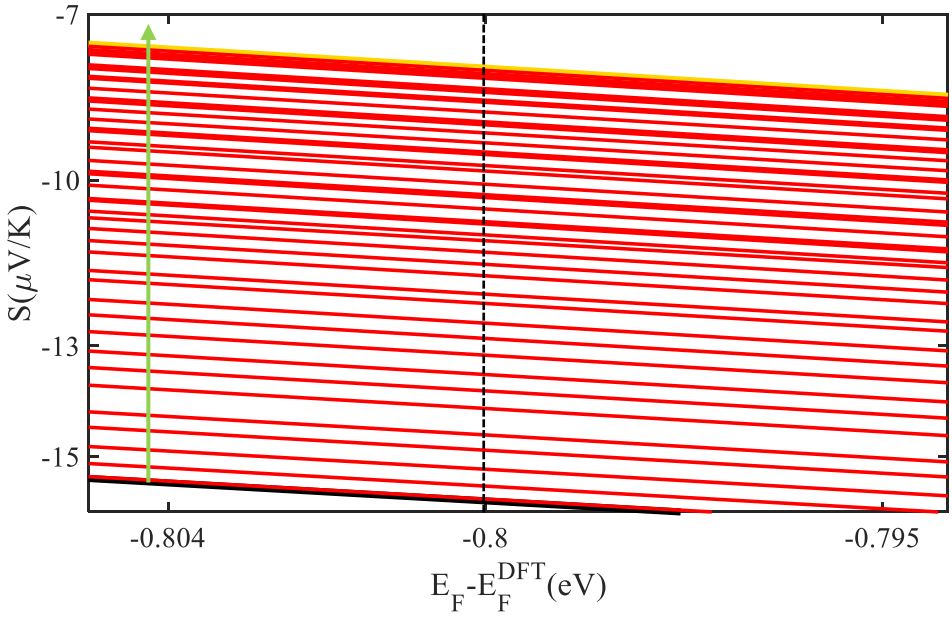

Figure 4.20 Seebeck coefficient S as a function pressure. The tilt angle varies from approximately 0^o (black curve) to 90^o (orange curve), at mid-gap $E_F - E_F^{DFT}$= -0.80 eV (black -line light pressure and green arrow points to toward heavy pressure).

4.7 Transmission coefficient T (E)

The transmission coefficient curves *T(E)* were calculated for the eight junctions using the Gollum transport code [11], based on the tilt angles (Table 4.2**)**. Despite the fact that the LUMO resonance is predicted to be pinned near the Fermi Level $E - E_F^{DFT}$ of the electrodes for these eight junctions due to the present of the pyridyl anchor group, previous comparisons between theory and experiment suggest that better agreement is obtained when the Fermi level is closer to the mid gap ($E - E_F^{DFT} \sim mid\ gap$), [12-15], (see black-dashed lines in the bottom panels of the Figures. 4.21- 4.24).

Furthermore, a change in the connectivity is expected to cause a change in the conductance with a ratio of 16, as predicts by the magic ratio theory [16]. This ratio has been measured and calculated to be around 15 for four anthracene-based molecules with two different anchors including thioacetate and thioether (SAc and SMe), [12]. The present study employs the same anthracene-based molecule with the same connectivities **1, 5** and **9, 10** only differs by the anchor where the pyridyl replaces the SAc or SMe.

Changing the anchor from thioacetate or thioether to pyridyl leads to change the transmission coefficient *T(E)* from a HOMO-dominated curve to a LUMO-dominated curve as demonstrates in the present study (Figure 4.21-4.24), [13]. It is worth mentioning, that the Seebeck coefficient is related to the slope of the transmission as shown in equation 4.3:

$$S = -\frac{\pi^2 k_B^2 T}{3e} \frac{\partial ln\big(T(E)\big)}{\partial E}\bigg|_{E=E_F} \qquad 4.3$$

Thus, changing the curve from HOMO to LUMO or vice versa resulting in switching the sign of the Seebeck coefficient, I will discuss this later.

In the present study the ratio between the two connectivies **9, 10** and **1, 5** (simply **3** and **4**), depends on whether the junction contains bare molecule or multicomponent and the tilt angle θ. For example, the ratio of the bare molecule is approximately 11, and when it binds to porphyrin this ratio decreases to about 2, then increases to 20 when it combines with graphene Gr. This ratio reduced significantly when both porphyrin and graphene Gr combine with the bare molecule to be roughly 2 (note: this ratio varies depending on Fermi energy location, here, $E - E_F^{DFT} \sim mid\ gap$). The magic ratio broke down because my junctions become complex.

After determining the optimum separation distance d of the multicomponent and between them and the Au substrate using the counterpoise method (section 4.5). I then investigate the role of the tilt angle θ, by employing a theoretical model (section 4.7), and take a guide from the experimental measurements to determine the right tilt angle for each junction. Eventually, I calculate the transmission coefficient of the 8 junctions and as follows:

The top panel of Figure 4.21, shows the bare anthracene-based molecules **Au/3/Au** and **Au/4/Au** of different connectivities **9, 10** and **1, 5** respectively, with the Py anchor groups.

The transmission coefficient $T(E)$ curve calculates based on the tilt angle θ shown in Table 4.2, where different curves of the same colour correspond to different title angles and the yellow line is the average. As it mentioned above, the Fermi energy is placed approximately in the mid-way between the HOMO and LUMO resonances. For these junctions (**Au/3/Au** and **Au/4/Au**), the Fermi Energy is $E - E_F^{DFT} =$ -0.8 eV (black dashed-line), and the conductance are calculated to be 3.8 and 4.6, respectively. The product rule predicts a constructive quantum interference CQI for both connectivities as discussed previously (Figs 4.2-4.5, section 4.4

Frontier orbitals), DFT results prove this prediction to be correct. It is worth mentioning, that the HOMO-LUMO gap for **Au/3/Au** is about -0.3 eV smaller than **Au/4/Au**, as shown in the lower panel of Figure. 4.21.

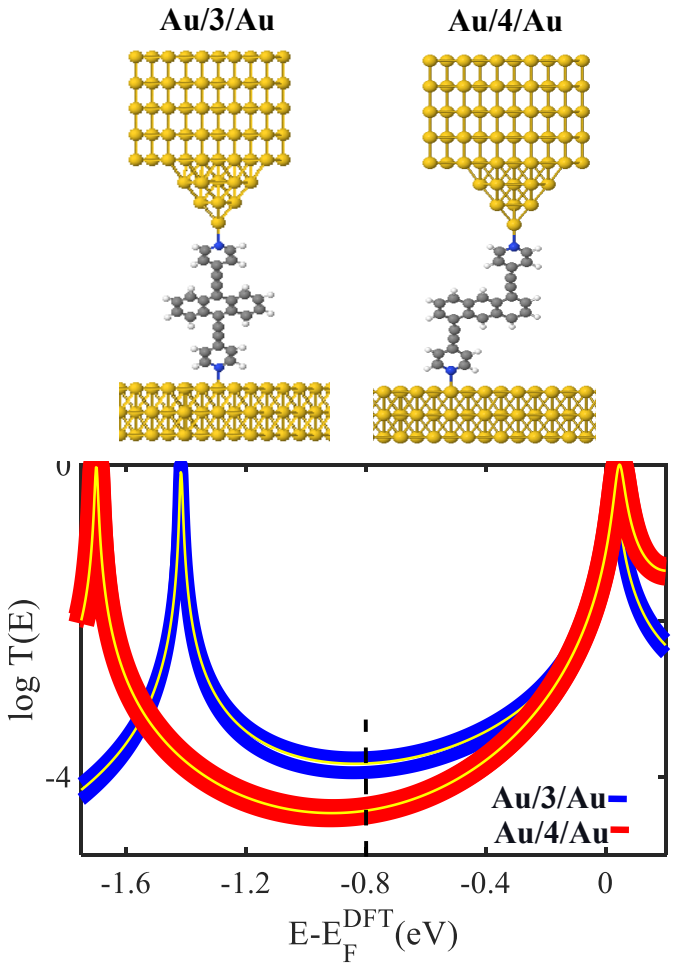

Figure 4.21: (**Top panel**): Schematic illustrations of molecular junctions of **Au/3/Au** and **Au/4/Au**. **(Bottom panel):** Zero bias transmission coefficient $T(E)$ of molecules **Au/3/Au** and **Au/4/Au** against electron energy E. **Au/3/Au** (blue solid-line) and **Au/4/Au** (red solid-line). Different curves of the same colour correspond to different tilt angle θ, (the yellow line is the average).

The next step is to combine the ZnTPP with anthracene-based molecules **Au/3/P/Au** and **Au/4/P/Au** of different connectivities **9, 10** and **1, 5** respectively as shown in the top panel Figure 4.22. Also, this $T(E)$ demonstrates based on the tilt angle θ shown in Table 4.2, where different curves of the same colour correspond to different title angles and the yellow line is the average. As previously indicated, the Fermi energy is considered approximately in the vicinity of the mid gap. This (Fermi energy) can be defined at $E - E_F^{DFT}$ = -0.76 eV (black dashed-line), for **Au/3/P/Au** and **Au/4/P/Au**. For these junctions (**Au/3/P/Au** and **Au/4/P/Au**), the conductance is calculated to be -4.0 and -4.9 eV, respectively. It is worth pointing out that the HOMO-LUMO gap for **Au/3/P/Au** is about -1.41 eV, and it is a slightly smaller than **Au/4/P/Au**, as shown in the lower panel of Figure. 4.22.

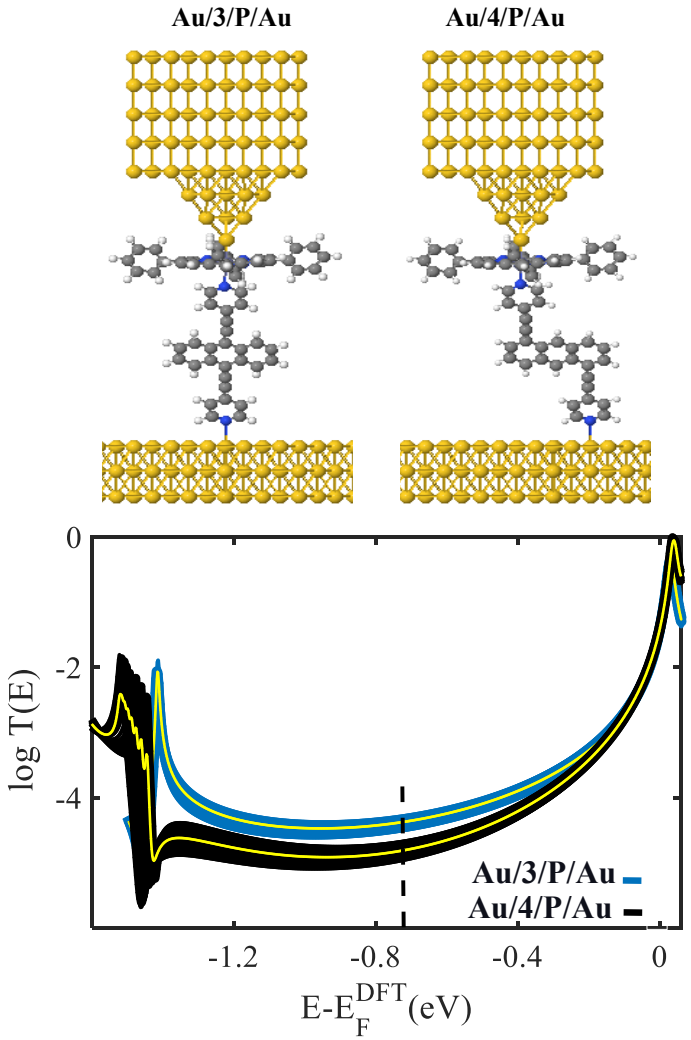

Figure 4.22 :(**Top panel):** Schematic illustrations of molecular junctions for **Au/3/P/Au** and **Au/4/P/Au. (Bottom panel):** Zero bias transmission coefficient *T(E)* of **Au/3/P/Au** and **Au/4/P/Au** against electron energy E. **Au/3/P/Au** (light blue solid-line) and **Au/4/P/Au** (black solid-line). Different curves of the same colour correspond to different tilt angles. The yellow line is the average of the four curves.

Adding a graphene sheet Gr to the anthracene-based molecule with both connectivities **9, 10** and **1, 5** is also investigated as shown in Figure 4.23 the top panel represents **Au/3/Gr/Au** and **Au/4/Gr/Au** based on the binding energy of multicomponent (Figs. 4.23). The bottom panel of Figure 4.23 shows the transmission curves, based on tilt angles, $T(E)$ as a function of energy. The Fermi energy is located to be approximately -0.48 eV as consider to be in the vicinity of the mid gap. The values of conductance are 3.9 and 4.8 of **Au/3/Gr/Au** and **Au/4/Gr/Au**, respectively. It is worth pointing out that the HOMO-LUMO gaps of **Au/3/Gr/Au** and **Au/4/Gr/Au** are roughly identical with -0.98 eV and -1.04 eV, respectively.

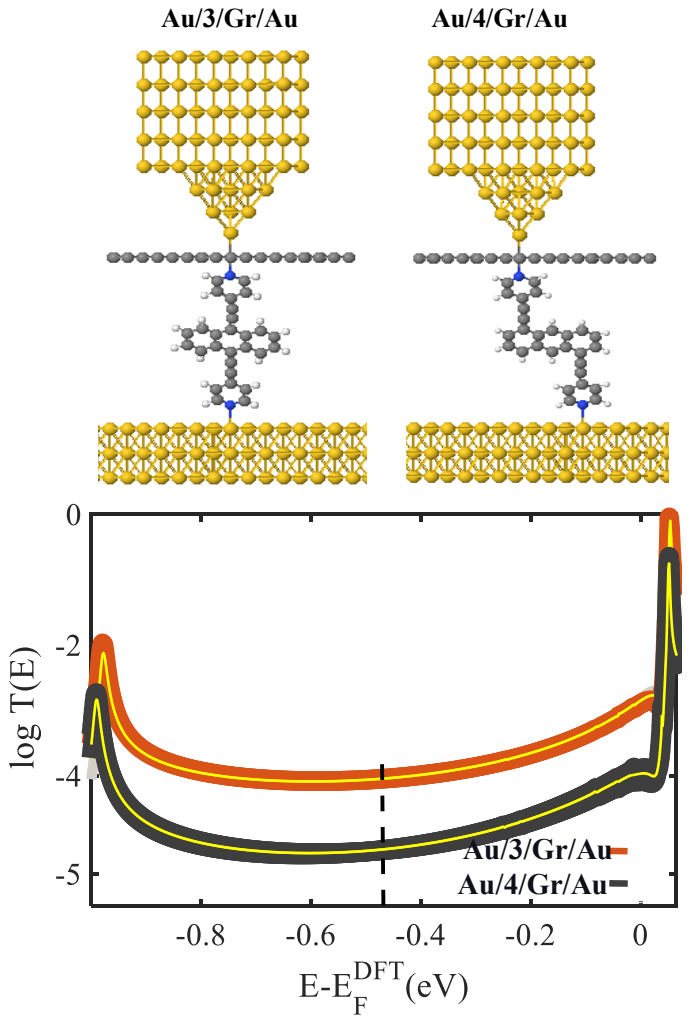

Figure 4.23: (**Top panel):** Schematic illustrations of molecular junctions for **Au/3/Gr/Au** and **Au/4/Gr/Au. (Bottom panel):** Zero bias transmission coefficient $T(E)$ of **Au/3/Gr/Au** and **Au/4/Gr/Au** against electron energy E. **Au/3/Gr/Au** (orange solid-line) and **Au/4/Gr/Au** (grey solid-line). Different curves of the same colour correspond to different tilt angles. The yellow line is the average of the four curves.

The last junction is more complex, as I combine both Porphyrin (ZnTPP) and graphene sheet, to the anthracene-based cores then I connecte them to gold electrodes, as shown in the top panel of Figure 4.24. The bottom panel represents the transmission curves, based on tilt angles, $T(E)$ as a function of energy. and the Fermi energy value locate at the mid gab, $E - E_F^{DFT}$ = -0.70 eV. The transmission coefficient $T(E)$ values are 5.5 and 6.4 **Au/3/P/Gr/Au**

and **Au/4/P/Gr/Au**, respectively. One could notice a destructive quantum interference DQI for both junctions at approximately $E - E_F^{DFT}$ = -1.3 eV, however, this feature is not useful because it locates close to HOMO resonance and junction is a LUMO dominated (far away from $E - E_F^{DFT}$). Again, the HOMO-LUMO gaps of **Au/3/P/Gr/Au** and **Au/4/P/Gr/Au** are identical -1.25 and -1.28 eV, respectively.

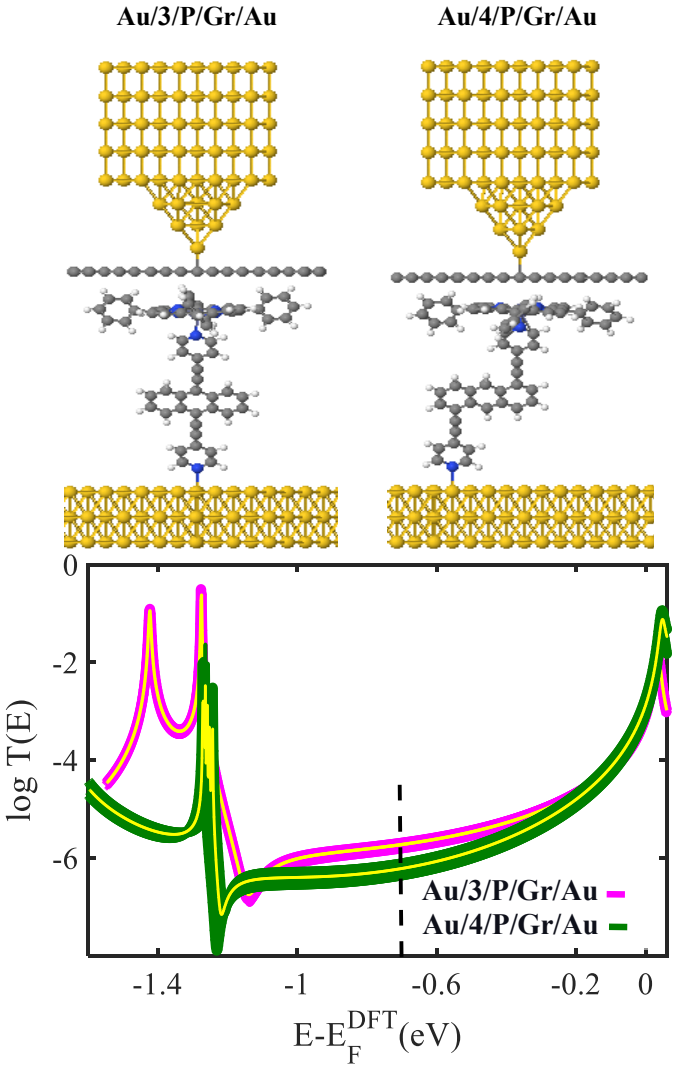

Figure 4.24: (**Top panel):** Schematic illustrations of molecular junctions for **Au/3/P/Gr/Au** and **Au/4/P/Gr/Au. (Bottom panel):** Zero bias transmission coefficient *T (E)* of **Au/3/P/Gr/Au** and **Au/4/P/Gr/Au** against electron energy E. **Au/3/P/Gr/Au** (pink solid-line)

and **Au/4/P/Gr/Au** (green solid-line)**.** Different curves of the same colour correspond to different title angles and the yellow line is the average of the four curves.

4.8 Seebeck coefficient *S*

After computing the electronic transmission coefficient for the eight junctions, I now compute their Seebeck coefficients S . To this end, it is useful to introduce the non-normalised probability distribution $P(E)$ defined by

$$P(E) = -T(E)\frac{df(E)}{dE} \qquad 4.4$$

Where $f(E)$ the Fermi is function and $T(E)$ are the transmission coefficients and whose moments L_i are denoted as follows

$$L_i = \int dEP(E)(E - E_F)^i \qquad 4.5$$

Where, E_F is the Fermi energy. The Seebeck coefficient, S and electrical conductance G are then given by

$$S(T) = -\frac{1}{|e|T}\frac{L_1}{L_0} \qquad 4.6$$

$$G = \frac{2e^2}{h}L_0 \qquad 4.7$$

Where, e is the electronic charge. Figures 4.25-4.28 show the Seebeck coefficient S evaluated at room temperature for different energy range $E_F - E_F^{DFT}$.

To calculate the Seebeck coefficient S for the studied junctions below, I used DFT combined with the quantum transport code Gollum. Figures 4.25-4.28 show the corresponding the S as a function of the Fermi energy E_F using the tilt angle model.

The thermopower has been calculated for the eight junctions (Figure 4.16), where the E_F is placed at the mid gap of HOMO-LUMO. These calculations are based on tilt angles, (different curves of the same colour correspond to different title angles, and the yellow line is the average).

Firstly, Figure 4.25 illustrates the bare anthracene molecule with the two connectivities **9, 10** and **1, 5** (**Au/3/Au** and **Au/4/Au,** respectively). The Seebeck coefficients S for these junctions are determined at $E_F - E_F^{DFT}$= -0.8 eV. The blue solid-line and the red solid-line correspond to different tilt angles (Tilt angle model). The S sign the two junctions were found to be negative. The S value for **Au/3/Au** is -2.5 V/K , whereas -9.9 $\mu V/K$ for **Au/4/Au.** Secondly, Figure 4.26 shows the anthracene-based molecule with the connectivities linked to the graphene sheet (top panel labelled **Au/3/P/Au** and **Au/4/P/Au)**. The S is obtained at $E_F - E_F^{DFT}$= -0.48 eV. It is found to be -11 and -12 $\mu V/K$ for **Au/3/P/Au** and **Au/4/P/Au,** respectively. While, the anthracene molecules attached to Zn-TPP are represented by **Au/3/Gr/Au** and **Au/4/Gr/Au**, as shown in Figure 4.27 (top panel). The bottom panel, the S values (at $E_F - E_F^{DFT}$= -0.76 eV) are -10 and -11 $\mu V/K$ for **Au/3/Gr/Au** and **Au/4/Gr/Au,** respectively. Finally, I linked the bare molecules to both Zn-TPP and graphene sheet Gr, as represented in Figure 4.28 (top

panel). Then, in the bottom panel, the S is determined at $E_F - E_F^{DFT}$= -0.70 eV. Its values are -16 and -20 $\mu V/K$ for **Au/3/P/Gr/Au** and **Au/4/P/Gr/Au.**

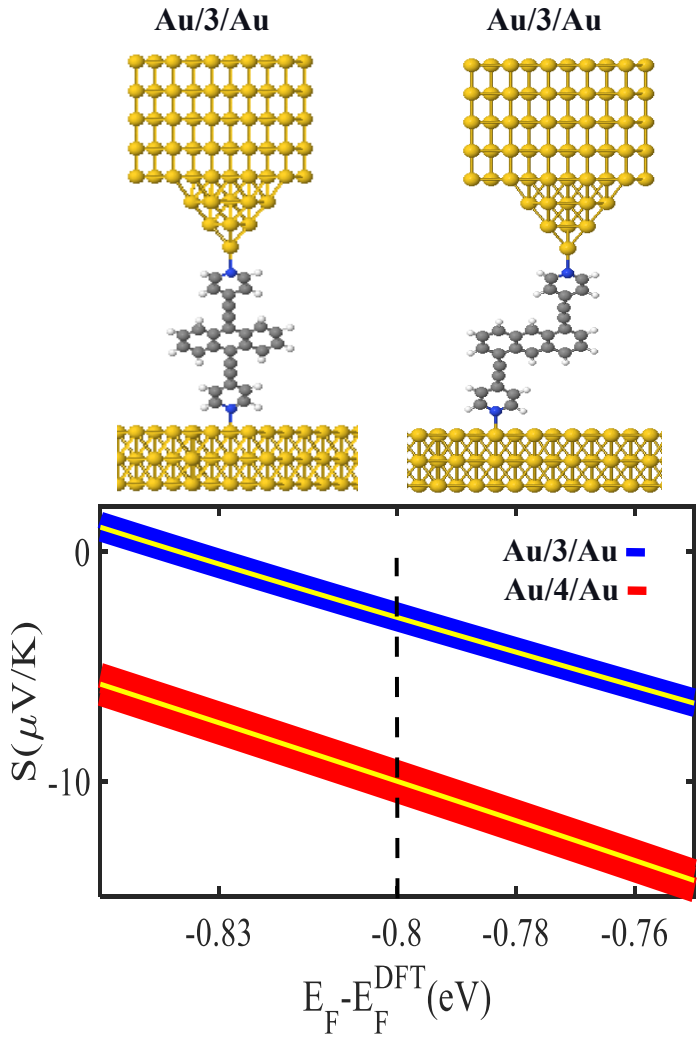

Figure 4.25: (**Top panel):** Schematic illustrations of molecular junctions for **Au/3/Au** and **Au/4/Au. (Bottom panel):** Seebeck coefficient S of molecules **Au/3/Au** and **Au/4/Au** against electron energy E. **Au/3/Au** (blue solid-line) and **Au/4/Au** (red solid-line)**.** Different curves of the same colour correspond to different title angles and the yellow line is the average of the four curves.

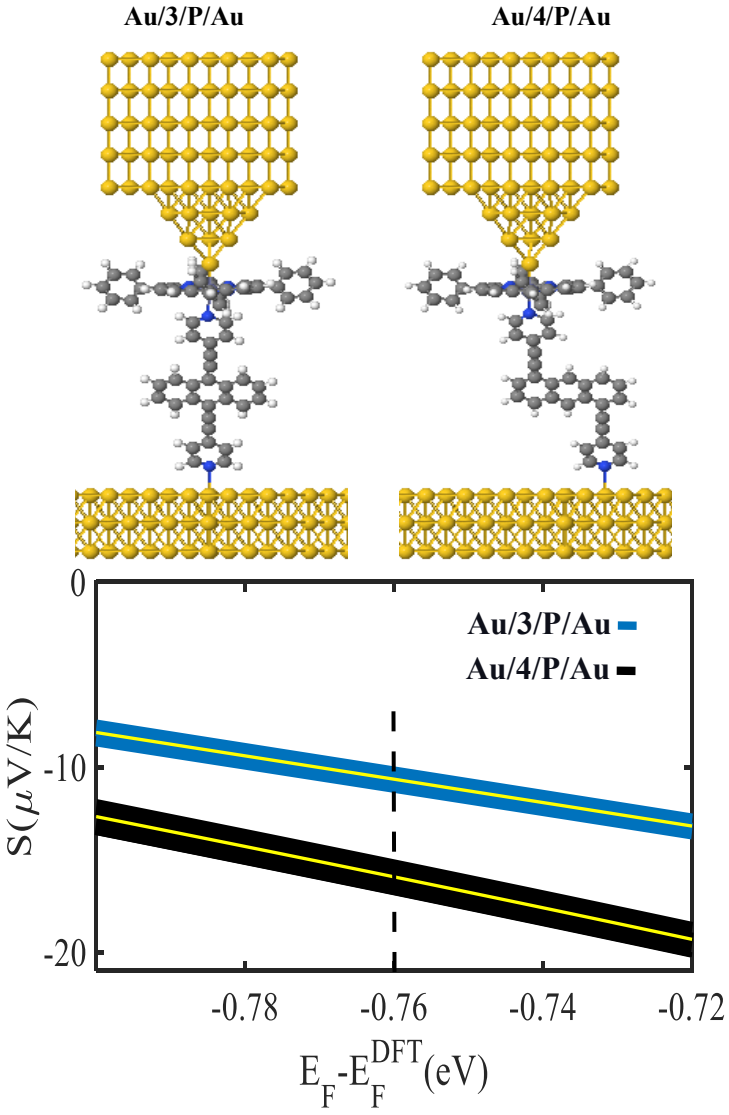

Figure 4.26: (**Top panel):** Schematic illustrations of molecular junctions for **Au/3/P/Au** and **Au/4/P/Au. (Bottom panel):** Seebeck coefficient *S* of molecules **Au/3/P/Au** and **Au/4/P/Au** against electron energy E. **Au/3/P/Au** (light blue solid-line) and **Au/4/P/Au** (black solid-line)**.** Different curves of the same colour correspond to different title angles and the yellow line is the average of the four curves.

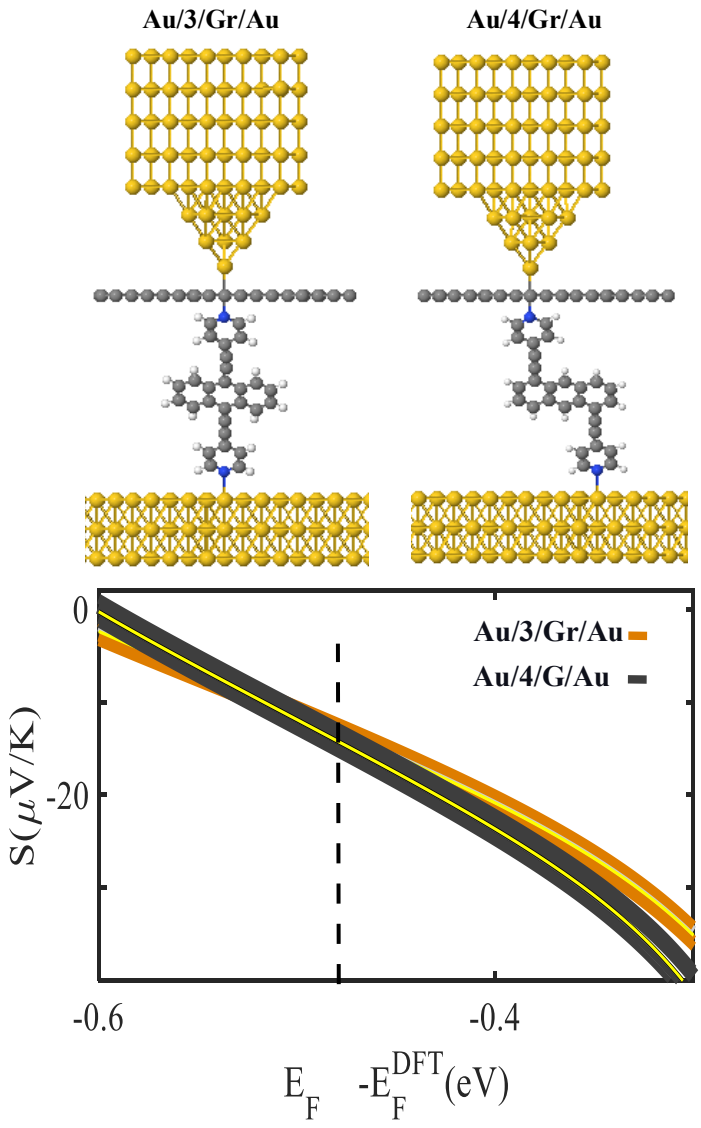

Figure 4.27: (**Top panel):** Schematic illustrations of molecular junctions for **Au/3/Gr/Au** and **Au/4/Gr/Au. (Bottom panel):** Seebeck coefficient *S* of molecules **Au/3/Gr/Au** and **Au/4/Gr/Au** against electron energy E. **Au/3/Gr/Au** (orange solid-line) and **Au/4/Gr/Au** (gray solid-line)**.** Different curves of the same colour correspond to different title angles and the yellow line is the average of the four curves.

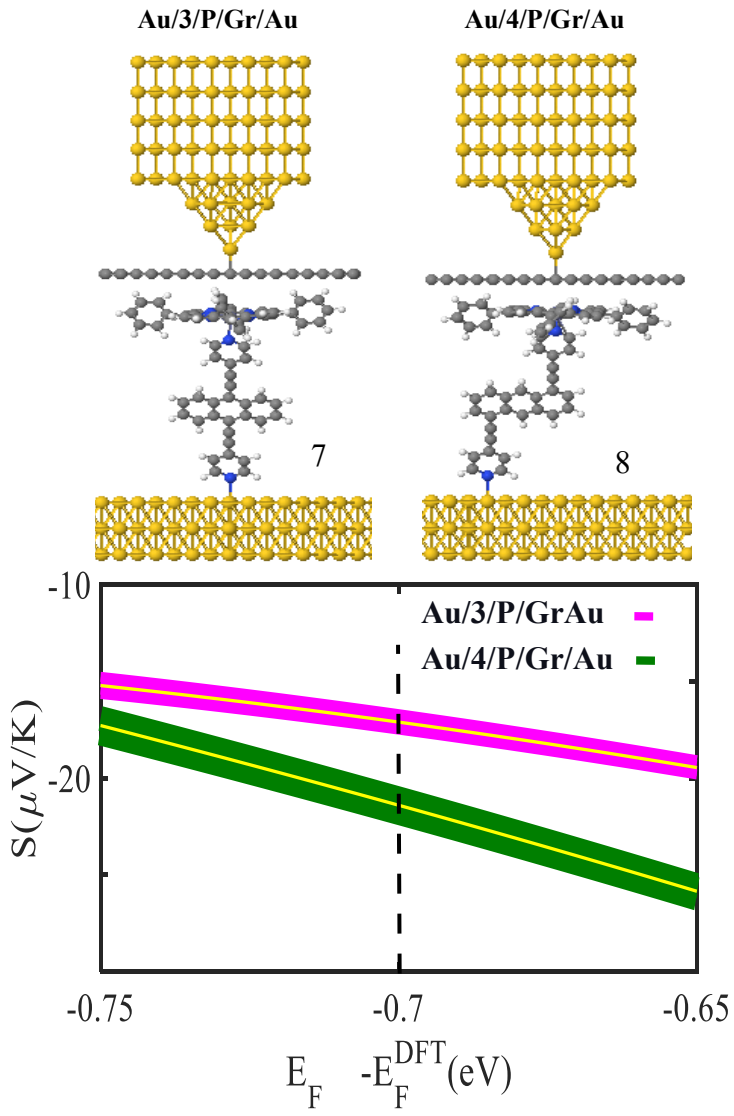

Figure 4.28: (**Top panel):** Schematic illustrations of molecular junctions for **Au/3/P/Gr/Au** and **Au/4/P/Gr/Au. (Bottom panel):** Seebeck coefficient *S* of molecules **Au/3/P/Gr/Au** and **Au/4/P/Gr/Au** against electron energy E. **Au/3/P/Gr/Au** (pink solid-line) and **Au/4/P/Gr/Au** (green solid-line)**.** Different curves of the same colour correspond to different title angles and the yellow line is the average of the four curves.

4.9 Theory versus experiment

As it mentioned at the beginning of this chapter, this is a joint study with experimental groups. Here, I am going to test my theoretical simulation against the measurements. I will begin with the prediction first, as the binding energy calculations suggest that the anthracene-based molecule with thioether linker group does not bind to a porphyrin slippery anchor through the Zn. This calculation performs in gas phase with multicomponent for two anthracene-based molecules. The two anthracene molecules mainly differ by the linker groups, one with pyridyl and one with thioether. The total energy difference points out that Py linker binds 10 times stronger than SMe. The XPS measurement proves the theoretical simulations to be accurate.

The second prediction is led by the magic ratio theory [16], where it predicts this ratio for the two connectivities (**3** and **4**), to be 16. My DFT calculations were 11 for the bare molecules, 14 when I add Zn-TPP, 13 when it combines with Gr, and this ratio reduced significantly when both porphyrin and graphene Gr combine with the bare molecule to be roughly 2. Nevertheless, the case is more complicated when there is a multicomponent, however, the theory and experiment agree that the room temperature low bias conductance for **9, 10** connectivity is always greater than the conductance for **1, 5** connectivity. This is a signature of quantum interference [13-16], which again predicts by product rule [8]. (Figs. 4.2 – 4.5 wavefunctions plots).

Up to this point, I covered the theory predictions against the experimental measurements. Next, I compute the theoretical electrical conductance and Seebeck coefficient of the 8 junctions and compare them to the corresponding measured ones. Figure 4.29 shows the computed room-temperature Seebeck coefficients of the 8 different molecular structures given in Figure 4.16. Previous comparisons,[17], between experiment and theory revealed that electron transport

through poly-aromatic hydrocarbons takes place near the middle of the energy gap between the highest occupied molecular orbital (HOMO) and the lowest unoccupied molecular orbital (LUMO), and indeed we find that the closest agreement between theory and experiment is obtained for a Fermi energy near the mid-gap, as indicated by the vertical dashed lines in Figure 4.21-4.24. As expected from literature studies of single molecules, electron transport through the eight junctions is LUMO dominated (due to the presence of pyridyl anchors), leading to the negative sign of the Seebeck coefficient for the 8 molecules, as shown in the lower panel of Figure 4.29, [12-15]. As shown in Figure 4.29, both experiment and theory reveal that addition of **Zn-TPP** tends to decrease the conductance of the **Au/3/Pt** and **Au/4/Pt** SAMs whilst increasing the magnitude of their Seebeck coefficients. Furthermore, the conductances of SAMs formed from **3** are generally higher than those formed from **4**, reflecting the higher degree of CQI in the former. Experimentally, the conductances of **Au/3/P/Gr/Pt** and **Au/4/P/Gr/Pt** were measured to be close to those of **Au/3/P/Pt** and **Au/4/P/P**t respectively and similarly, the conductances of **Au/3/Gr/Pt** and **Au/4/Gr/Pt** were measured to be close to those of **Au/3/Pt** and **Au/4/P**t respectively, revealing that inclusion of the graphene layer had a negligible effect on electrical conductance. In contrast, theory reveals that if the fraction of molecules making contact with the electrodes is unchanged by the inclusion of the graphene layer, then inclusion of the latter would be expected to decrease the conductance. This suggests that the higher binding energy associated with the graphene layer increases the fraction of molecules making contact with the top electrode. The experimental observation that inclusion of graphene barely affects electrical conductance is of interest, because it may present an opportunity for independently tuning thermal conductance by varying the phonon mismatch across the electrode-molecule boundary.

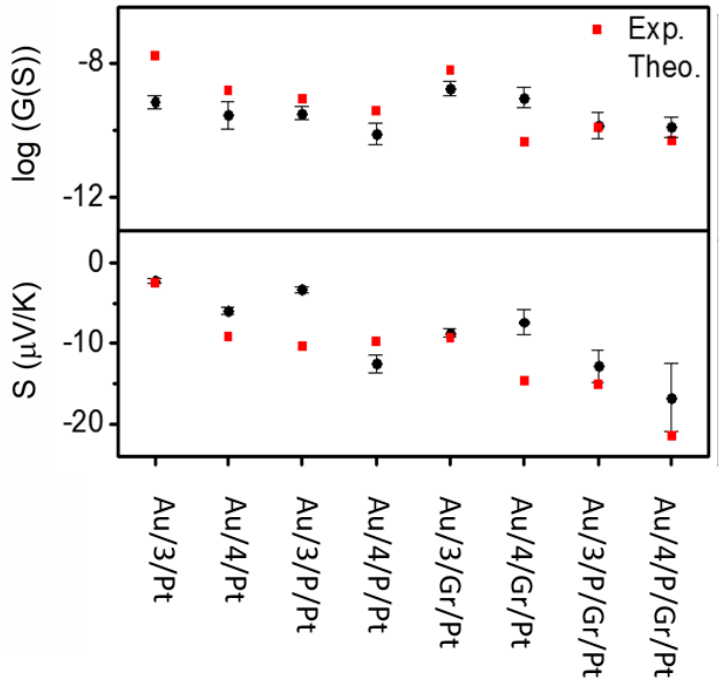

Figure 4.29: Electrical and thermoelectrical properties of the eight junctions. A comparison between experiment and theory (black-circles experiment and red-squares theory).

4.10 Conclusion

We have utilized multi-layered self-assembly and asymmetric design to boost the Seebeck coefficient's of self-assembled monolayers. Solution-based NMR experiments were used to successfully predict the ability of a series of anthracene-based molecular wires to bind to a porphyrin. Through this binding, SAMs of these molecules were able to stabilize addition of a porphyrin layer to their top-face. These SAMs were characterized extensively through the use of AFM and XPS both with and without the inclusion of **Zn-TPP**, confirming the discrete structure of these systems and demonstrating a clear translation between the binding behaviour of the molecules in solution and at the mesoscopic scale on a surface. Figure 4.29 demonstrates that when starting from an anthracene-based SAM formed from **3** or **4**, subsequent addition of either a porphyrin layer or a graphene layer can act to significantly increase their Seebeck coefficients, and addition of both porphyrin and graphene can lead to further increases. We also note that a number of these multi-component systems retain strong features associated with CQI. Finally, our experimental work shows that this methodology can be applied to tailor each end of a molecular junction to different electrode materials. The fabrication of these novel 'sticky' to 'slippery' linker systems presents a significant breakthrough in the field of molecular electronics, overcoming the need for rigid-contacts to metallic electrodes, a critical step in the design of future thin film devices. This study could also reasonably be extended to further work in tailoring different ends of a multicomponent system to different materials, as a route towards decoupling electronic and thermal contributions in the generation of thermopower. We are currently undertaking work to simulate new 'sticky' and 'slippery' linkers and engineer more efficient devices utilizing this methodology.

4.11 Bibliography

1. Rincón-García, L., Ismael, A. K., Evangeli, C., Grace, I., Rubio-Bollinger, G., Porfyrakis, K., and Lambert, C. J. (2016). Molecular design and control of fullerene-based bi-thermoelectric materials. *Nature materials*, *15*(3), 289-293.
2. Zhang, Y., and Park, S. J. (2017). Enhanced interfacial interaction by grafting carboxylated-macromolecular chains on nanodiamond surfaces for epoxy-based thermosets. *Journal of Polymer Science Part B: Polymer Physics*, *55*(24), 1890-1898.
3. Sangtarash, S., Sadeghi, H., and Lambert, C. J. (2018). Connectivity-driven bi-thermoelectricity in heteroatom-substituted molecular junctions. *Physical Chemistry Chemical Physics*, *20*(14), 9630-9637.
4. Rincón-García, L., Ismael, A. K., Evangeli, C., Grace, I., Rubio-Bollinger, G., Porfyrakis, K., and Lambert, C. J. (2016). Molecular design and control of fullerene-based bi-thermoelectric materials. *Nature materials*, *15*(3), 289-293.
5. Tan, A., Sadat, S., and Reddy, P. (2010). Measurement of thermopower and current-voltage characteristics of molecular junctions to identify orbital alignment. *Applied Physics Letters*, *96*(1), 013110.
6. Ismael, A. K., Wang, K., Vezzoli, A., Al-Khaykanee, M. K., Gallagher, H. E., Grace, I. M., and Higgins, S. J. (2017). Side-Group-Mediated Mechanical Conductance Switching in Molecular Junctions. *Angewandte Chemie International Edition*, *56*(48), 15378-15382.
7. Al-Galiby, Q. H., Sadeghi, H., Algharagholy, L. A., Grace, I., and Lambert, C. (2016). Tuning the thermoelectric properties of metallo-porphyrins. *Nanoscale*, *8*(4), 2428-2433.

8. Lambert, C.J. and Liu, S.X., 2018. A magic ratio rule for beginners: a chemist's guide to quantum interference in molecules. *Chemistry–A European Journal*, 24(17), pp.4193-4201.

9. Bergfield, J. P., and Stafford, C. A. (2009). Thermoelectric signatures of coherent transport in single-molecule heterojunctions. *Nano letters*, *9*(8), 3072-3076.

10. Reddy, P., Jang, S. Y., Segalman, R. A., and Majumdar, A. (2007). Thermoelectricity in molecular junctions. *Science*, *315*(5818), 1568-1571.

11. Ferrer, J., Lambert, C. J., García-Suárez, V. M., Manrique, D. Z., Visontai, D., Oroszlany, L., and Algharagholy, L. A. (2014). GOLLUM: a next-generation simulation tool for electron, thermal and spin transport. *New Journal of Physics*, *16*(9), 093029.

12. Wang, X., Bennett, T. L., Ismael, A., Wilkinson, L. A., Hamill, J., White, A. J., and Lambert, C. J. (2020). Scale-up of room-temperature constructive quantum interference from single molecules to self-assembled molecular-electronic films. *Journal of the American Chemical Society*, *142*(19), 8555-8560.

13. Ismael, A., Wang, X., Bennett, T. L., Wilkinson, L. A., Robinson, B. J., Long, N. J., and Lambert, C. J. (2020). Tuning the thermoelectrical properties of anthracene-based self-assembled monolayers. *Chemical science*, *11*(26), 6836-6841.

14. Ismael, A., Al-Jobory, A., Wang, X., Alshehab, A., Almutlg, A., Alshammari, M., and Lambert, C. (2020). Molecular-scale thermoelectricity: as simple as 'ABC'. *Nanoscale Advances*, *2*(11), 5329-5334.

15. Wang, X., Ismael, A., Almutlg, A., Alshammari, M., Al-Jobory, A., Alshehab, A., and Lambert, C. (2021). Optimised power harvesting by controlling the pressure applied to molecular junctions. *Chemical Science*.

16. Geng, Y., Sangtarash, S., Huang, C., Sadeghi, H., Fu, Y., Hong, W., and Liu, S. X. (2015). Magic ratios for connectivity-driven electrical conductance of graphene-like molecules. *Journal of the American Chemical Society*, *137*(13), 4469-4476.

17. Yakuphanoglu, F., Okur, S., and Özgener, H. (2009). Modification of metal/semiconductor junctions by self-assembled monolayer organic films. *Microelectronic engineering*, *86*(11), 2358-2363.

Chapter 5

Orientational control of Molecular scale thermoelectricity

This chapter is based on two theoretical studies studying the core asymmetric anthracene molecule and flipping molecule with a finite graphene sheet (Gr). I will explore the following. Firstly, I will study the asymmetric anthracene core with different anchoring groups such as alkynyl -Py, alkynyl -S, and S-Py. Secondly, I studied the asymmetric anthracene linked to the Gr sheet, where we consider flipping these anthracenes in this part. For these two studies, we calculate the wave function and binding energy to predict and investigate the electronic properties. Finally, the thermoelectric properties such as the transmission coefficient $T(E)$ and the Seebeck coefficient S have been calculated by Siesta [1] (Gollum Code) [2].

5.1 Motivation

It is chemically proven that varying the anchor group type of single molecules to external electrodes will control their electrical conductance in a deterministic manner, [3-6]. Synthetic methodologies were used to vary the terminal anchor groups, three different combinations including alkynyl, thiol and pyridine, across aromatic anthracene-based cores. In this work, I present a novel research, where I am able to control the sign of the Seebeck coefficient S by changing the orientation of some asymmetric molecules in regard to the top-Gr sheet (flipping). It is worth mention that, an asymmetric molecule is essential for the flipping process, however, not all asymmetric molecules lead to switching the sign of the Seebeck coefficient S, [5-13]. Thus, I demonstrate that the thermoelectric properties of some asymmetric molecules can be controlled by flipping these molecules with regard to a graphene sheet.

It is well-known, that the S controls the conversion of a temperature gradient to a voltage differential. Due to limit global sources, common inorganic thermoelectric materials such as Co, Ni, Bi, Sb, and Pb are toxic and costly. As a result, various techniques for using the thermoelectric properties of nanostructured organic materials or organic molecules have been suggested in recent years.

5.2 Studied Molecules

This work is a continuous investigation about anthracene-based molecules that have been studied in chapter 4. In this chapter, the transport properties of asymmetric anthracene-based molecules have been explored [7-10]. Three structures of asymmetric anthracene-based built from figure 5.1. These structures are fully relaxed as described in section 4.2 of chapter 4, and known as follows, **1**: anthracene-based molecule with two different anchors including alkynyl and Py (alkynyl -Py), **2**: anthracene-based with alkynyl and thiol (alkynyl-thiol), **3**: anthracene-based with thiol and Py (thiol-Py), and a graphene sheet (Gr). The three asymmetric anthracene-based molecules combine with Gr and placed between Au electrodes to study the flipping feature as I will discuss later. Notice: I have used finite graphene sheet. it has been terminated as Zigzag shape in z-direction or transport direction with dimensions (18.7 Å, 20.3 Å).

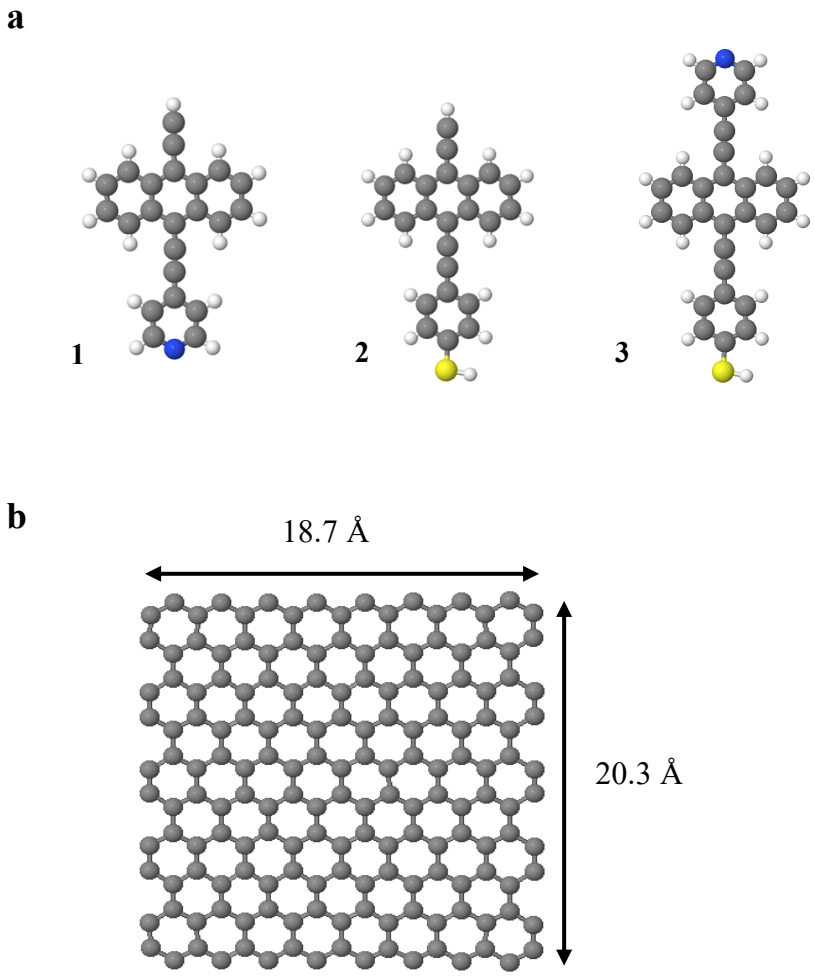

Figure 5.1: a: Three asymmetric anthracene-based molecules; **1**: alkynyl -Py anchor, **2**: alkynyl - thiol anchor, and **3**: Py-thiol anchor. **b:** Graphene sheet (Gr.)

5.3 Frontier orbitals of the molecules.

To have a good understanding of electronic properties**,** the frontier orbital of studied molecules: highest occupied molecular orbitals (HOMO) and lowest unoccupied orbitals (LUMO), in addition to (HOMO+1), and (LUMO-1), along with their energies are investigated. I investigate three asymmetric anthracene core molecules including (alkynyl -Py), (alkynyl - thiol), and (Py-thiol) anchor groups, as shown in Figure 5.2-5.4. The red and blue colours represent the positive and negative orbital amplitude. According to the product rule [11], one

can predict whether a molecule possesses a high or low conductance based on the colours on the HOMO and LUMO, as it discussed in previous chapter (see section 4.3).

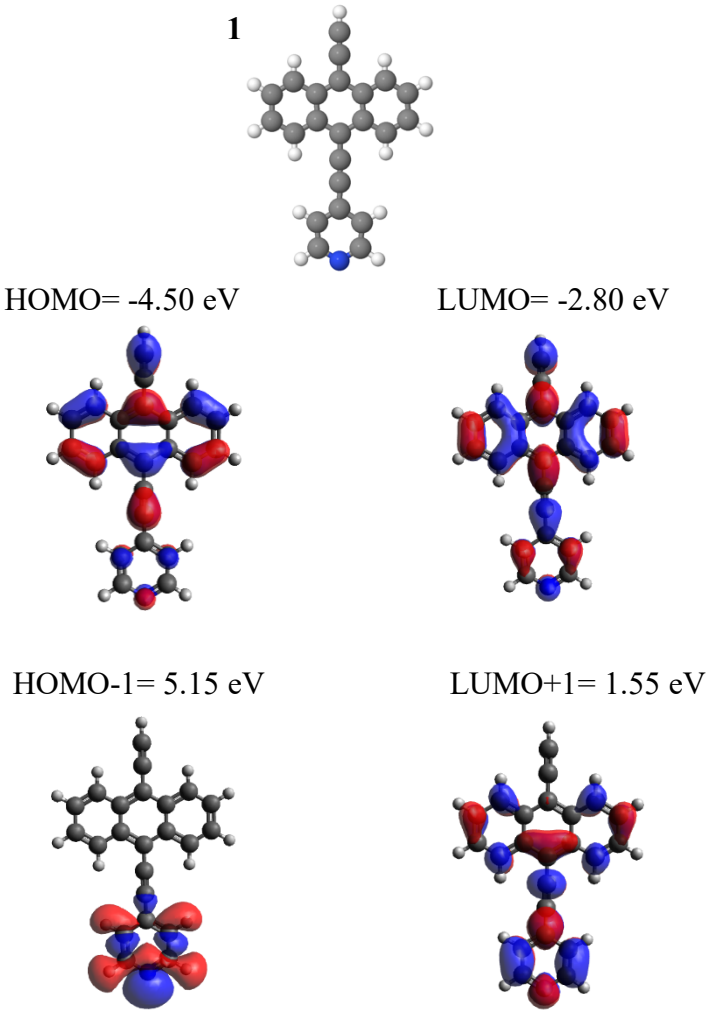

Figure 5.2: Wave function for **1. Top panel**: fully optimised geometry of **1**. **Lower panel**: HOMO, LUMO, HOMO-1, LUMO+1 of molecule **1** along with their energies.

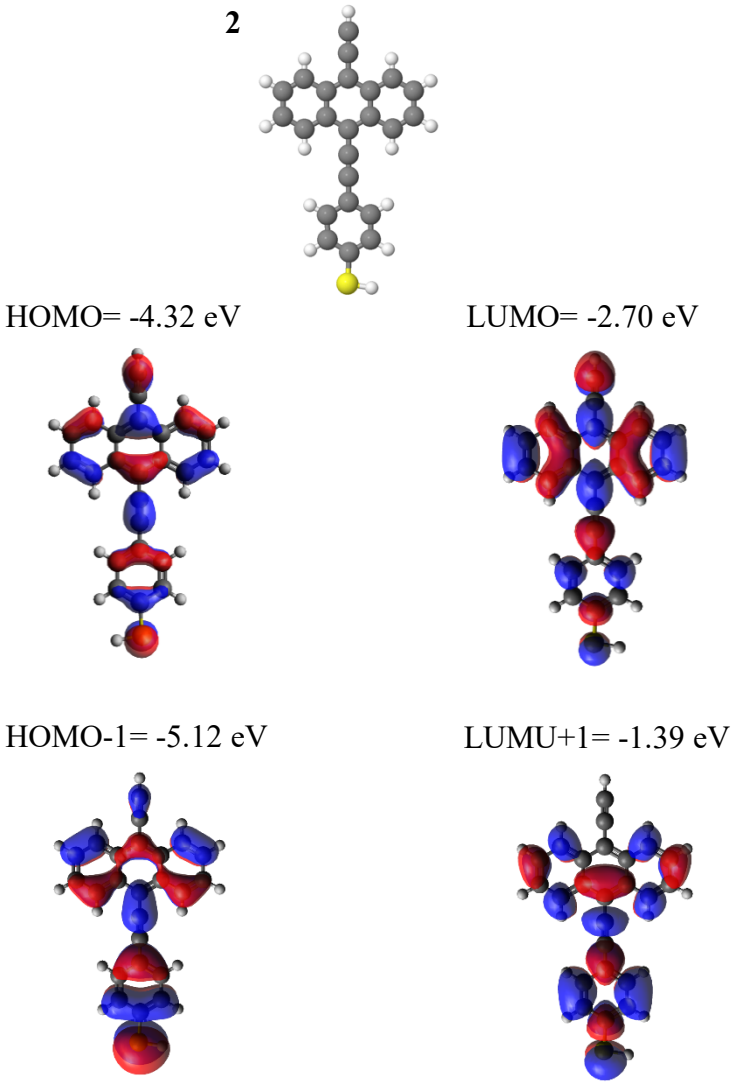

Figure 5.3.: Wave function for **2**. **Top panel**: fully optimised geometry of **2**. **Lower panel**: HOMO, LUMO, HOMO-1, LUMO+1 of molecule **2** along with their energies.

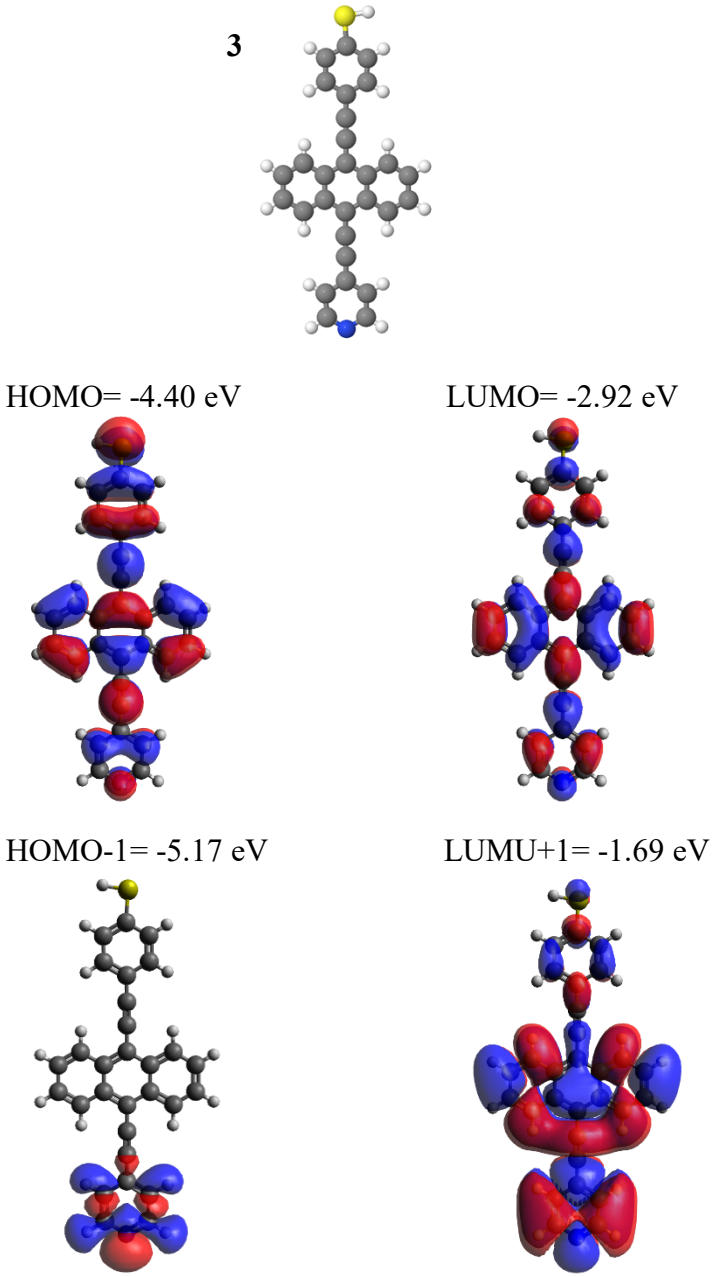

Figure 5.4: Wave function for **3**. **Top panel**: fully optimised geometry of **3**. **Lower panel**: HOMO, LUMO, HOMO-1, LUMO+1 of molecule **3** along with their energies.

5.4 Binding Energies

This section uses a combination of DFT and the counterpoise method, as it described in section 4.3 of chapter 4. Briefly, it removes the basis set superposition errors to calculate the optimum binding distance of two objects [12-13].

5.4.1 Binding Energy of Anthracene Core to Gold electrode:

Here, I calculated the binding energy of the three molecules (Fig. 5.1) on gold electrodes where asymmetric anthracene core linked to Au lead. These asymmetric anthracene cores have different anchor groups including: Py, thiol, and alkynyl, as shown in Figures (5.5-5.7).

Figure 5.5 shows that the optimum binding distance $d_{Anch.}$ between the Py anchor group and the Au to be 2.3 Å, and at approximately -0.4 eV. Similarly, Figure 5.6 represents the binding energy between the thiol anchor group and the gold lead and $d_{Anch.}$ is 2.4 Å, at approximately -1.2 eV. This suggests the binding energy of the thiol anchor group is much stronger than that the Py anchor to Au electrode (this result is in agreement with the literature review). Finally, the alkynyl's binding energy lies between the thiol and Py, however, it is more towards the stronger binding energy (i.e. thiol) to Au with binding energy of -1 eV at d_1= 2.3 Å, as shown in the Figure 5.7. These calculations suggest that both thiol and alkynyl bind to Au substrate approximately 3 times stronger than that Py with 2.3 Å separation distance as shown in Table 5.1, (Note the optimum distance between the Au and Anchor labelled $d_{Anch.}$).

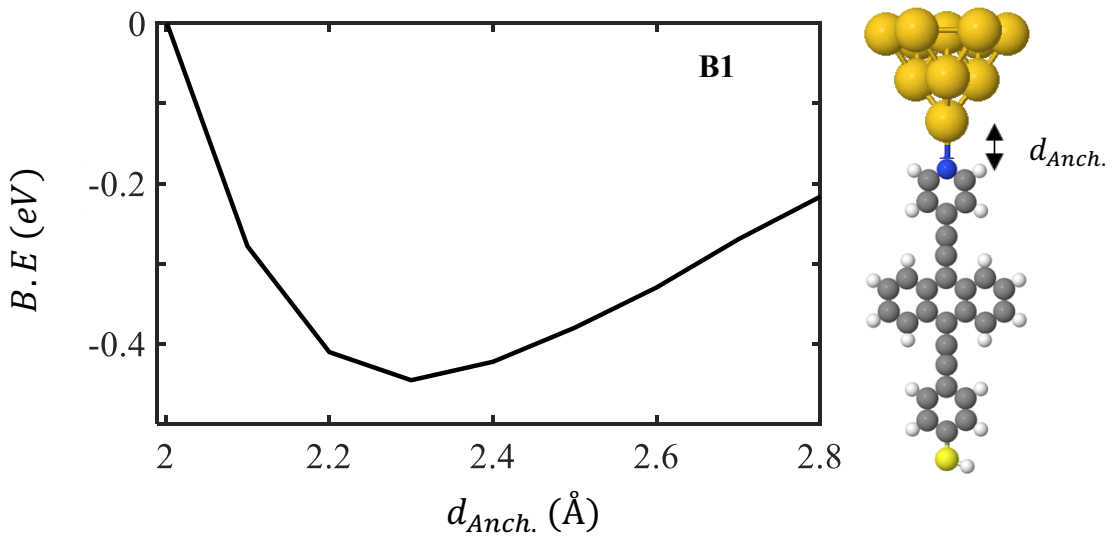

Figure 5.5: Right: An asymmetric anthracene-based molecule configuration with thiol and Py anchors at the Au lead interface. **Left:** Binding energy as a function of the optimum binding distance $d_{Anch.}$ between the gold electrode and an asymmetric anthracene core. This distance is found to be 2.3 Å, at approximately 0.4 eV.

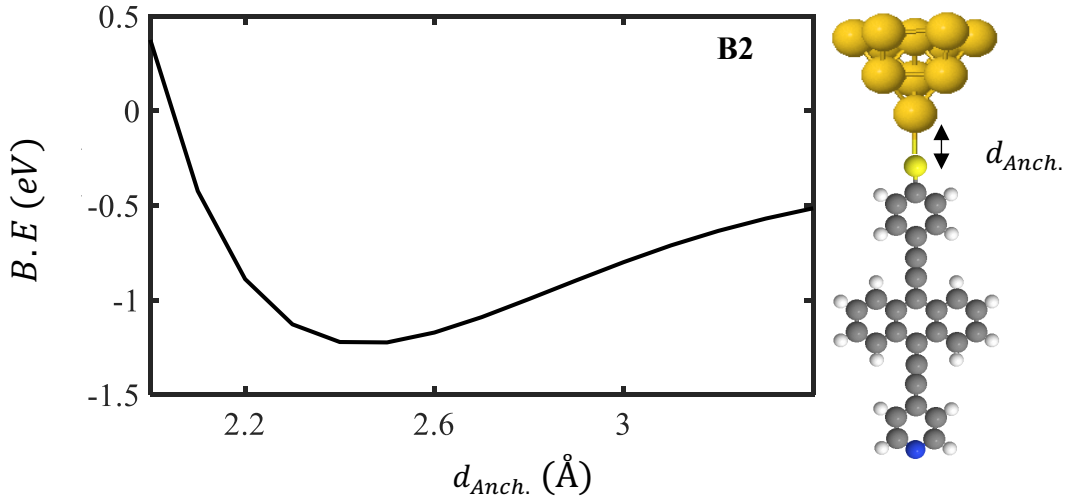

Figure 5.6: Right: An asymmetric anthracene-based molecule configuration with Py and thiol anchors. **Left:** Binding energy as a function of the optimum binding distance $d_{Anch.}$ between the gold electrode and an asymmetric anthracene core. This distance is found to be 2.4 Å, at approximately 1.2 eV.

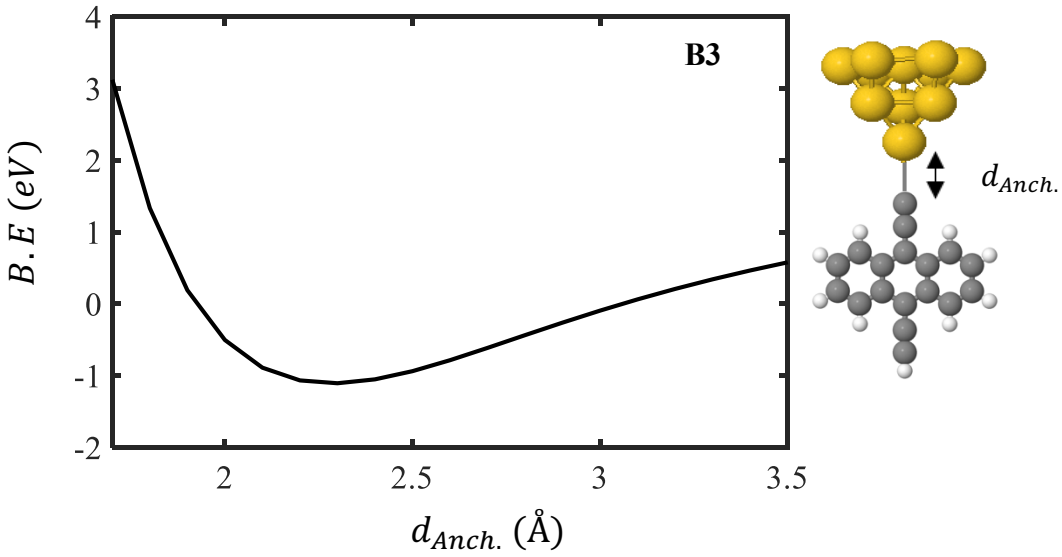

Figure 5.7: Right: An asymmetric anthracene-based molecule configuration with 2 alkynyl anchors. **Left:** Binding energy as a function of the optimum binding distance $d_{Anch.}$ between the gold electrode and an asymmetric anthracene core. This distance is found to be 2.3 Å, at approximately 1.0 eV.

Table 5.1: Summarises the binding energy (B.E), and optimum distance ($d_{Anch.}$), calculations for three different anchor groups bind to gold electrode.

	Au-anchor bound		
	B1 (Au-Py)	B2 (Au-thiol)	B3 (Au-alkynyl)
B.E (eV)	-0.4	-1.2	-1.0
$d_{Anch.}$(Å)	2.3	2.4	2.2

5.4.2 Binding Energy of Anthracene Core to Graphene sheet:

Here, another three binding energies have been calculated where, I demonstrate how an asymmetric anthracene-based molecule of different anchor groups binds to a graphene sheet. Thus, I calculate the binding energy as a function of the optimum binding distance of a Gr sheet to Py or alkynyl or thiol anchor group.

The binding energy between a Gr sheet and pyridine anchor is shown in Figure 5.8, where the right panel shows an asymmetric anthracene molecule linked to a graphene sheet (Gr-Py). The left panel represents the binding energy plot as a function of the optimum binding distance $d_{Flip.}$. In this case, $d_{Flip.}$ is found to be 3Å, and the B.E is approximately -0.14 eV. (Note the optimum distance between the graphene sheet and anchor labelled$d_{Flip.}$).

Next, I connect the Gr sheet with an asymmetric anthracene Gr-thiol, this time, and I calculate the binding energy, as shown in Figure 5.9. The right panel represents an asymmetric anthracene molecule linked to a graphene sheet (Gr-thiol). The left panel shows the binding

energy as a function of the optimum distance $d_{Flip.}$ and $d_{Flip.}$ is 3Å, with B.E approximately -0.22 eV.

Finally, I attach the G sheet to an asymmetric anthracene (Gr- alkynyl), as shown in Figure 5.10. The right panel is an asymmetric anthracene molecule linked to a G sheet (Gr- alkynyl). In the left panel, $d_{Flip.}$ is found to be 1.4Å, and the B.E approximately -0.44 eV.

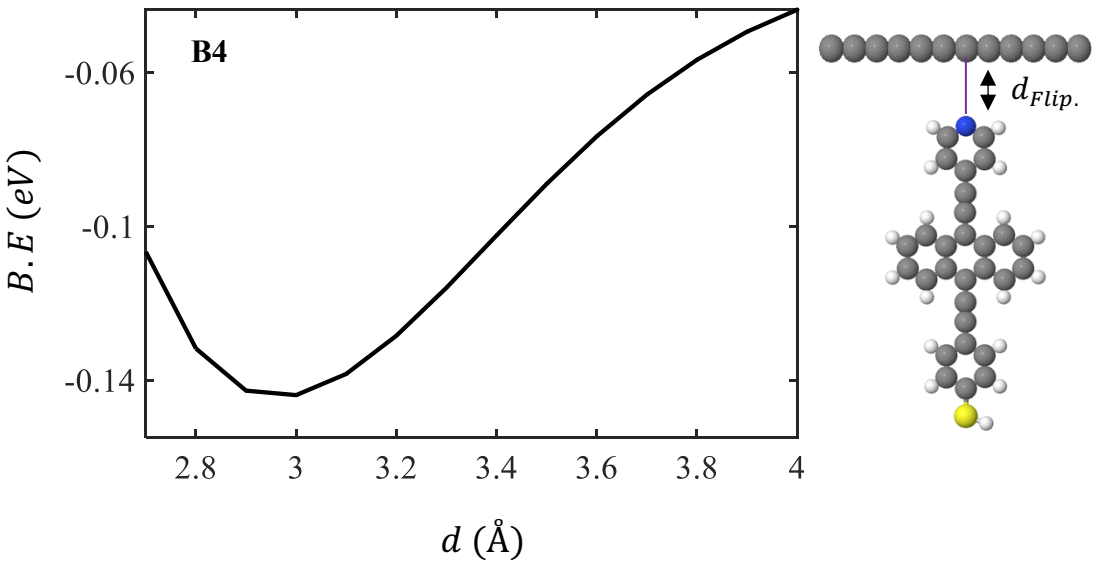

Figure 5.8: Right: An asymmetric anthracene-based molecule configuration with thiol and Py anchors at the Gr interface. **Left:** Binding energy as a function of the optimum binding distance $d_{Flip.}$ (Py-Gr). This distance is found to be 3.0 Å, at approximately 0.14 eV.

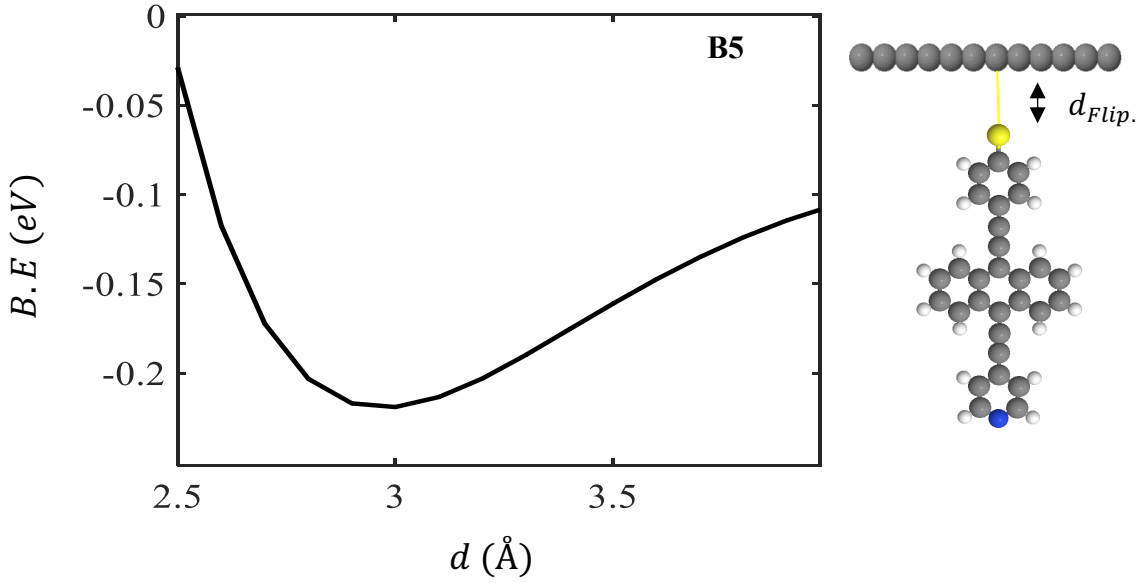

Figure 5.9: Right: An asymmetric anthracene-based molecule configuration with Py and thiol anchors at the Gr interface. **Left:** Binding energy as a function of the optimum binding distance $d_{Flip.}$(thiol-Gr). This distance is found to be 3.0 Å, at approximately 0.22 eV.

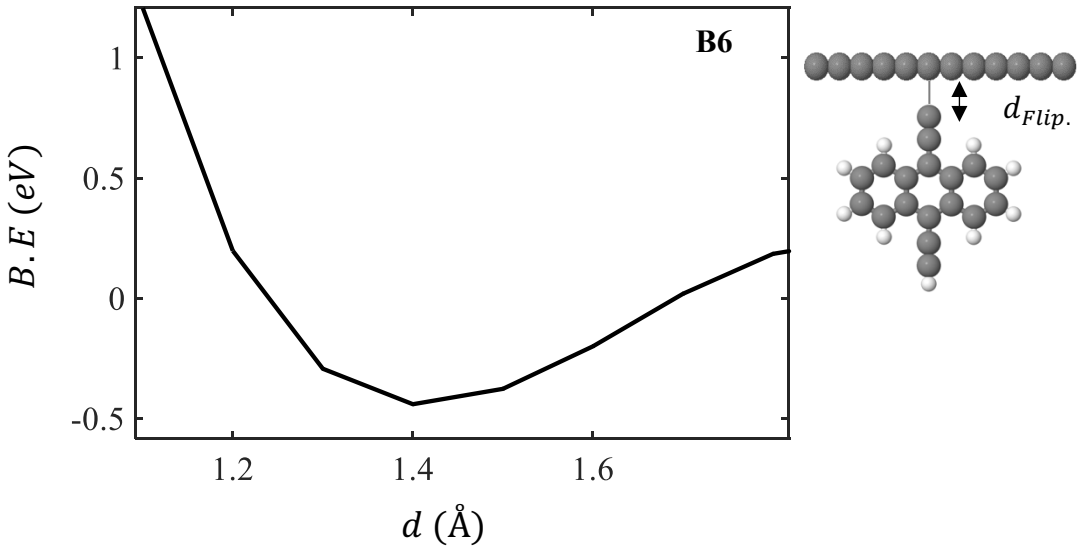

Figure 5.10: Right: An asymmetric anthracene-based molecule configuration with 2 alkynyl anchors at the Gr interface. **Left:** Binding energy as a function of the optimum binding distance $d_{Flip.}$(TMS-Gr). This distance is found to be 1.4 Å, at approximately 0.44 eV.

Figures 5.8-5.10 results suggest that the alkynyl anchor binds to Gr sheet 2 times stronger than that thiol and with reducing the separation distance $d_{Flip.}$ to a half, whereas the B.E reduces to a half for the pyridyl anchor at the same distance, $d_{Flip.}$ =3.0 Å as shown in Table 5.2.

Table 5.2: Summarises the binding energy (B.E), and optimum distance ($d_{Flip.}$), calculations for three different anchor groups bind to Gr.

	Gr-anchor bound		
	B4 (Py-Gr)	B5 (thiol-Gr)	B6 (alkynyl - Gr)
B.E (eV)	-0.14	-0.22	-0.44
$d_{Flip.}$ (Å)	3.0	3.0	1.4

Table 5.4: Summarises all the binding energies (B.E), and optimum distances ($d_{Anch.} and\ d_{Flip.}$), calculations for three different anchor groups bind to Au or Gr.

	(Au)-anchor bounds	
	$d_{Anch.}$ and $d_{Flip.}$ (Å)	B.E (eV)
B1	2.3	-0.4
B2	2.4	-1.2
B3	3.0	-1.0
B4	3.0	-0.14
B5	3.0	-0.22
B6	1.4	-0.44

5.5 Investigating Three Asymmetric Anthracene-based Cores

In this section, I explore three different asymmetric anthracene-based molecules with different anchor groups including: alkynyl, Py and thiol. The electronic properties of these molecules have been investigated. I firstly, calculate the wave functions to assist the prediction whether these molecules possess a high or low conductance based on the QI, through the product rule as discussed in chapter 4. Then the binding energy to find the optimum distance between the Au and anchors, so that I can calculate the transport properties such as the transmission coefficient $T(E)$ and Seebeck coefficient S . Wave functions and biding energies have been already discussed in sections 4.3 and 5.3, I shall begin with the $T(E)$.

5.6 Transmission coefficient $T(E)$

This section aims to study the transmission function of asymmetric anthracene-based cores with different anchor groups such as alkynyl, Py, and thiol, for this purpose I investigate three cases:

Case 1: Anthracene-based of alkynyl -Py anchoring groups:

Anthracene with two different anchors including alkynyl and Py, has been studied as shown in Figure 5.11. If the two anchors were pyridine, one would expect this molecule to be a LUMO-dominated due to the presence of the pyridyl anchor. However, it seems the case is still true even if the molecule is an asymmetric, means two different anchors. I think this is due to that Py anchor overcomes alkynyl even though that the binding energy of alkynyl is stronger than that Py (see Table 5.1). It is worth mentioning, that alkynyl is a HOMO-dominated anchor and that is clearly shown in Figure 5.11, where the alkynyl pulls the DFT-predicted Fermi energy ($E-E_F^{DFT}=0$ eV) slightly away from LUMO resonance, as the pyridyl anchor is pinning $E-E_F^{DFT}=0$ right at the LUMO resonance.

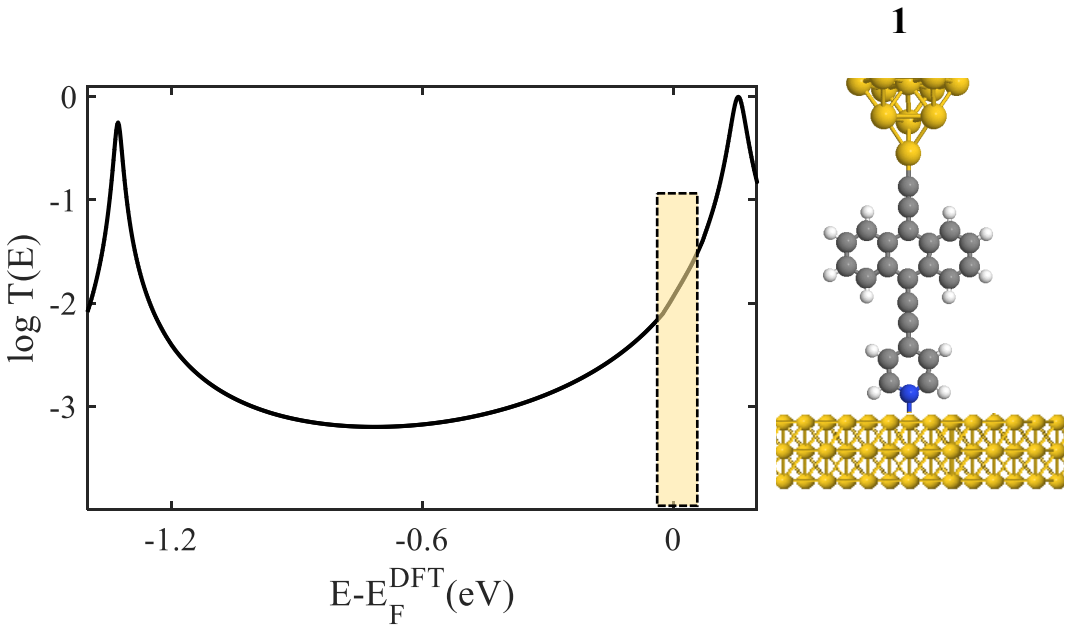

Figure 5.11: Right panel: Schematic illustrations of an asymmetric molecular junction for **1.** **Left panel:** Zero-bias transmission coefficient $T(E)$ of molecule **1** against electron energy E, an example of a LUMO-dominated curve of asymmetric molecule.

Case 2: Anthracene-based of alkynyl -thiol anchoring groups:

In this case, I consider anthracene with two different anchors including alkynyl and thiol anchors. Figure 5.12 shows that this molecule is a HOMO-dominated and that is what one would expect due to the fact that the both anchors (alkynyl and thiol), are HOMO-dominated. $E\text{-}E_F^{DFT}=0$ sits so close to the HOMO resonance because both anchors are pinning in the same direction toward HOMO resonance.

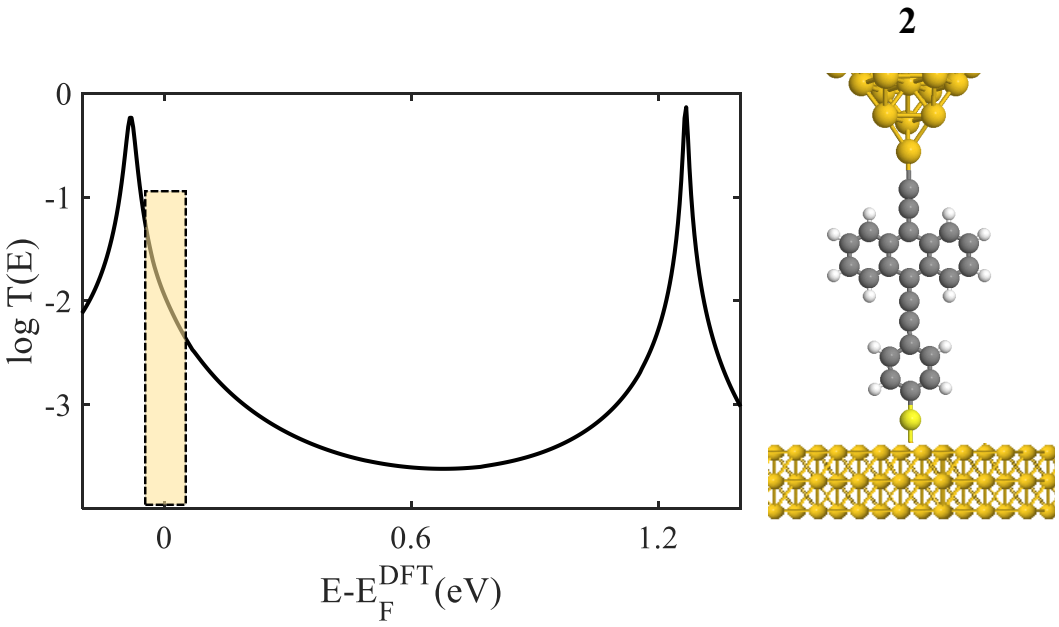

Figure 5.12: Right panel: Schematic illustrations of an asymmetric molecular junction for **2.** **Left panel:** Zero-bias transmission coefficient $T(E)$ of molecule **2** against electron energy E, an example of a HOMO-dominated curve of asymmetric molecule.

Case 3: Anthracene-based of Py-thiol anchoring groups:

Case 3 is an asymmetric anthracene with two different anchors including thiol and Py, as shown in Figure 5.13. As the two anchors well-known to pin down in an opposite direction, in other words, HOMO- or LUMO-dominated. Furthermore, both anchors are strong so one would expect this molecule to possess a mid-gap Fermi energy ($E\text{-}E_F^{DFT}$=0 eV), rather than being HOMO- or LUMO-dominated. Figure 5.13, proves this prediction to be accurate as clearly shown that $E\text{-}E_F^{DFT}$=0 eV sits in mid-way between the HOMO and LUMO resonances.

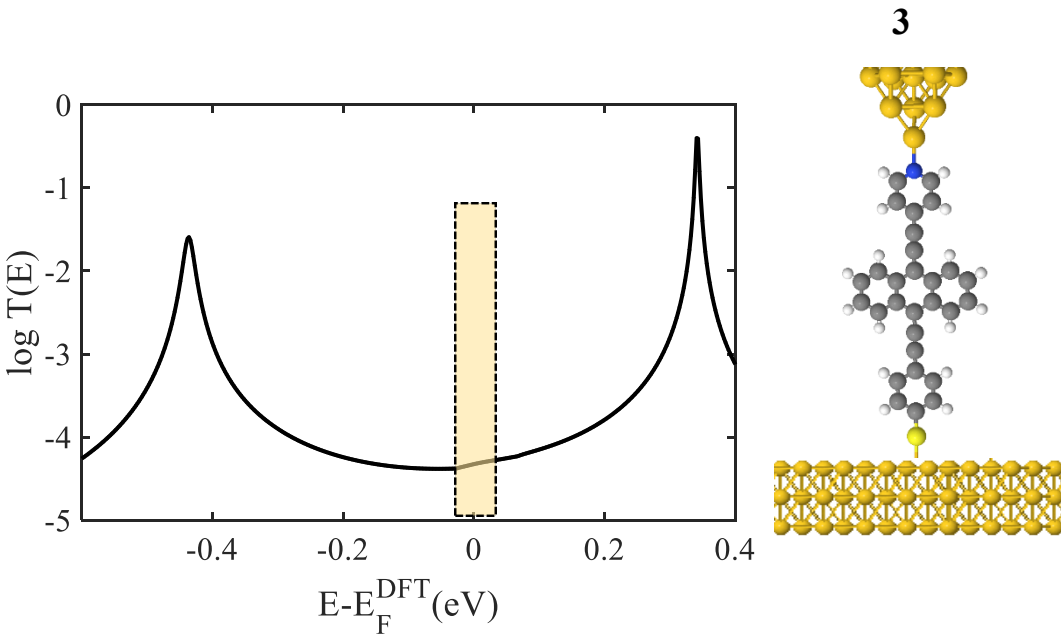

Figure 5.13: Right panel: Schematic illustrations of an asymmetric molecular junction for **3.** **Left panel:** Zero-bias transmission coefficient $T(E)$ of molecule **3** against electron energy E, an example of a HOMO or LUMO-dominated curve of asymmetric molecule.

Actual conductance values of the three asymmetric anthracene-based molecules are shown in table 5.5. It also contains some extra information about these junctions such as HOMO-LUMO gaps, molecular length, G and total binding energy of asymmetric molecules.

Table 5.5: HOMO-LUMO gap of isolated molecules and in junctions, molecular length, conductance and total binding energy.

E_F Molecule	Log (G/G_0)	E_g, DFT (Isolated Mo.)	E_g, DFT (Au/M/Au)	Length (Å)	Total B.E (eV)
1	-7.3	1.70 eV	1.41 eV	12.3	Au-C= -1 Au-N=-0.4 Total= -1.4
2	-7.7	1.62 eV	1.28 eV	14.0	Au-C=-1 Au-S=-1.2 Total=-2.2
3	-8.4	1.50 eV	0.70 eV	18.27	Au-S=-1.2 Au-N=-0.4 Total=-1.6

5.7 Seebeck coefficient *S*

The Seebeck coefficient of the three cases above, calculates using equatins 4.6 as discussed in chapter 4, the three cases.

Case 1: Anthracene of alkynyl -Py anchoring groups.

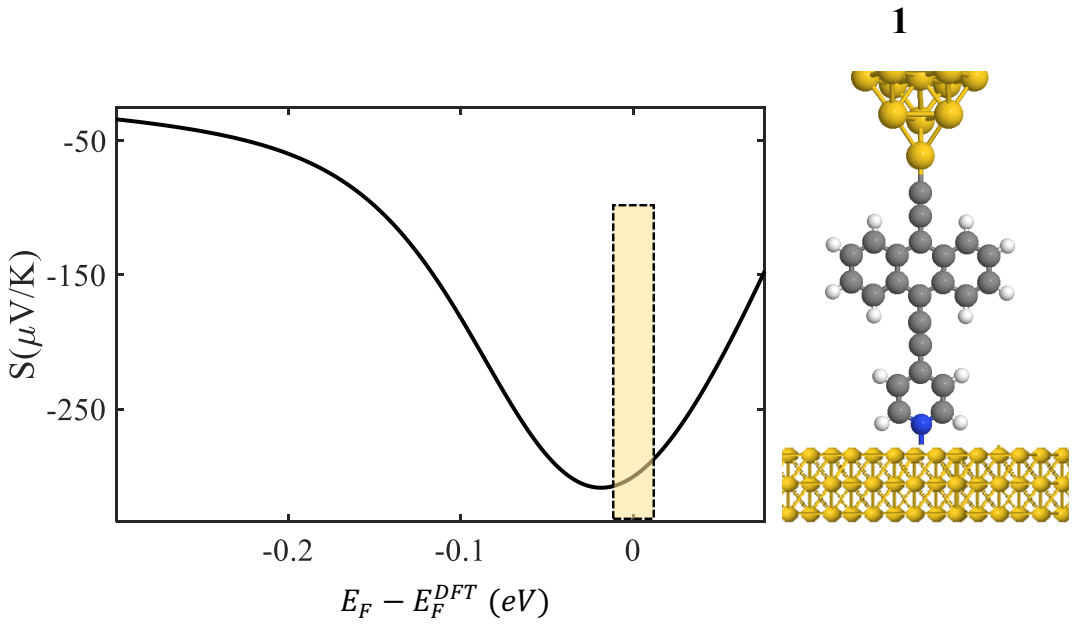

Figure 5.14: Right panel: Schematic illustrations of molecular junction of **1. Left panel:** Seebeck coefficient *S* of molecule **1** against electron energy E.

Case 2: Anthracene of alkynyl -thiol anchoring groups.

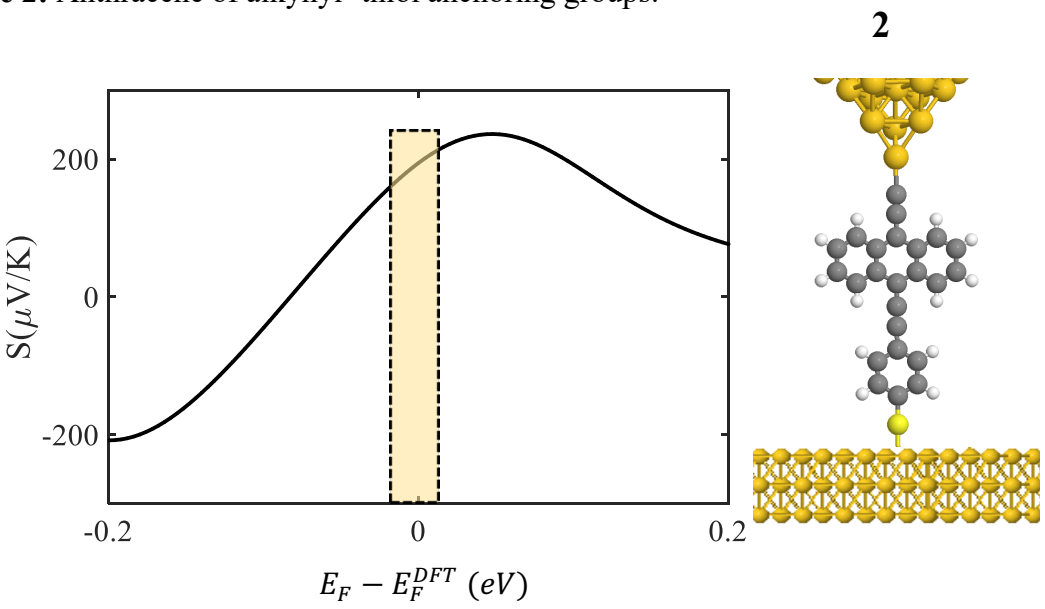

Figure 5.15: Right panel: Schematic illustrations of molecular junction for **2. Left panel:** Seebeck coefficient *S* of molecule **2** against electron energy E.

Case 3: Anthracene of Py-thiol anchoring groups.

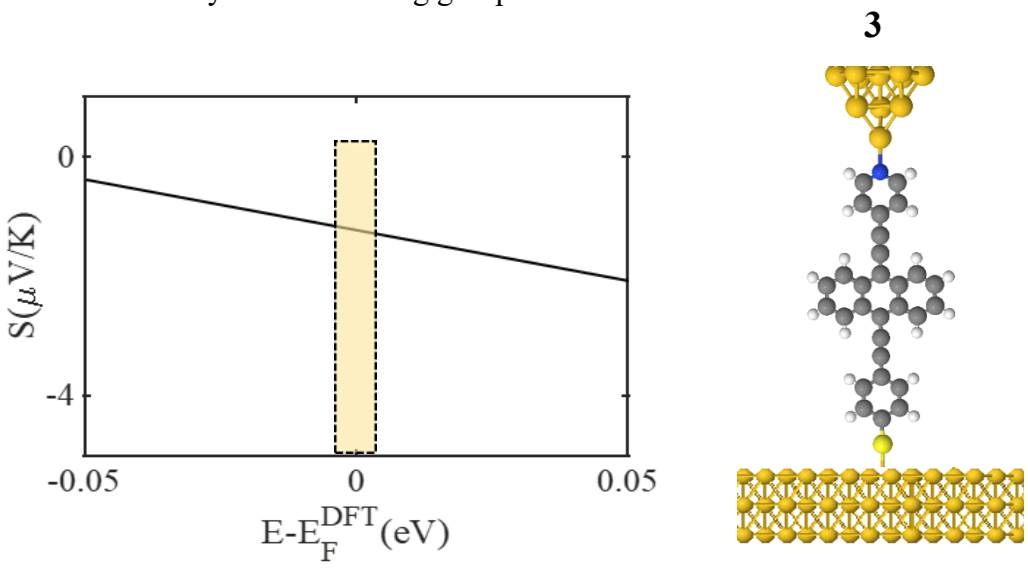

Figure 5.16: Right panel: Schematic illustrations of molecular junction for **3**. **Left panel:** Seebeck coefficient *S* of molecule **3** against electron energy E.

As it discussed in chapter 4, the slope of the transmission coefficient $T(E)$ determines the sign and magnitude of the Seebeck coefficient S. In other words, whether the curve is HOMO or LUMO dominated. Figure 5.14, shows a negative Seebeck coefficient at DFT-predicted Fermi $E\text{-}E_F^{DFT}$=0 eV and this is due to the fact that this molecule is a LUMO-dominated as shown in Figure 5.11 (anthracene of alkynyl -Py anchors). In contrast, Figure 5.15 shows a positive S at $E\text{-}E_F^{DFT}$=0 eV and this is because it is a HOMO-dominated molecule as shown in Figure 5.12 (anthracene of alkynyl -Thiol anchors). Figure 5.16 shows a negative S at $E\text{-}E_F^{DFT}$=0 eV and this is again because it is a LUMO-dominated molecule as shown in Figure 5.12 (anthracene of alkynyl -Thiol anchors).

5.8 Quantum oscillation in asymmetric multicomponent.

In this section, I aim to study the oscillation in conductance for asymmetric anthracene, with different anchors including alkynyl, Py and thiol, linked to *finite Gr sheet* (multicomponent). Firstly, I combine the Gr sheet with the asymmetric anthracene to form the multicomponent, then place the multicomponent between Au electrodes. The Au tip and the anchor of the molecule are aligned in a way that passes through a carbon atom of the Gr sheet as shown in Figure (5.17-a). Secondly, I repeat the first step but in different positions (i.e. **1, 2, 3** and **4**) as shown in Figure 5.17-b. Finally, I determine the transmissions coefficient $T(E)$, in 4 different alignment locations as shown in Figure (5.17-a and -b).

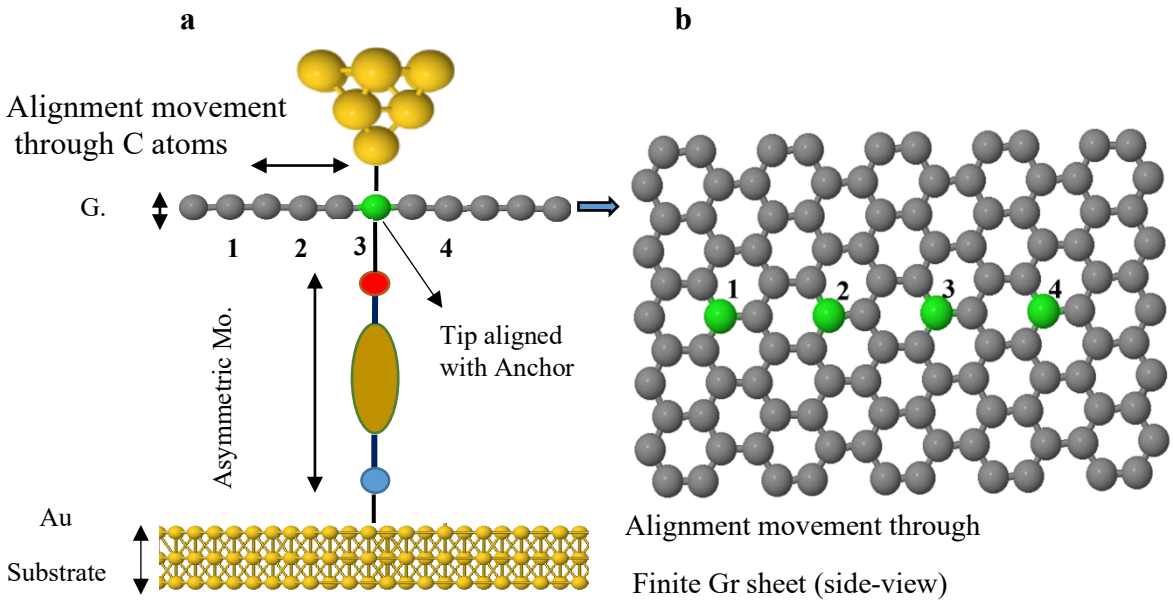

Figure 5.17: Representation of multicomponent junction; **a**: An asymmetric molecule attached to Gr sheet (multicomponent), placed between Au electrodes, **b**: Side-view shows the alignment movement through the graphene sheet (Gr).

To keep the tip and the molecule aligned to each other via the anchor group, I pull only the graphene sheet in different positions. In these pulling positions there is always a carbon atom aligned with the tip and anchor, means tip, C atom and anchor are all aligned. For the oscillation calculations, I investigate three cases, where three different asymmetric anthracene molecules are employed and combine with Gr sheet to form multicomponent and as follows:

Case 1: Multicomponent alkynyl -Gr

Here, the oscillation of asymmetric anthracene of alkynyl and Py groups has been studied in four positions **1**, **2**, **3** and **4**. In these calculations, I move only the Gr sheet, while the whole junction is kept stationary as shown in Figure 5.18-a. The $T(E)$ curves (black, green, red and blue) are determined for **1**, **2**, **3** and **4** positions respectively as shown in Figure 5.18-b. These calculations show that the alkynyl -Gr multicomponent is a LUMO-dominated and the reason for that is the presence of the pyridyl anchor that binds to Au electrode at the other end. alkynyl -Gr multicomponent presents a uniform oscillation with a ratio of approximately 0.4, at DFT-predicted Fermi energy ($E\text{-}E_F^{DFT}$=0 eV), as shown in Figure 5.18-**c**. It also shows, that the odd positions **1**, **3** yield a high conductance while the even positions **2**, **4** have a low conductance.

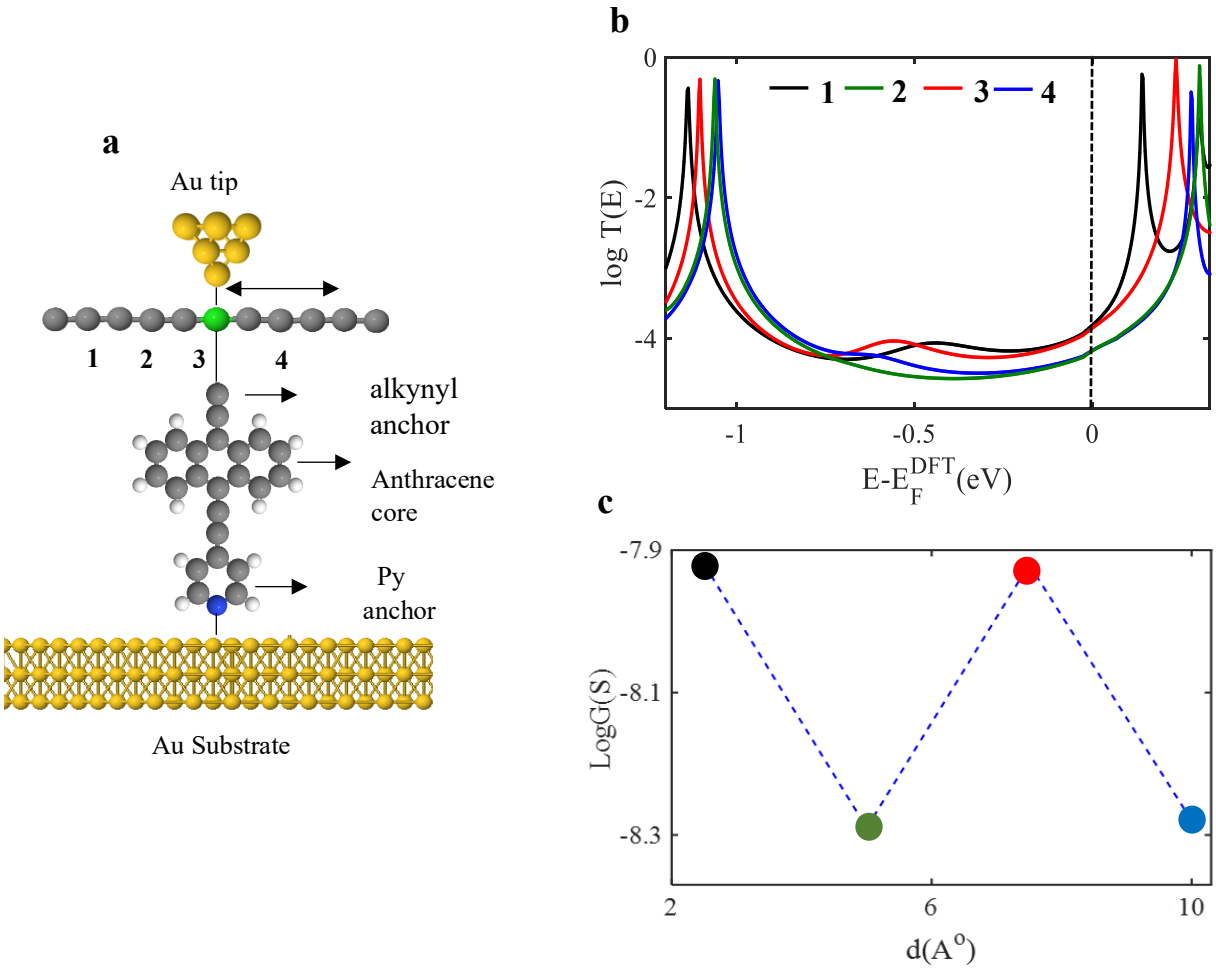

Figure 5.18: a: Representation of alkynyl -Gr multicomponent junction in four positions; **b**: Transmission coefficient curves against electron energy E for **1**, **2**, **3** positions and **4**.**c**: Conductance versus the pulling distance on the carbon atoms in the Gr sheet (black and red odd while green and blue even positions).

Case 2: Multicomponent Thiol-Gr

Multicomponent of asymmetric anthracene of alkynyl and thiol anchor groups attach to Gr sheet is shown in Figure 5.19-**a**. $T(E)$ curves of this case have been calculated in the four positions **1, 2, 3** and **4 (**black, green, red and blue), respectively. These calculations show that the Multicomponent-thiol is a HOMO-dominated at the DFT-predicted Fermi energy (E-E_F^{DFT}=0 eV). This is because the alkynyl that binds to Au (at the other end), is a HOMO-dominated anchor as clearly shown in Figure 5.19-b. In this case the oscillation is less uniform and again the odd positions **1, 3** have higher conductance than that the even positions **2, 4**. The oscillation ratio is 0.34, (average is taken for the odd and even values).

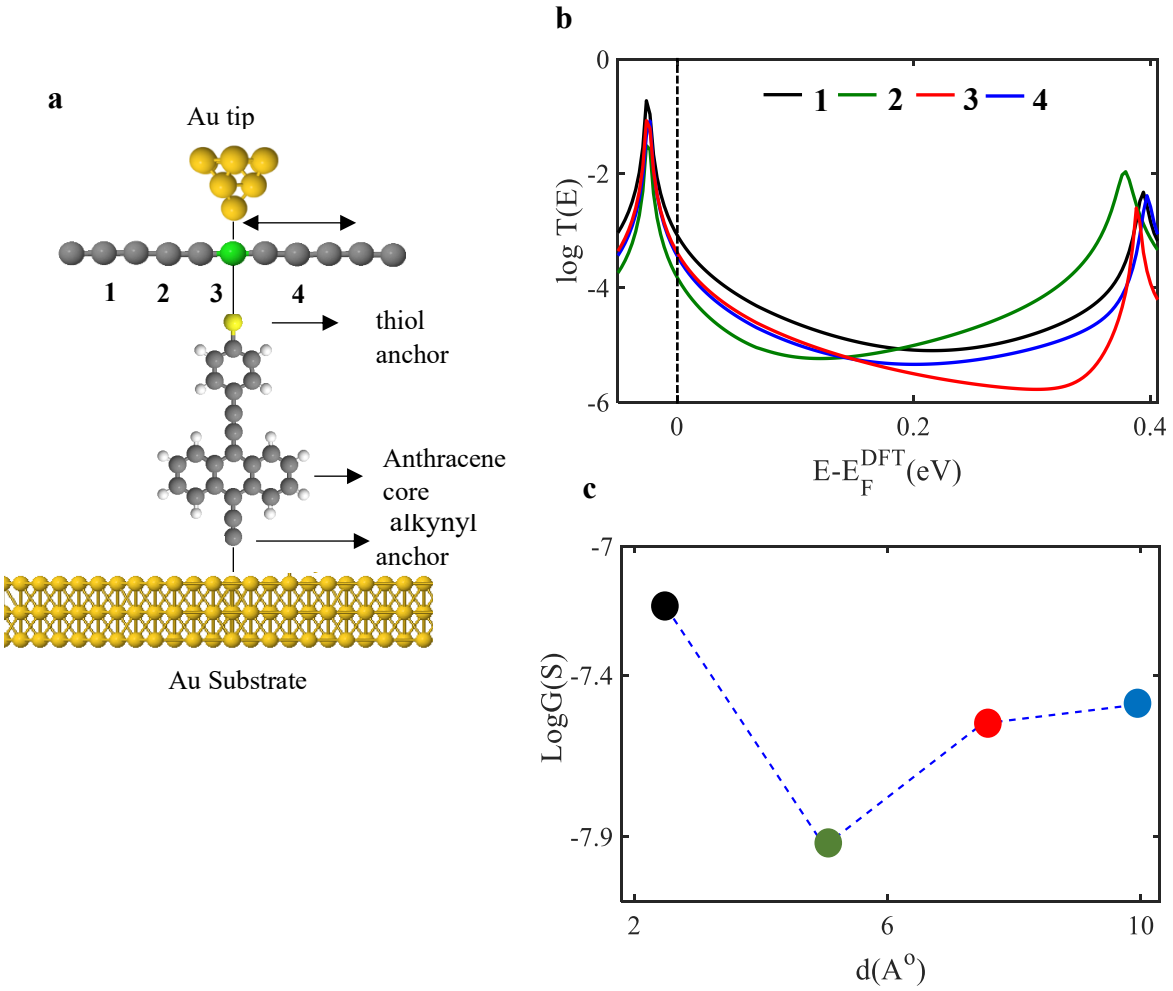

Figure 5.19: a: Representation of thiol-Gr multicomponent junction in four positions; **b**: Transmission coefficient curves against electron energy E for **1**, **2**, **3** positions and **4**.**c**: Conductance versus the pulling distance on the carbon atoms in the Gr sheet (black and red odd while green and blue even positions).

Case 3: Multicomponent pyridyl-Gr

For this case, I consider a multicomponent of asymmetric anthracene of Py and thiol groups as shown in Figure 5.20-**a**. The $T(E)$ curves calculate for **1, 2, 3** and **4** positions (black, green, red and blue curve, respectively). These calculations suggest that this case is a LUMO-dominated at $E\text{-}E_F^{DFT}=0$ eV, as shown in Figure 5.20-b. This multicomponent is a LUMO-dominated

because of the present of thiol anchor that binds to the Au electrode at the other end of the junction. The oscillation in this case again is less uniform and the oscillation ratio is larger than that other two cases by 0.2 (i.e. 0.6).

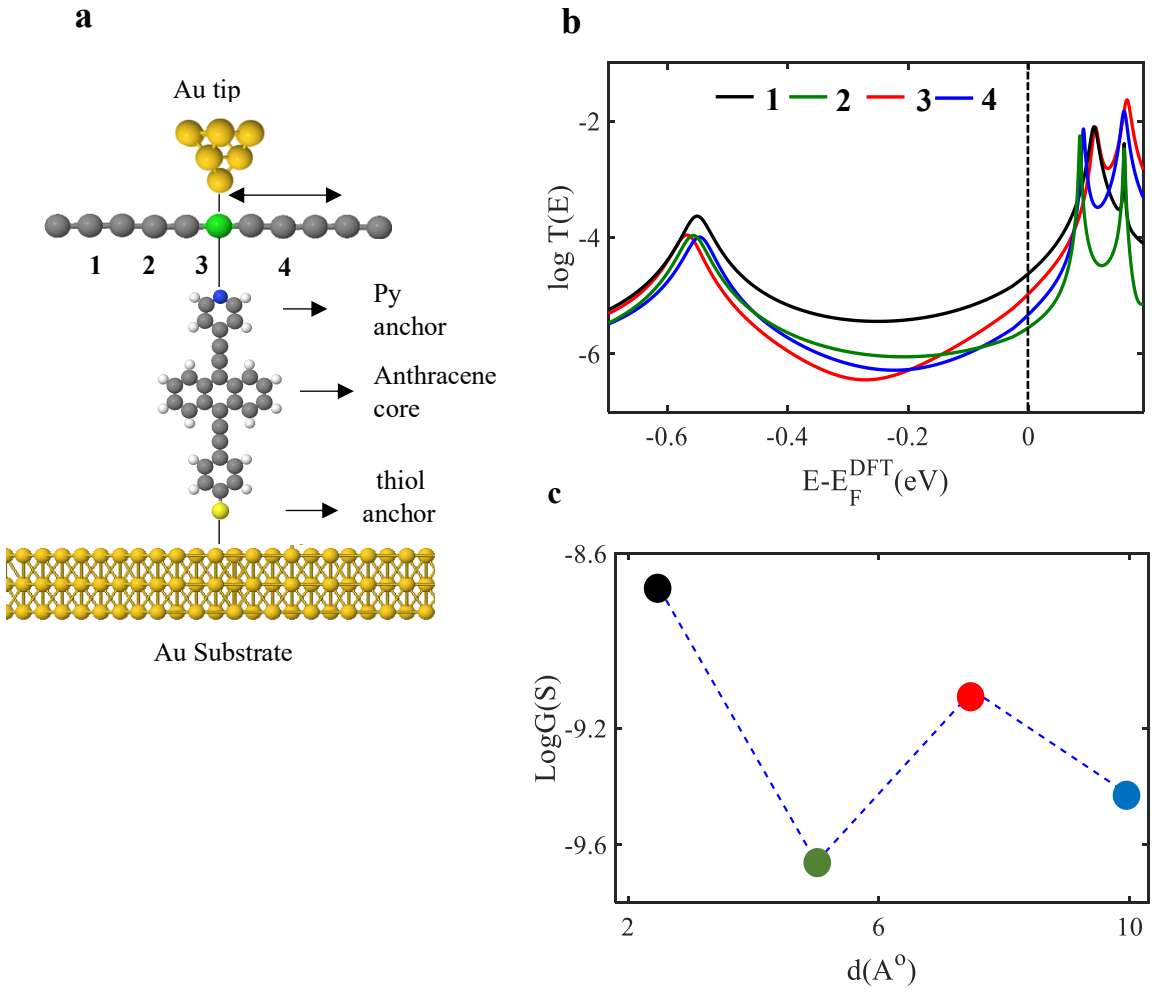

Figure 5.20: a: Representation of Py-Gr multicomponent junction in four positions; **b**: Transmission coefficient curves against electron energy *E* for **1**, **2**, **3** positions and **4**.**c**: Conductance versus the pulling distance on the carbon atoms in the Gr sheet (black and red odd while green and blue even positions).

5.9 Flipping characteristic

After studying the oscillation behaviour in three cases of asymmetric anthracene-based molecules including alkynyl-Py, alkynyl -thiol, and Py-thiol anchor groups attached to Gr sheet in several locations to form multicomponent. In this section, I am going to employ the same 3 multicomponent discussed in section 5.8. In the present research, the Gr sheet is stationary while the asymmetric molecule flips between the Au and Gr sheet.

Figure 5.21 illustrates the components that use to build the flipping junction. It also shows molecule where it consists of spacers and two different anchors groups (blue and red). Then adding a Gr sheet to form the multicomponent compound. Finally, this structure places between two gold electrodes. To achieve the flipping feature, firstly, I link anchor-2 to the Gr sheet and then place this structure between the Au electrodes, (Figure 5.22-a). Secondly, I flip the molecule where anchor-1 is now attached to the Gr sheet, and again place the multicomponent between electrodes (Figure 5.22-b). Thus, I have two case labelled **a** and **b** as showing in the following section.

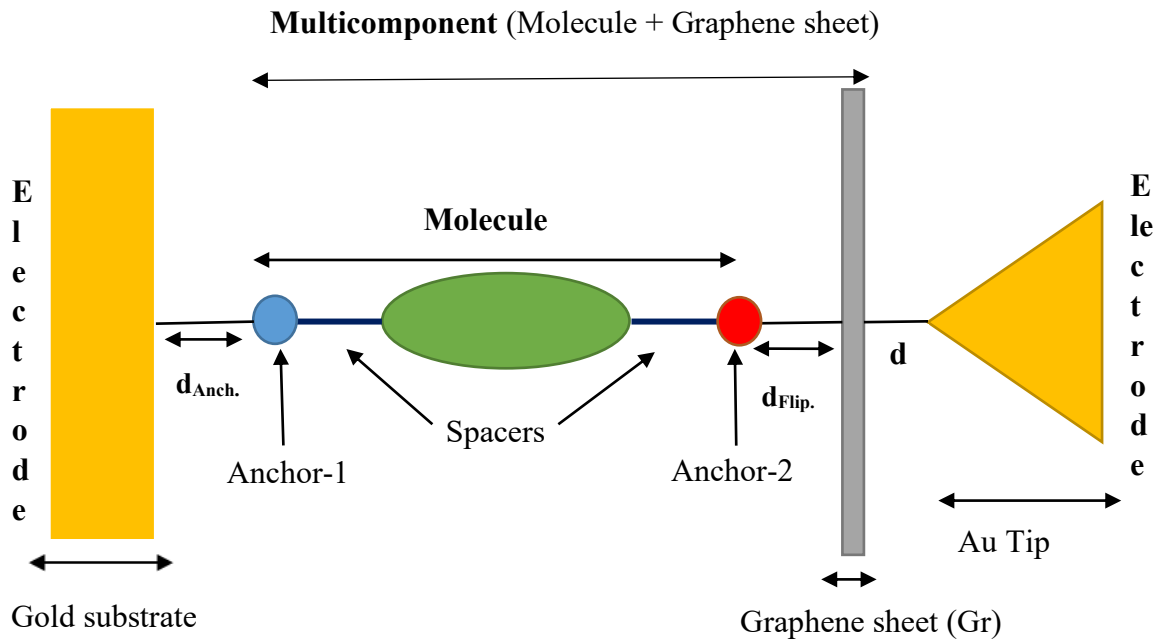

Figure 5.21: Representation of multicomponent junction, highlighting the key components such as anchor groups, spacers, Gr and Au electrodes.

After demonstrating how the flipping feature achieves, I am going to investigate three cases named **Scenario: A**, **Scenario: B** and **Scenario: C**, as follows:

5.9.1 Scenario A:

In this scenario, I choose an asymmetric anthracene-based molecule of two different anchors including alkynyl and Py, then I attach it to a Gr sheet in two separate cases. Case **a**, when the pyridyl anchor binds to the Gr sheet while alkynyl binds to Au at the other end. Case **b**, is the opposite of case **a**, means the alkynyl binds to Gr and Py to Au, as shown in Figure 5.22.

If the two anchors were pyridyl, then one would expect this junction to be a LUMO-dominated, as pyridyl is a typical LUMO-dominated anchor. However, this expectation is still valid for both cases **a** and **b** even though the molecule is an asymmetric, means two different anchors Py- alkynyl, as shown in Figure 5.23.

This is because the Py anchor overcomes alkynyl even though that the binding energy of alkynyl is stronger (see Table 5.1). Furthermore, the case here is more complicated due to the presence of the graphene sheet.

Figure 5.23-c, shows the DFT-predict Fermi energy $E\text{-}E_F^{DFT}=0$ locates at 0.07 eV away from the LUMO resonance, this happens when the pyridyl anchor attaches to Gr sheet. This location (0.07 eV), has been doubly pushed away from the LUMO resonance (0.13 eV), when the anthracene flips. Some studies, [14], show that the alkynyl is a HOMO-dominated anchor, and this explains why the $E\text{-}E_F^{DFT}=0$ doubly downshifted towards the HOMO resonance as shown Figure 5.23-d,

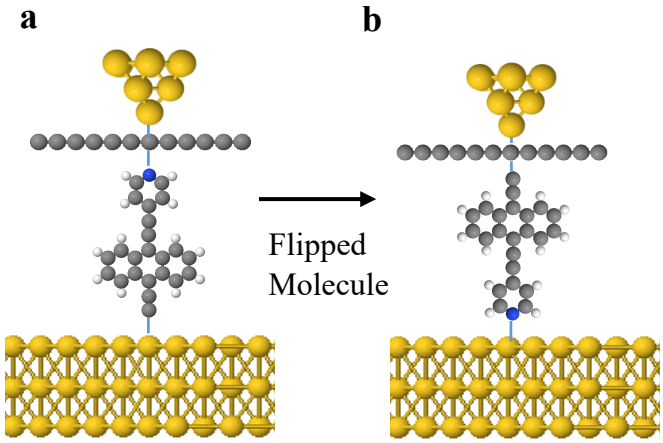

Figure 5.22: Schematic illustration of molecular junctions for **a** and **b. a** and **b** shows how the molecule flips between the Gr sheet and Au. **a** is when Py linked to the Gr and **b** is when alkynyl linked to the Gr.

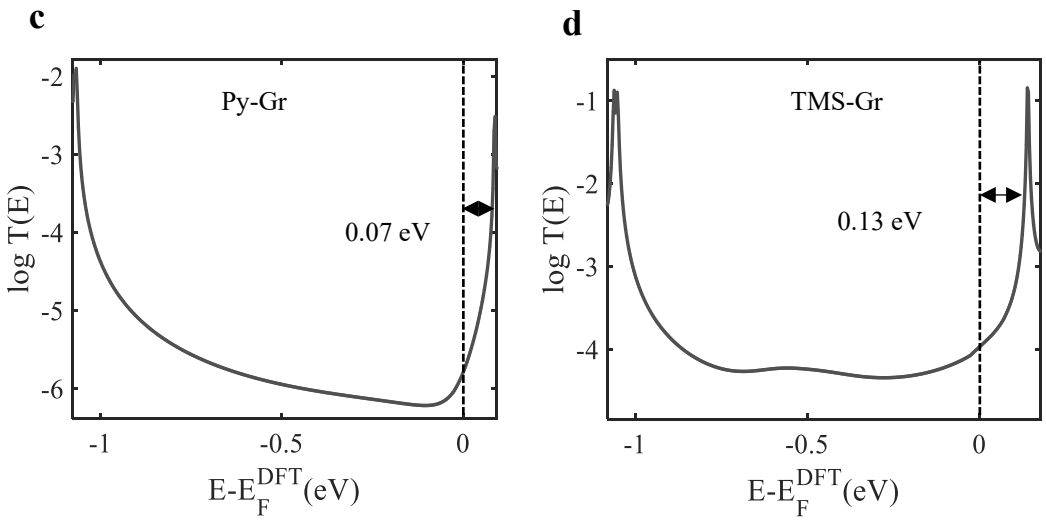

Figure 5.23: Zero bias transmission coefficient *T(E)* against electron energy E. The black curve is the average of the four curves in Figure 5.18. The flipping feature shifts the $E-E_F^{DFT}=0$ from 0.07 to 0.13 eV towards a HOMO resonance (**c** to **d**).

5.9.2 Scenario B:

I consider an asymmetric anthracene of two different anchors including alkynyl and thiol attach to a Gr sheet to form the multicomponent in two cases (**a** and **b**), and place them between Au electrodes, as shown in Figure 5.24-**a** and **-b**.

In this scenario, case **a**, is when the thiol anchor binds to the Gr sheet while alkynyl binds to Au at the other end. Case **b**, is the opposite of case **a**, means the alkynyl binds to G and thiol to Au, as shown in Figure 5.24-**a** and -**b**.

Since, the two anchors are HOMO-dominated, so it is expected to see the DFT-predicted Fermi energy to be biased towards one resonance than the other [14]. However, I would not expect the $E\text{-}E_F^{DFT}=0$, to locate at the same position from that resonance when the molecule flips. This position should be changed due to the fact that the two anchors have different binding energy towards the Gr sheet. In fact, the alkynyl anchor binds 2 times stronger to Gr sheet than that thiol and the separation distance $d_{Flip.}$ is half of the thiol anchor (see Table 5.2).

Figure 5.25-c shows that the $E\text{-}E_F^{DFT}=0$ sits so close to the HOMO resonance with a value of 0.01 eV, while it displaces from the HOMO location by 0.15 eV to the right, as shown in Figure 5.25-d. Thus, even though the both anchors alkynyl and thiol are HOMO-dominated, however they pin the Fermi energy in different locations as the molecule flips [14].

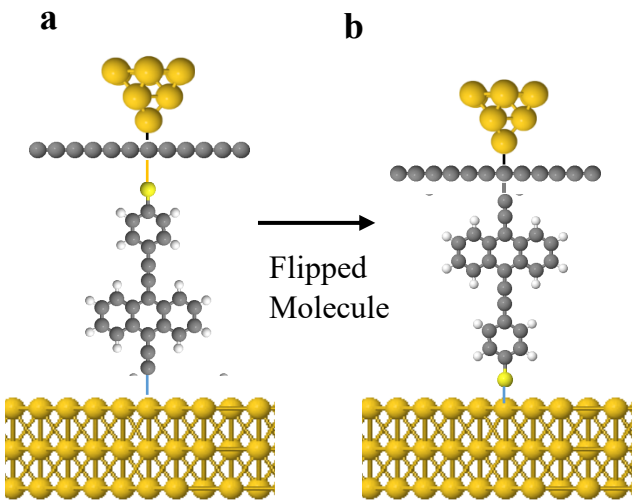

Figure 5.24: Schematic illustration of molecular junctions for **a** and **b. a** and **b** shows how the molecule flips between the Gr sheet and Au. **a** is when thiol linked to the Gr and **b** is when alkynyl linked to the Gr.

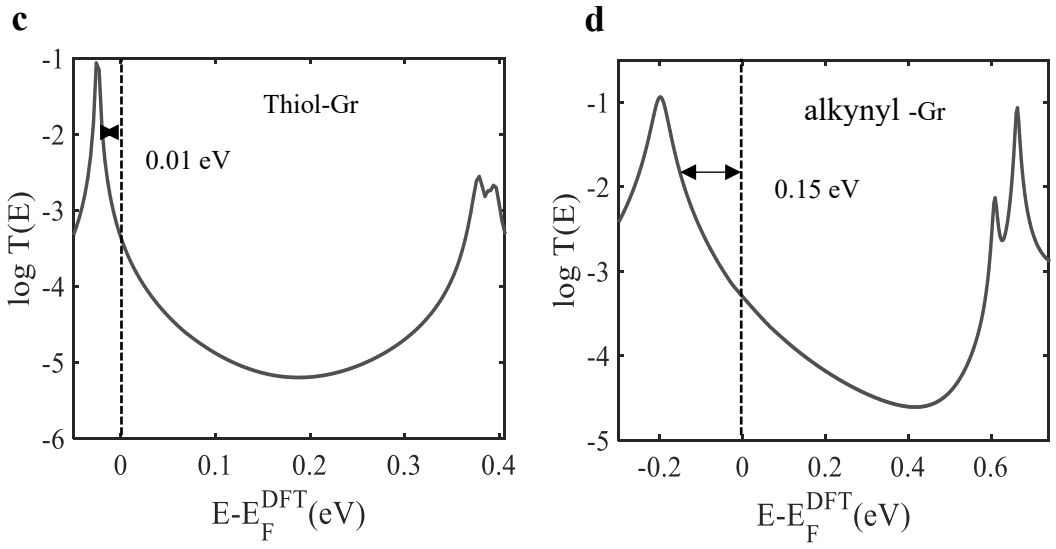

Figure 5.25: Zero bias transmission coefficient *T(E)* against electron energy E. The black curve is the average of the four curves in Fig. 5.19. The flipping feature shifts the $E-E_F^{DFT}=0$ from 0.01 to 0.15 eV towards a LUMO resonance (**c** to **d**).

5.9.3 Scenario C:

Scenario C is an asymmetric anthracene with two different anchors thiol and Py attach to Gr sheet to form a multicomponent in two different cases (**a** and **b**), and place them between Au electrodes, as shown in Figure 5.26-**a** and **-b**.

In this scenario, case **a**, is when the pyridyl anchor binds to the Gr sheet while thiol binds to Au at the other end. Case **b**, is the opposite of case **a**, means the thiol binds to Gr and pyridyl to Au, as shown in Figure 5.26-**a** and **-b**.

As the two anchors are typically known to pin down in an opposite direction. In other words, HOMO- and LUMO-dominated for thiol and Py anchors respectively. Figure 5.27-c, shows a LUMO dominated transmission curve, and this is due to the presence of the pyridyl anchor where the $E\text{-}E_F^{DFT}=0$ sits close to the LUMO resonance with a value of 0.07 eV.

On the other hand, Figure 5.27-d, shows a HOMO dominated transmission curve. This is due to the presence of the thiol anchor where the $E\text{-}E_F^{DFT}=0$ sits close to the HOMO resonance and it displaces by 0.31 eV away from the LUMO resonance. This displacement such an important characteristic because it causes the slope of the transmission curve to change from positive to negative or vice versa. Flipping an asymmetric molecule in a junction is the technique to switch the slope of the transmission function, which is a desirable feature in the thermopower generation as I will discuss later. Table 5.6 summarises the flipping calculations.

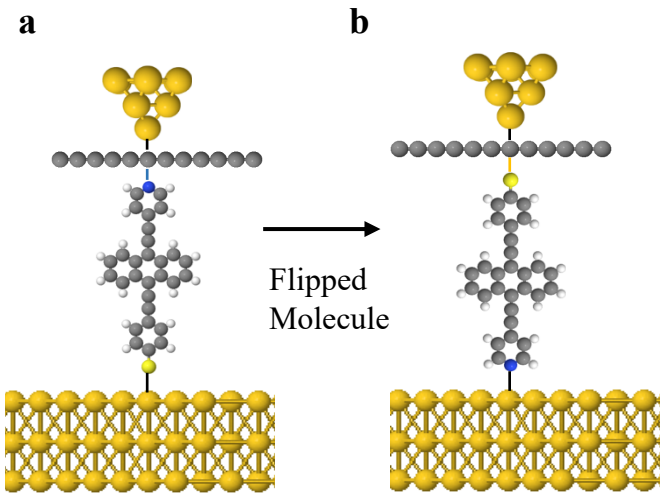

Figure 5.26: Schematic illustration of molecular junctions for **a** and **b. a** and **b** shows how the molecule flips between the Gr sheet and Au. **a** is when Py linked to the Gr and **b** is when thiol linked to the Gr.

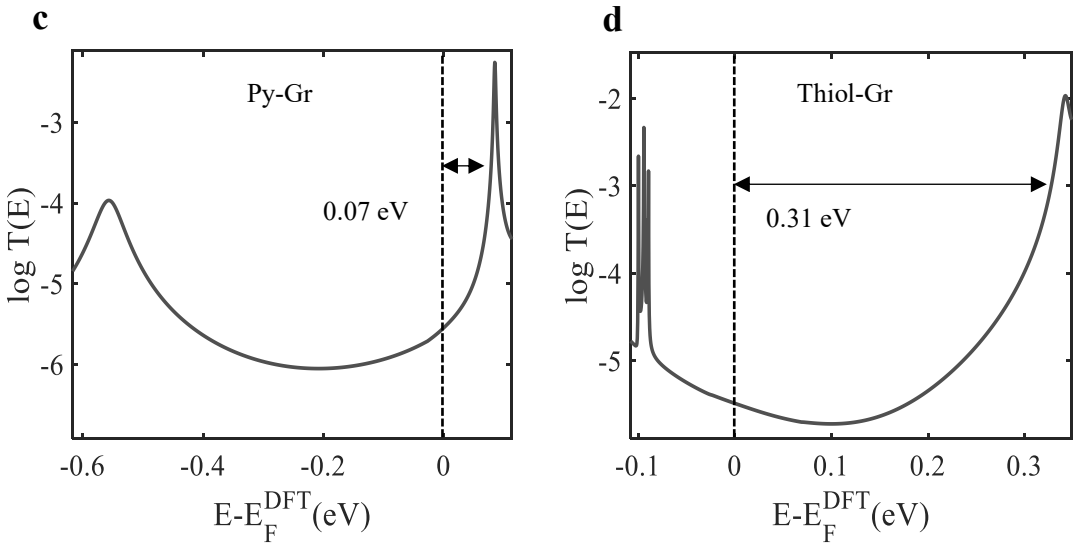

Figure 5.27: Zero bias transmission coefficient *T(E)* against electron energy E. The black curve is the average of the four curves in Fig. 5.20. The flipping feature shifts the $E\text{-}E_F^{DFT}=0$ from 0.07 to 0.31 eV towards a HOMO resonance (**c** to **d**).

Table 5.6: Summarises all the multicomponent calculations including displacement and type domination.

Multicomponent	Displacement (eV)	Type domination
Au-Py-Anthracene- alkynyl ***-Gr***-Au.	0.13	LUMO
Au- alkynyl -Anthracene-***Py-Gr***-Au	0.07	LUMO
Au-Thiol-Anthracene- alkynyl ***-Gr***-Au	0.15	HOMO
Au- alkynyl -Anthracene-***Thiol-Gr***-Au.	0.01	HOMO
Au-Thiol-Anthracene-***Py-Gr***-Au.	0.07	LUMO
Au-Py-Anthracene-***Thiol-Gr***-Au.	0.31	HOMO

5.10 Seebeck coefficient *S* .

In section 5.9, the transmission curve has been calculated at different locations on a Gr sheet then the average is taken as shown in the 3 scenarios (Figures 5.23, 5.25 and 5.27). In this section, the Seebeck coefficient *S* for the same locations calculates and the average is taken for the 3 flipping scenarios.

By using equations (4.2-4.5) mentioned in chapter 4, the *S* calculate for cases labelled **a**, as shown in Figures (5.28, 5.30, 5.32)-a, and cases labelled **b,** as shown in Figures (5.28, 5.30, 5.32)-b.

5.10.1 Scenario A:

The Seebeck coefficient *S* calculate for both cases **a** and **b** of Figure 5.28 below. Panels **c** and **d** of Figure 5.29 both show a negative *S* at the DFT-predicted Fermi energy ($E-E_F^{DFT}=0$ eV), as junctions **a** and **b** possess LUMO dominated transmission curves as shown Figure 5.23-a and -b. Since no switching in the sign of *S* while the molecule is flipped, this suggests that an asymmetric anthracene molecule with Py and alkynyl anchors is not the proper candidate for producing a flipping feature.

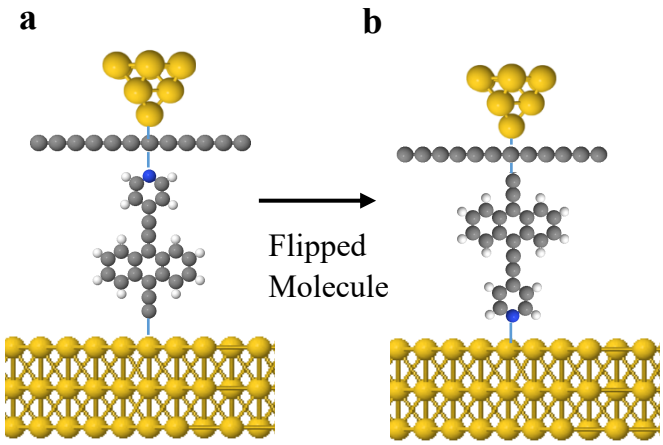

Figure 5.28: Schematic illustration of molecular junctions for **a** and **b. a** and **b** shows how the molecule flips between the Gr sheet and Au. **a** is when Py linked to the Gr and **b** is when alkynyl linked to the Gr.

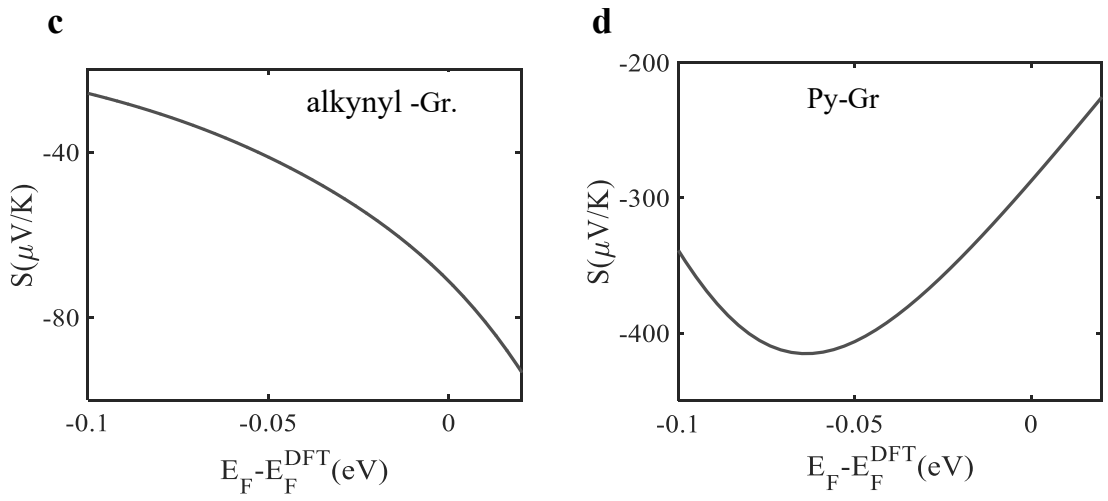

Figure 5.29: Average Seebeck coefficient *S* as a function of the energy for junctions **a** and **b** of Figure 5.28. **c:** Py attaches Gr sheet**. d:** alkynyl attaches to Gr sheet**.** Both junctions show a negative *S*.

5.10.2 Scenario B:

I repeat the same calculations of scenario-A, however, different anchors including alkynyl, and thiol for both cases **a** and **b** of Figure 5.30 below. Panels **c** and **d** of Figure 5.31 both show a positive *S* at the DFT-predicted Fermi energy ($E-E_F^{DFT}=0$ eV), as junctions **a** and **b** possess HOMO dominated transmission curves as shown Figure 5.25-a and -b. Since no switching again in the sign of *S* while the molecule is flipped, this suggests that an asymmetric anthracene molecule with thiol and alkynyl anchors is not the proper candidate for producing a flipping feature.

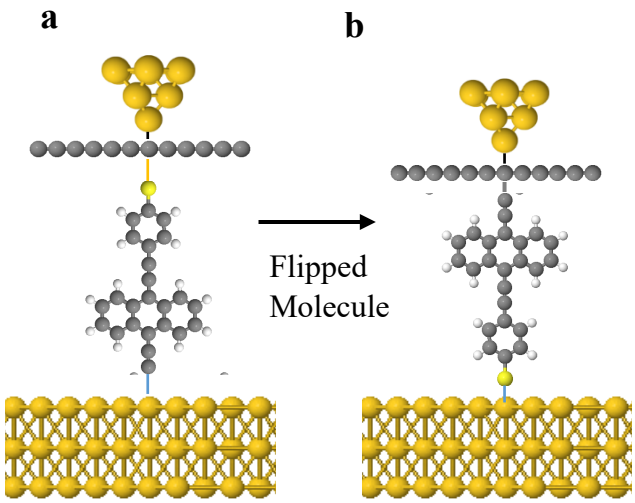

Figure 5.30: Schematic illustration of molecular junctions for **a** and **b. a** and **b** shows how the molecule flips between the Gr sheet and Au. **a** is when thiol linked to the Gr and **b** is when alkynyl linked to the Gr.

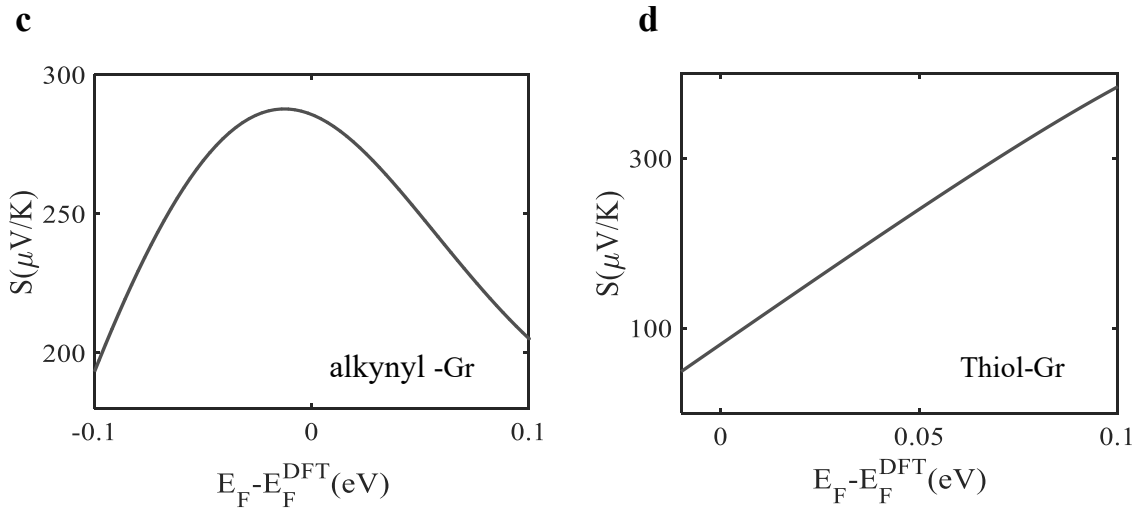

Figure 5.31: Average Seebeck coefficient *S* as a function of the energy for junctions **a** and **b** of Figure 5.30. **c:** alkynyl attaches Gr sheet**. d:** Thiol attaches to Gr sheet**.** Both junctions show a positive *S*.

5.10.3 Scenario C:

The calculations of scenarios-A and -B are repeat, however, different anchors including Py, and thiol for both cases **a** and **b** of Figure 5.32 below. Upper and lower panels (**c** and **d)** of Figure 5.33 demonstrate an opposite sign. Means, a positive and negative *S* at wide range of energy around the DFT-predicted Fermi energy ($E-E_F^{DFT}=0$ eV), as junctions **a** and **b** possess a LUMO and HOMO dominated transmission curves as shown Figure 5.27-a and -b. This scenario illustrates a clear example of switching the sign of *S* while the molecule is flipped. Scenario-C provides a proper candidate for producing a flipping feature through employing an asymmetric anthracene molecule with thiol and pyridyl anchors.

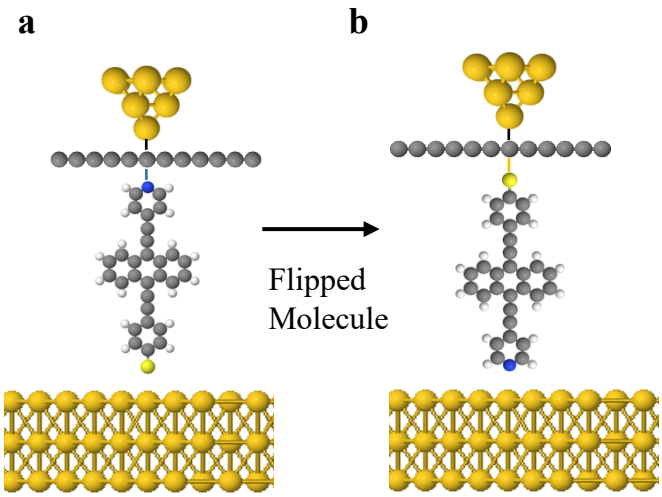

Figure 5.32: Schematic illustration of molecular junctions for **a** and **b. a** and **b** shows how the molecule flips between the Gr sheet and Au. **a** is when Py linked to the G and **b** is when thiol linked to the Gr.

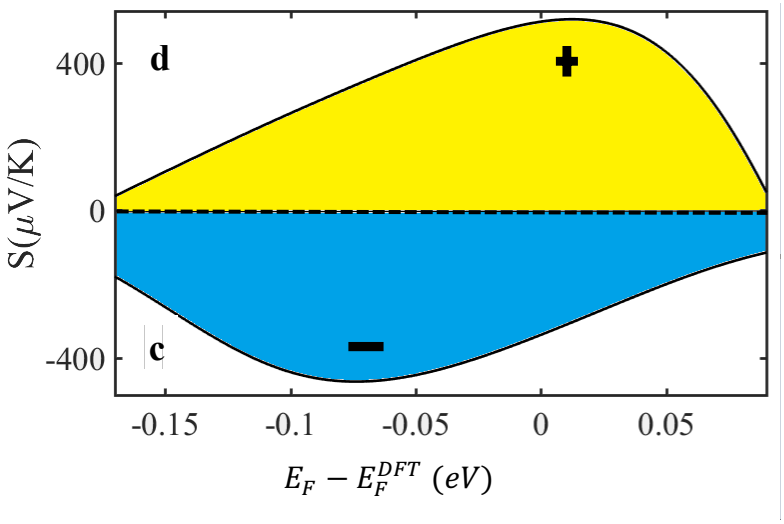

Figure 5.33: Average Seebeck coefficient S as a function of the energy for junctions **a** and **b** of Figure 5.32. **c:** Py attaches G sheet**. d:** Thiol attaches to Gr sheet**.** Junction **a** shows a negative S while **b** shows positive S.

5.11 Conclusion

Overall, I have investigated novel theoretical results by studying asymmetric anthracene of different anchor groups including alkynyl, thiol and Py. Firstly, I studied three asymmetric anthracene without graphene sheet, meaning that I connect them to the Au electrodes. I have demonstrated that the $T(E)$ and the S for these asymmetric anthracene molecules at the DFT-predicted Fermi energy ($E\text{-}E_F^{DFT}=0$ eV), have interested features including oscillation and flipping. I found that the anthracene of alkynyl -Py anchors is a HOMO-dominated with

negative *S*; while the anthracene of alkynyl -thiol is a LUMO-dominated with positive *S*. While An anthracene of Py-thiol anchors is more mid-gap than a HOMO- or LUMO-dominated.

By adding a graphene sheet Gr to these asymmetric anthracenes, I was able to investigate the oscillation by pulling the Gr sheet on the molecule in four different locations. I employ for this purpose three asymmetric molecules containing different anchor group including alkynyl, thiol and Py. I have calculated the transmission coefficient curves (black, green, red and blue curves) for four the positions **1, 2, 3** and **4**, respectively. I also found that the oscillation for the first case (alkynyl -G) is uniform while it is less uniform for the last two cases (thiol-Gr) and (Py-Gr), respectively. The oscillation ratio is found to be 0.4, 0.34 and 0.6 for the three cases respectively.

Finally, I consider the flipping technique for an asymmetric molecule; where I first linked anchor-1 to a Gr sheet form multicomponent and then placed it between two Au electrodes. Secondly, I flipped the asymmetric molecule where the anchor-2 is now linked to the Gr sheet to form multicomponent, then placed it between two Au electrodes. For this purpose, three asymmetric anthracene molecules including (alkynyl -Py) anchor group, (alkynyl -Thiol) anchor group, and (Py-Thiol) anchor group were employed. Thus, I found that by flipping a proper asymmetric anthracene molecule to the graphene sheet, I can control the sign of the Seebeck coefficient *S*.

5.12 Bibliography

1. Rincón-García, L., Ismael, A. K., Evangeli, C., Grace, I., Rubio-Bollinger, G., Porfyrakis, K., and Lambert, C. J. (2016). Molecular design and control of fullerene-based bi-thermoelectric materials. *Nature materials*, *15*(3), 289-293.
2. Ferrer, J., Lambert, C. J., García-Suárez, V. M., Manrique, D. Z., Visontai, D., Oroszlany, L., and Algharagholy, L. A. (2014). GOLLUM: a next-generation simulation tool for electron, thermal and spin transport. *New Journal of Physics*, *16*(9), 093029.
3. Ismael, Ali K., Iain Grace, and Colin J. Lambert. "Increasing the thermopower of crown-ether-bridged anthraquinones." *Nanoscale* 7.41 (2015): 17338-17342.
4. Ismael, A. K., and Lambert, C. J. (2020). Molecular-scale thermoelectricity: a worst-case scenario. *Nanoscale Horizons*, *5*(7), 1073-1080.
5. Cui, L., Miao, R., Jiang, C., Meyhofer, E., and Reddy, P. (2017). Perspective: Thermal and thermoelectric transport in molecular junctions. *The Journal of Chemical Physics*, *146*(9), 092201.
6. Yzambart, G., Rincón-García, L., Al-Jobory, A. A., Ismael, A. K., Rubio-Bollinger, G., Lambert, C. J., and Bryce, M. R. (2018). Thermoelectric Properties of 2, 7-Dipyridylfluorene Derivatives in Single-Molecule Junctions. *The Journal of Physical Chemistry C*, *122*(48), 27198-27204.
7. Al-Galiby, Q. H., Sadeghi, H., Algharagholy, L. A., Grace, I., and Lambert, C. (2016). Tuning the thermoelectric properties of metallo-porphyrins. *Nanoscale*, *8*(4), 2428-2433.

8. Wang, X., Bennett, T. L., Ismael, A., Wilkinson, L. A., Hamill, J., White, A. J., and Lambert, C. J. (2020). Scale-up of room-temperature constructive quantum interference from single molecules to self-assembled molecular-electronic films. *Journal of the American Chemical Society*, *142*(19), 8555-8560.
9. Ismael, A., Al-Jobory, A., Wang, X., Alshehab, A., Almutlg, A., Alshammari, M., and Lambert, C. (2020). Molecular-scale thermoelectricity: as simple as 'ABC'. *Nanoscale Advances*, *2*(11), 5329-5334.
10. Wang, X., Ismael, A., Almutlg, A., Alshammari, M., Al-Jobory, A., Alshehab, A., and Lambert, C. (2021). Optimised power harvesting by controlling the pressure applied to molecular junctions. *Chemical Science*.
11. Lambert, C.J. and Liu, S.X., 2018. A magic ratio rule for beginners: a chemist's guide to quantum interference in molecules. *Chemistry–A European Journal*, 24(17), pp.4193-4201.
12. Reddy, P., Jang, S. Y., Segalman, R. A., and Majumdar, A. (2007). Thermoelectricity in molecular junctions. *Science*, *315*(5818), 1568-1571.
13. Bergfield, J. P., & Stafford, C. A. (2009). Thermoelectric signatures of coherent transport in single-molecule heterojunctions. *Nano letters*, *9*(8), 3072-3076.
14. Ismael, A. K., & Lambert, C. J. (2019). Single-molecule conductance oscillations in alkane rings. *Journal of Materials Chemistry C*, *7*(22), 6578-6581.

Chapter 6

Conclusion and Future Work

6.1 Conclusion

This thesis has focused on the following chapters:

Chapter 1 represents a general picture of molecular electronics, thermoelectricity, and the thesis outline.

Chapter 2 introduces general concepts of DFT code SIESTA, which is applied to all studied electronic structure calculations in this thesis. In the stimulation work, I extracted the Hamiltonian of an isolated molecule and relaxing it, and then connecting this isolated molecule to metallic electrodes to calculate the transport properties.

Chapter 3 is the single-particle transport theory, including the landau formula, thermoelectric coefficients, and scattering theory.

Chapter 4 is the DFT calculations compared with the experimental measurements, where I focus intensely on the electronic properties of anthracene molecules having two pyridyl anchor groups. I studied this molecule, called Di (4-(ethynyl) phenylthioacetate), with different connectivities including (**9, 10**) and (**1, 5**). I have demonstrated the wave function plots of both connectivities to predict whether they possess a constructive or destructive QI, the binding energy to find the optimum separation distance between the molecule and the metallic electrodes, the transmission coefficient $T(E)$, and the Seebeck coefficient S. Through a theoretical model, I found that the tilt angle θ plays a role as a pivotal parameter in increasing the conductance G and decreasing the thermopower S as well. My theoretical simulations have

been checked against experimental measurements via several parameters and as follows: anthracene molecule with thioether liker group does not bind to a porphyrin molecule while the same molecule with pyridyl linker does bind. Both connectivities (**9, 10**) and (**1, 5**) have a CQI and the ratio between them about 16 for the bare molecules. This ratio decreases (less than 16) when they molecule combine with either graphene sheet or porphyrin or both of them. This combination decreases the conductance G, however, it boosts the Seebeck coefficient S. Finally, an excellent agreement is found between my simulations and the measurements.

Chapter 5 is based on the same core molecules that have been studied in chapter 4, however in different directions. This chapter presents novel theoretical results of asymmetric anthracene molecules linked to the graphene sheet to form multicomponent. I investigate asymmetric anthracene molecules with different anchor groups, such as alkynyl, thiol, and pyridyl. Firstly, I have studied the oscillation behaviour of the multicomponent in four different positions **1, 2, 3** and **4** while pulling a graphene sheet in the junction in a way that the Au tip and the anchor are aligned and passes through a C atom in the Gr sheet., Secondly, I proposed the flipping technique when an asymmetric molecule is attached to a Gr sheet via anchor-1 to form multicomponent-1, and then the same molecule again attaches to the same sheet, however this time via anchor-2 (anchor-1 and anchor-2 are different), to form multicomponent-2. Both multicomponent placed between Au electrodes to calculate $T(E)$, and eventually S. The two different multicomponent show positive and negative signs of S which is of interest to have bi-thermal material just by flipping the same molecule.

6.2 Future work

In this thesis I have concentrated on the Seebeck coefficient and the electrical conductance of the self-assemble monolayer (SAMs) for the anthracene molecule. I studied symmetric molecule, chapter4, the following: the anthracene-based molecule, anthracene +Gr, anthracene+Zn-TTP and anthracene+Zn-TTP + Gr. In chapter 5, I have studied asymmetric molecule for three different anchor group Alkynyl, Py and thiol linked to Gr sheet. For the future work, one can envisage extending these in a number of directions. First it is interesting to investigate how the calculations change when the gold leads are replaced by alternative metals such as platinum, palladium and iron. Secondly, it would be interesting to examine the electronic properties of different molecules such as OPE3 linked to a Porphyrin or graphene sheet (multicomponent molecules attached to gold electrodes). Also, these multicomponent molecules can be studied with alternative metals such as platinum. Then, it would be motivated to examine the flipping feature of other asymmetric molecules such as anthracene others with the different type of porphyrin including Co, F and Zn. Similarly, employing other anchor groups for example, amine (NH2), BDT and CN. Studying the flipping feature at different alignment sites including hollow, on-top and bridge. Finally, Studying the flipping (molecule attached to Gr sheet) can be studied at different alignment sites including hollow, on-top and bride. These can be summarized as the following: (a)aligned though hexagon, (b)aligned on carbon atom (on top), (c) nun-aligned on through hexagon ring and (d) non-aligned on the top of carbon atom.